ANALYSIS OF THE ELASTICA WITH APPLICATIONS TO VIBRATION ISOLATION

by

Sophia Teresa Santillan

Department of Mechanical Engineering and Materials Science
Duke University

Date: _____

Approved:

_____
Dr. Lawrence Virgin, Supervisor

_____
Dr. John Dolbow

_____
Dr. Linda Franzoni

_____
Dr. Josiah Knight

_____
Dr. Thomas Witelski

Dissertation submitted in partial fulfillment of the
requirements for the degree of Doctor of Philosophy
in the Department of Mechanical Engineering and Materials Science
in the Graduate School of
Duke University

2007

ABSTRACT

ANALYSIS OF THE ELASTICA WITH APPLICATIONS TO VIBRATION ISOLATION

by

Sophia Teresa Santillan

Department of Mechanical Engineering and Materials Science
Duke University

Date: _____

Approved:

_____
Dr. Lawrence Virgin, Supervisor

_____
Dr. John Dolbow

_____
Dr. Linda Franzoni

_____
Dr. Josiah Knight

_____
Dr. Thomas Witelski

An abstract of a dissertation submitted in partial fulfillment of the
requirements for the degree of Doctor of Philosophy
in the Department of Mechanical Engineering and Materials Science
in the Graduate School of
Duke University

2007

Abstract

Linear theory is useful in determining small static and dynamic deflections. However, to characterize large static and dynamic deflections, it is no longer useful or accurate, and more sophisticated analysis methods are necessary. In the case of beam deflections, linear beam theory makes use of an approximate curvature expression. Here, the exact curvature expression is used to derive the governing partial differential equations that describe the in-plane equilibrium and dynamics of a long, thin, inextensible beam, where the self-weight of the beam is included in the analysis. These beam equations are expressed in terms of arclength, and the resulting equilibrium shape is called the elastica. The analysis gives solutions that are accurate for any deflection size, and the method can be used to characterize the behavior of many structural systems. Numerical and analytical methods are used to solve or to approximate solutions to the governing equations. Both a shooting method and a finite difference, time-stepping algorithm are developed and implemented to find numerical solutions and these solutions are compared with some analytical approximation method results. The elastica equations are first used to determine both linear and nonlinear equilibrium configurations for a number of boundary conditions and loading types. In the case of a beam with a significant self-weight, the system can exhibit nonlinear static behavior even in the absence of external loading, and the elastica equations are used to determine the weight corresponding to the onset of instability (or self-weight buckling). The equations are also used to characterize linear and nonlinear vibrations of some structural systems, and experimental tests are conducted to verify the numerical results. The linear vibration analysis is applied to a vibration isolator system, where a postbuckled clamped-clamped beam or otherwise highly-deformed structure is used (in place of a conventional spring) to reduce system motion. The method is also used to characterize nonlinear dynamic behavior, and the resulting frequency-response curves are compared with those in the literature. Finally, the method is used to investigate the dynamics of subsea risers, where the effects of gravity, buoyancy, and the current velocity are considered.

Contents

List of Tables

List of Figures

Acknowledgements

I'm very thankful to have been given the opportunity to pursue my degrees at Duke University. I'd first like to thank my PhD committee members: Dr. John Dolbow, Dr. Linda Franzoni, Dr. Josiah Knight, Dr. Thomas Witelski, and especially my advisor, Dr. Lawrie Virgin. Dr. Virgin has been a consistent source of guidance and encouragement. I came back to Duke to work with him, and he's been a wonderful mentor and teacher. Dr. Witelski has also, with great patience and care, answered my many research questions, and Dr. Franzoni has been a great friend and teacher to me ever since I first came to Duke. Thanks, also, to Dr. Ray Plaut for always giving quick and thorough answers, suggestions, and advice in response to my many questions and concerns. I'd also like to thank Deirdre McShane and Ben Davis. Deirdre helped with a few preliminary isolator models and became a great friend in the process, and Ben has been a great labmate, hallmate and listener during my last two years at Duke. Finally, I'd like to thank my parents, for their constant support, and Toby, for his friendship and companionship.

This research was supported by the U.S. National Science Foundation under Grant No. CMS-0301084 and by the NASA Graduate Student Researchers Program under Grant No. NGT-1-03016.

Chapter 1

Introduction

Linear theory is useful in determining small static and dynamic deflections. Here the assumptions made in linear theory are shown and an example is given of systems where the theory is accurate. However, to characterize large static and dynamic deflections, linear theory is no longer useful or accurate, and more exact analysis methods are necessary. In the case of beam deflections, linear beam theory makes use of an approximate curvature expression. Here, the limitations of modeling using an Euler-Bernoulli (or linear) beam model are introduced, and in contrast, the exact curvature expression is used to derive and solve the governing partial differential equations that describe the equilibrium and dynamics of a long, thin, inextensible beam. The assumption of no shear deformation is still made, as the beam is slender. The self-weight of the beam is included in the analysis, permitting a study of its effects on the beam response. These beam equations are expressed in terms of arclength, and the resulting equilibrium shape is called the elastica. The analysis gives solutions that are accurate for any deflection size, and the method can be used to characterize the behavior of many structural systems.

Next, the linear dynamics equations are presented and used to confirm familiar beam bending vibration frequencies and mode shapes for a cantilever beam (where the self-weight is neglected).

Experiments are designed and conducted to verify static and dynamic results, using polycarbonate strips. The linear vibration frequencies are found, along with corresponding mode shapes.

Numerical and analytical methods are used to solve or to approximate solutions to the governing equations. Both a shooting method and a finite difference, time-stepping algorithm are introduced and used to find numerical solutions, and some analytical solution methods are compared with these results.

Finally some previous work is presented. Numerical results are found for three systems (including nonlinear static and linear dynamic results), and experiments are conducted to verify these results.

1.1 Structural Behavior Analysis

The analysis of structural behavior (whether for static or dynamic response) can be categorized in terms of linearity.

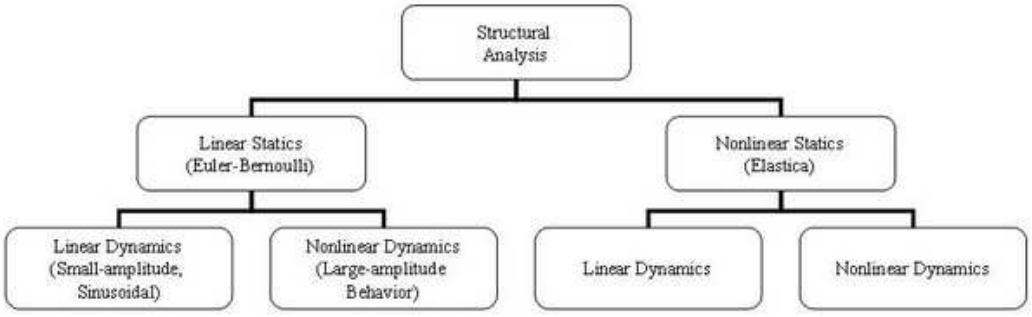

Figure 1.1: Structural Analysis in terms of linearity.

1.1.1 Statics

First, as illustrated in Figure 1.1, the linearity of the static problem is determined. In general, the assumption of linearity is sufficient (in terms of accuracy) for the case of small static deflections, and this assumption significantly simplifies the governing equations and solution process. In the case of beam analysis, for example, Euler-Bernoulli beam theory assumes linearity and so is appropriate for use in determining the static (or equilibrium) behavior of beams undergoing small deflections. In this case, for a specific loading type, the weight of the beam itself is neglected, and the deflection of the beam along its length can easily be found analytically by direct integration.

Of course for the case of large static deflections, the assumption of linearity is no longer valid. The loaded beam, for example, behaves nonlinearly if the loading causes a lateral deflection with a magnitude beyond some percentage of the beam length. In the case of a beam with a significant self-weight, the system can exhibit nonlinear static behavior even in the absence of external loading. Because linear beam theory results from an approximation of beam curvature, the exact equation for curvature must be used for large deflections. Depending on the deflection size to be modeled, this expression may be approximated by a truncated series (where use of the first term only is equivalent to linear beam theory). The beam equations can be expressed in terms of arclength, and the resulting equilibrium shape is called the elastica.

The exact expression for the curvature of a long, thin, inextensible beam is given by [1]

$$\frac{1}{\rho} = \frac{d\theta}{dS} \tag{1.1}$$

where S and θ are the arclength of the beam and the angle formed by the beam with the X-axis, respectively, as pictured for the case of the upright cantilever beam in Figure 1.2.

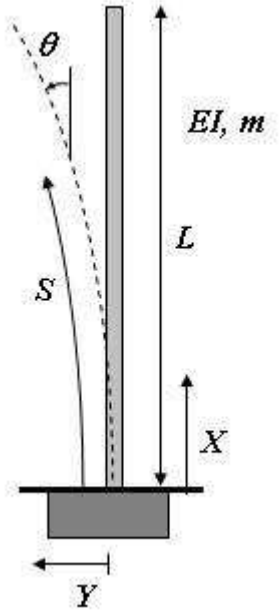

Figure 1.2: Upright vertical cantilever beam.

In Cartesian coordinates, the curvature is given by

$$\frac{1}{\rho} = \frac{d\theta}{dS} = \frac{d\theta}{dX}\frac{dX}{dS} = \frac{\frac{d^2Y}{dX^2}}{[1+(\frac{dY}{dX})^2]^{3/2}} = \frac{\frac{d^2Y}{dX^2}}{1+\frac{3}{2}(\frac{dY}{dX})^2+\frac{3}{8}(\frac{dY}{dX})^4+\ldots}, \tag{1.2}$$

where the denominator is expanded as a Taylor Series. If the slope of the beam, dY/dX, is small along its entire length (as for linear beam theory), then its square and higher powers are negligible and the curvature can be approximated using only the first series term, giving

$$\frac{d^2Y}{dX^2} \approx \frac{1}{\rho}. \tag{1.3}$$

Using the elastic flexure formula [2], the curvature can be expressed by

$$\frac{1}{\rho} = \frac{M}{EI}, \tag{1.4}$$

where M is the bending moment, and EI is the flexural rigidity (or bending stiffness). The exact equation 1.1 is then written

$$\frac{d\theta}{dS} = \frac{M}{EI}. \tag{1.5}$$

and the corresponding linear approximation for the curvature (equation 1.3) becomes

$$\frac{d^2Y}{dX^2} \approx \frac{M}{EI}. \tag{1.6}$$

If the moment, M, can be expressed as an integrable function of the coordinate X, then the linear approximation given by equation 1.6 can be used and integrated twice, using specified boundary conditions. For the case of a cantilever, these conditions are

$$Y(0) = Y'(0) = 0, \quad Y''(L) = Y'''(L) = 0, \tag{1.7}$$

where a prime denotes differentiation with respect to X. The resulting analytical displacement function, $Y(X)$, gives the linear approximation for beam deflection under the given loading conditions.

If the self-weight of the cantilever is included in the analysis, however, the bending moment is in the form of an integral, and so the linear equation 1.6 cannot be easily integrated to determine even small-deflection behavior. Although the solution cannot be found analytically, some approximations can be made from the assumption of small deflections, thereby simplifying the problem.

The term "heavy" is used to indicate that self-weight is included in the analysis, and the upright heavy cantilever is shown in Figure 1.2. The beam has length L and weight per unit length $W \equiv mg$, where m is the mass per unit length. The lateral deflection is given by Y. For a range of small self-weight values, the beam remains in a straight, vertical configuration. But as the weight is increased, the beam may undergo self-weight buckling (the trivial solution is still an equilibrium state, but becomes unstable) [3]. The nonlinear governing equation for this case using the exact equation 1.5 is [4]

$$\frac{d^2\theta}{dS^2} = \frac{-W(L-S)\sin\theta}{EI}, \tag{1.8}$$

and the corresponding Cartesian-coordinate equation (using equation 1.6) is given by [1]

$$\frac{d^3Y}{dX^3} = \frac{-W(L-X)}{EI}\frac{dY}{dX}. \tag{1.9}$$

Equation 1.8 was first solved by Greenhill [3] using a Bessel function, and was used to determine the critical buckling load (or self-weight) [1],

$$W_c \approx 7.837EI/L^3. \tag{1.10}$$

Alternatively, an energy method may be used to determine the critical buckling load, where the postbuckled beam deflection is assumed [1, 5].

The resulting non-trivial equilibrium configuration can be approximated with a number of methods. For postbuckled results near buckling (such that lateral beam deflections are small), a deflected shape may be assumed and an energy method used to determine the weight-deflection relationship. Virgin [5] used this method, where the deflected shape was assumed such that

$$Y(X) = Q\left[1 - \cos\left(\pi X/2L\right)\right], \tag{1.11}$$

and the resulting load-deflection relationship was given by

$$W/W_c = 1 + 0.5186(Q/L)^2. \tag{1.12}$$

This expression is equivalent to

$$\tan\theta_L = (\pi/2)\sqrt{\left(W/W_c - 1\right)/0.5186}, \tag{1.13}$$

where $\theta_L = \theta(L)$ is the angle made by the tangent to the beam with the vertical at the free end. Another method used in the literature is to make use of the exact curvature. Frisch-Fay [4] approximated the solution using a Taylor Series, giving

$$\theta_L - w\sin\theta_L/6 + w^2\sin(2\theta_L)/360 + w^3\sin^3\theta_L/5184 - w^3\cos\theta_L\sin 2\theta_L/25920 = 0, \tag{1.14}$$

where $w = WL^3/EI$, and a small-angle approximation was used to determine initial postbuckling behavior, giving

$$\theta_L = 2.1\sqrt{W/W_c - 1}. \tag{1.15}$$

Timoshenko and Gere [1] found the exact solution to equation 1.8 using elliptic integrals, which were also used by Sinclair [6], where shear and longitudinal deformations are also considered. The three results given by equations 1.13-1.15 are plotted in Figure 1.3, along with the exact solution. Each of the methods gives an underestimate of beam deflection for a given self-weight and is accurate only for a very small range of postcritical weight values. The most accurate approximation is given by equation 1.14, but varies significantly from the exact solution even when the self-weight is only 10 percent above critical.

Even for a nonlinear governing beam-deflection equation, a linear approximation may be used to generate deflection results that are accurate for a range of small deflections. Certainly the use of the exact equation for curvature is necessary to accurately determine the behavior of highly-deflected

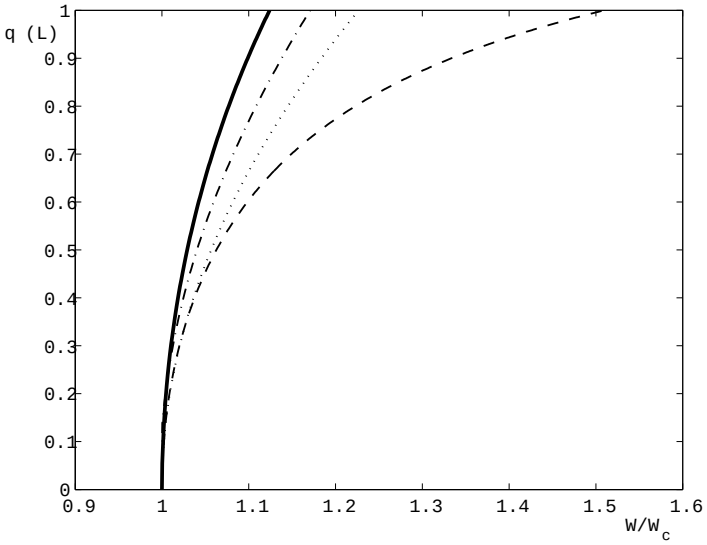

Figure 1.3: Tip angle versus self-weight approximations for the postbuckled upright heavy cantilever. Solid curve: exact solution; dot-dashed curve: equation 1.14 [4]; dotted curve: equation 1.15 [4]; dashed curve: equation 1.13 [5].

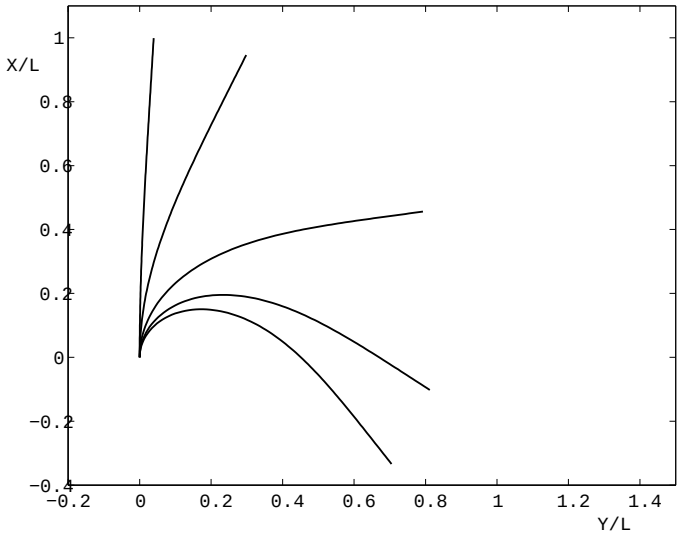

Figure 1.4: Equilibrium configurations of an upright heavy cantilever with nondimensional weight, $w = WL^3/EI = 7.84, 8, 10, 15, 20$, or normalized weights, $W/W_c = 1.0004, 1.02, 1.28, 1.91, 2.55$.

beams. In addition, while they greatly simplify the analysis, no assumptions may be made in the large-deflection case that limit the deflection size.

Figure 1.4 depicts the equilibrium configuration for the heavy, upright, postbuckled cantilever for varying nondimensional self-weight values (where, as before, $w = WL^3/EI$). These results were found numerically (with the shooting method, shown in Section 1.3), using the exact curvature equation 1.8, with no small-deflection assumptions.

The inclusion of self-weight in the analysis clearly makes a significant difference in the equilibrium shape, and can also lead to qualitative changes in the system dynamics.

1.1.2 Dynamics

Once the appropriateness of static linearity of the system is determined, a dynamic analysis can be conducted, and this study can also be categorized in terms of linearity (Figure 1.1). So far, it has been shown that the exact governing equations for the equilibrium configuration of a beam with specific boundary conditions can be obtained. In addition, the exact curvature equation can be used to determine highly-deflected static configurations. The dynamic behavior of the system can also reveal significant information concerning stability, and so it is worth investigating as part of a thorough system analysis. In cases where the buckling and vibration mode shapes of a beam are identical, the relationship between the axial load and the square of the lowest natural frequency is linear. Even in the cases where buckling and vibration mode shapes are not the same, the deviation from linearity is often very small, and this property has been exploited for non-destructive testing purposes [7, 8].

D'Alembert's principle states that [9]

> the virtual work performed by the effective forces through infinitesimal virtual displacements compatible with the system constraints is zero, i.e.

$$\sum_{k=1}^{N} \left(\vec{F_k} - m_k \ddot{\vec{r_k}} \right) \cdot \delta \vec{r_k} = 0 \tag{1.16}$$

where F_k is the applied force, and $m_k \ddot{\vec{r_k}}$ is the inertial force of the mass particle, m_k.

Returning to the cantilever and neglecting self-weight, the principle can be used to derive the governing partial differential equation for small-amplitude free beam bending vibration [9]

$$m\ddot{Y} + EIY'''' = 0, \quad 0 \leq X \leq L, \tag{1.17}$$

where T is dimensional time, X is the longitudinal coordinate, m is the mass per unit length, $\dot{Y} \equiv \partial Y/\partial T$ and $Y' \equiv \partial Y/\partial X$, and damping is neglected. Note that the corresponding equations for the static configuration, combined with the appropriate boundary conditions (equation 1.7), give the trivial solution $Y(X) = 0$, as expected.

One solution method is known as the separation of variables, where it is assumed that $Y(X,T)$ is the product of two functions, one spatial and one temporal, such that [10]

$$Y(X,T) = B(X)R(T). \tag{1.18}$$

The spatial function, $B(X)$, then corresponds to the mode shape for a particular frequency [10]. This relationship and equation 1.17 lead to two ordinary differential equations from

$$-\frac{EIB''''}{mB} = \frac{\ddot{R}}{R} = C \tag{1.19}$$

where C is a constant. Focusing only on the temporal function, it can be seen that $R(T)$ can be written in the form

$$R(T) = Ae^{i\omega T}, \tag{1.20}$$

where $C = -\omega^2$. The qualitative dynamic behavior is then dependent on ω, which itself is dependent on the spatial function and boundary conditions from

$$EIB'''' = \omega^2 mB. \tag{1.21}$$

Solutions take the form

$$B(X) = a_1 \sin bX + a_2 \cos bX + a_3 \sinh bX + a_4 \cosh bX, \tag{1.22}$$

where $b^4 = m\omega^2/EI$, and four of the five constants, a_k and b, are determined using the boundary conditions (equation 1.7). The remaining constant is arbitrary; it determines the magnitude of vibration (and so must be small).

There are infinitely many values for ω_j^2, corresponding to the natural frequencies (and modes) of the system. The first natural frequency for the cantilever is given by $\omega_1 \approx 3.516\sqrt{EI/mL^4}$ and the corresponding mode shape is described by

$$B(X) = \cosh bX - \cos bX - \sigma(\sin bX - \sinh bX), \tag{1.23}$$

where $\sigma \approx 0.7341$ [11].

In general, if $\omega_j^2 > 0$, the response, $R_j(T)$ is purely harmonic and can be expressed as a linear combination of $\sin\omega_j T$ and $\cos\omega_j T$, and the system is stable. If the smallest frequency squared, ω_1^2, becomes negative, then the temporal solution, $R_1(T)$ is expressed as a linear combination of hyperbolic functions, $\sinh\omega_1 T$ and $\cosh\omega_1 T$ that grow with time (i.e. the system is unstable). So the conditions that yield $\omega_1 = 0$ correspond to the onset of instability.

Linear vibration frequencies and mode shapes can be found for the upright heavy prebuckled cantilever, and this relationship between the first natural frequency and instability (or, in this case, self-weight buckling) can be seen.

The governing equation for beam bending vibration of the heavy beam is given by

$$m\ddot{Y} + EIY^{''''} + W[(L-X)Y']' = 0. \tag{1.24}$$

Note that, as before, it can be shown that the equilibrium solution (in the case of the heavy pre-buckled cantilever) is $Y(X) = 0$. Because the equilibrium configuration is not one that is highly-deflected and only small-amplitude (or linear) vibrations are of interest, accurate results can be found using this Cartesian-coordinate equation.

Introducing the nondimensional quantities

$$w = WL^3/EI, \quad x = X/L, \quad y = Y/L, \quad t = (T/L^2)\sqrt{EIg/W}, \tag{1.25}$$

equation 1.24 can be rewritten

$$\ddot{y} + y^{''''} + w[(1-x)y']' = 0, \tag{1.26}$$

where $\dot{y} \equiv \partial y/\partial t$ and $y' \equiv \partial y/\partial x$. Assuming harmonic motion and using $\Omega = \omega L^2\sqrt{W/EIg}$ (where ω is a dimensional vibration frequency), or that the lateral motion is of the form

$$y(x,t) = \bar{y}(x)\sin\Omega t \tag{1.27}$$

gives

$$\bar{y}^{''''} + w[(1-x)\bar{y}']' - \Omega^2\bar{y} = 0, \tag{1.28}$$

The nondimensional boundary conditions are

$$\bar{y}(0) = \bar{y}'(0) = 0, \quad \bar{y}''(1) = \bar{y}'''(1) = 0, \tag{1.29}$$

and the equation may be solved numerically (as shown in Section 1.3) to determine the natural frequencies and mode shapes of the system.

For a self-weight value $w = 0$, the analysis gives

$$\omega_j = \Omega_j \sqrt{\frac{EIg}{WL^4}}, \quad \Omega_j = 3.516(j=1), 22.034(j=2), 61.697(j=3)...., \tag{1.30}$$

consistent with those known for the free vibration of a cantilever where weight is neglected (and for the weightless example above) [9].

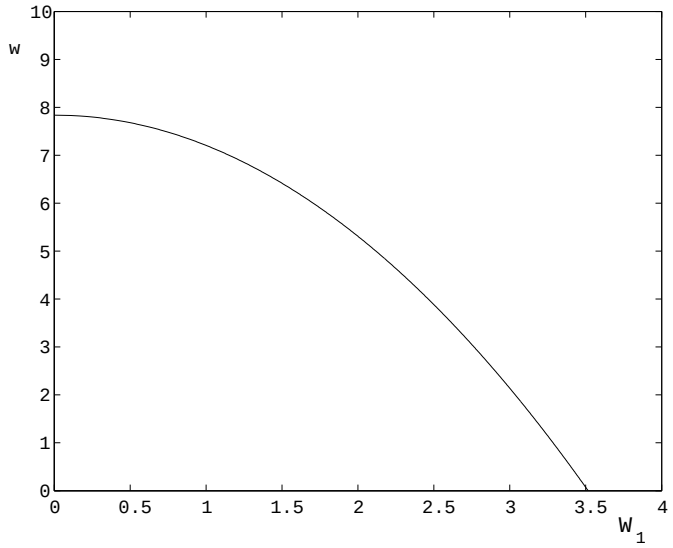

Figure 1.5: Self-weight versus frequency for the upright heavy prebuckled cantilever.

As w is increased, the first natural frequency decreases, as shown in Figure 1.5. The w-value for which the frequency, Ω_1, drops to zero is found to be $w = 7.837$, consistent with the critical self-weight buckling value previously shown in the static heavy cantilever analysis [1, 3].

A similar analysis may be performed for the vertical, hanging, heavy cantilever (shown with the upright case in Figure 1.6), where the nondimensional weight parameter, w, may now be negative (corresponding to the hanging configuration). Note that, although the case of $w = 0$ corresponds to a gravity-free system, in practice it can be considered equivalent to the case of a short horizontal cantilever.

If the bending stiffness of the beam is negligible (for the hanging orientation), then the classic hanging chain solution is obtained, where the first few natural frequencies are:

$$\omega_j = \gamma_j \sqrt{\frac{g}{L}}, \quad \gamma_j = 1.203(j=1), 2.760(j=2), 4.327(j=3)...., \tag{1.31}$$

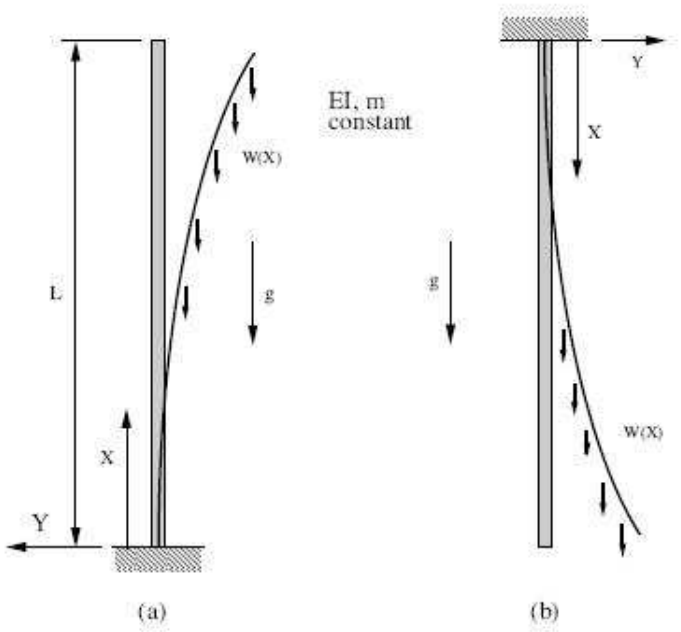

Figure 1.6: The heavy, vertical cantilever, (a) upright and (b) hanging configurations.

obtained numerically (for $w \to \infty$) or with the use of Bessel functions [12]. The first four natural frequencies for the upright and hanging configurations are shown in Figure 1.7.

Again, use of the exact-curvature equation was not necessary to determine the linear vibration frequencies for the vertical cantilever because the static configuration was not highly-deflected and only small-amplitude vibrations were of interest. The exact-curvature equation is necessary, however, for the analysis of linear vibrations about a nonlinear static configuration (the third category from the left shown in the bottom row of Figure 1.1), but the assumption of small dynamic deflections may be used to simplify the problem.

The case of nonlinear vibrations about a nonlinear equilibrium configuration (the rightmost category in Figure 1.1) is the most involved, in terms of solution approximation, but can be modeled using analytical or numerical methods. For linear dynamic systems, the natural frequency is not amplitude-dependent; the frequency is assumed to be constant regardless of the magnitude of motion. However, in the case of a nonlinear dynamic system, the natural frequency may vary as a function of motion amplitude. This amplitude-dependent frequency may increase (for a "hardening" system) or decrease (for a "softening" system) with the magnitude of motion [13]. The resulting "backbone" curves for the prebuckled, heavy, upright cantilever (Figure 1.2) are plotted in Figure 1.8, where, for each self-weight value, the nonlinear frequency, Ω_{N1}, is normalized by the

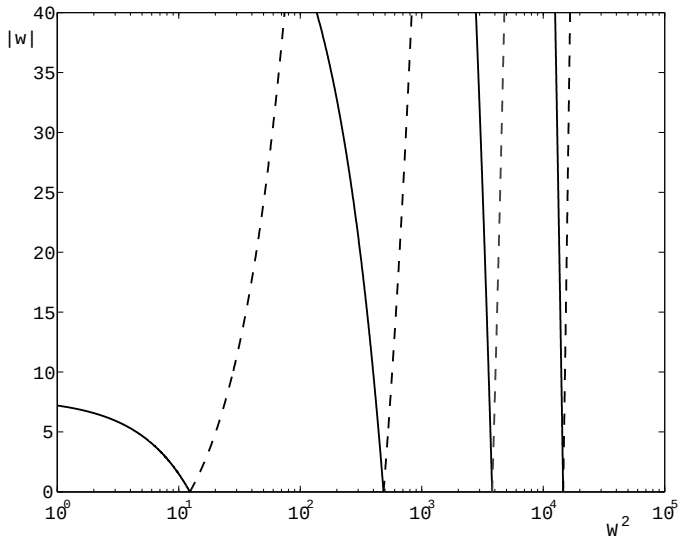

Figure 1.7: The four lowest vertical cantilever frequencies, solid curve: upright, dashed curve: hanging.

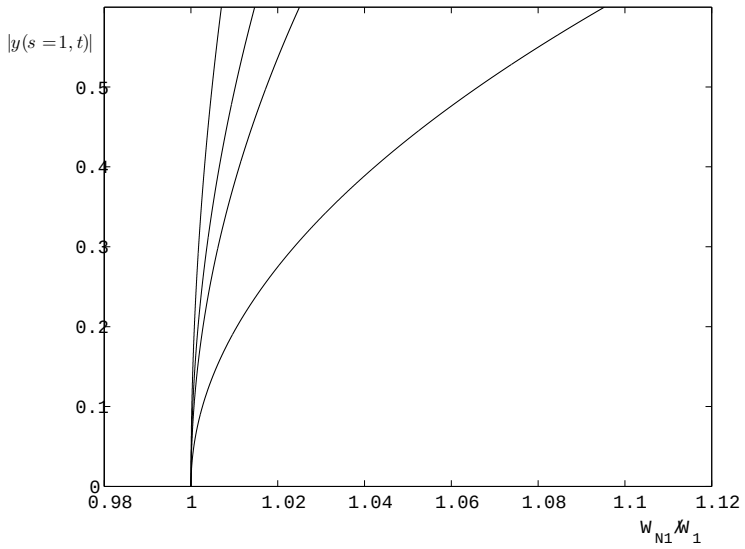

Figure 1.8: Backbone curves for the nonlinear vibration of the upright heavy cantilever, for nondimensional weights (from left to right) $w = 0, 1.655, 2.989, 5.859$.

corresponding linear natural frequency, Ω_1 (shown in Figure 1.5). It can be seen that an increase in self-weight yields an increasingly hardening system.

Solution methods for each of the cases shown in Figure 1.1 are shown in the Sections to follow.

1.2 The Elastica

Use of the exact expression for curvature (equation 1.5) yields an exact solution, and the equation can be written in first-order form (including the equations that give resulting Cartesian coordinates) using Figure 1.9. The resulting equilibrium shape is called the elastica, and the governing equations

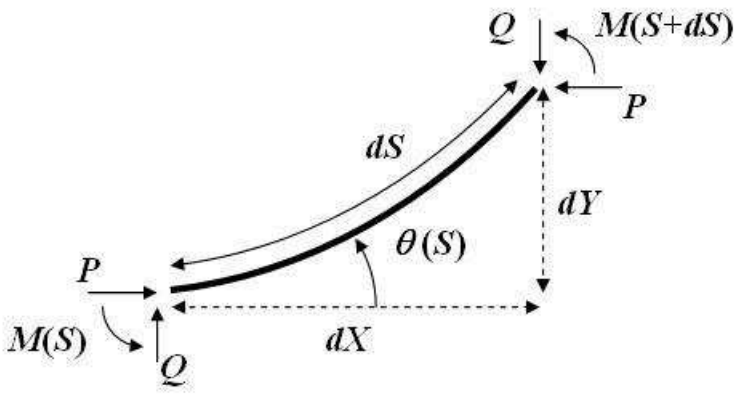

Figure 1.9: Arclength segment of the elastica.

for the inextensible, slender, heavy beam of fixed length are [1]

$$\begin{array}{ll} dX/dS = \cos\theta, & dY/dS = \sin\theta, \\ d\theta/dS = M/EI, & dM/dS = Q\cos\theta - P\sin\theta, \\ dP/dS = -W\sin\beta, & dQ/dS = -W\cos\beta, \end{array} \tag{1.32}$$

where P and Q are the internal forces parallel to the X and Y axes, respectively, and β is the angle made by the X-axis with the horizontal. The strip is assumed to be thin, flexible, inextensible, unshearable, and unstrained when straight [14].

If dynamics are included in the analysis, each variable becomes a function of both arclength, S,

and time, T. The governing partial differential elastica equations become [15]

$$\begin{gathered}
\partial X/\partial S = \cos\theta, \\
\partial Y/\partial S = \sin\theta, \\
\partial\theta/\partial S = M/EI, \\
\partial M/\partial S = Q\cos\theta - P\sin\theta, \\
\partial P/\partial S = -W\sin\beta - (W/g)\partial^2 X/\partial T^2 - C\partial X/\partial T, \\
\partial Q/\partial S = -W cos\beta - (W/g)\partial^2 Y/\partial T^2 - C\partial Y/\partial T,
\end{gathered} \tag{1.33}$$

where C is the damping coefficient.

In addition to the nondimensional variables given in equation 1.25, the following nondimensional quantities are defined:

$$\begin{gathered}
s = S/L, \quad p = PL^2/EI, \quad q = QL^2/EI, \\
m = ML/EI, \quad c = CL^2\sqrt{g/WEI}, \quad \Omega = \omega L^2\sqrt{W/EIg}
\end{gathered} \tag{1.34}$$

where ω is a dimensional vibration frequency. In nondimensional terms, equations (1.33) become

$$\begin{array}{ll}
\partial x/\partial s = \cos\theta, & \partial y/\partial s = \sin\theta, \\
\partial\theta/\partial s = m, & \partial m/\partial s = q\cos\theta - p\sin\theta, \\
\partial p/\partial s = -w\sin\beta - \partial^2 x/\partial t^2 - c\partial x/\partial t, & \partial q/\partial s = -w\cos\beta - \partial^2 y/\partial t^2 - c\partial y/\partial t.
\end{array} \tag{1.35}$$

Assuming small-amplitude vibrations about the equilibrium configuration and that damping is negligible ($c = 0$), the variables may be written in the form

$$\begin{array}{ll}
x(s,t) = x_e(s) + x_d(s)\sin\Omega t, & y(s,t) = y_e(s) + y_d(s)\sin\Omega t, \\
\theta(s,t) = \theta_e(s) + \theta_d(s)\sin\Omega t, & m(s,t) = m_e(s) + m_d(s)\sin\Omega t, \\
p(s,t) = p_e(s) + p_d(s)\sin\Omega t, & q(s,t) = q_e(s) + q_d(s)\sin\Omega t
\end{array} \tag{1.36}$$

where subscripts e and d denote equilibrium and dynamic quantities, respectively. At equilibrium, the equations are given by

$$\begin{array}{ll}
x_e' = \cos\theta_e, & y_e' = \sin\theta_e, \\
\theta_e' = m_e, & m_e' = q_e\cos\theta_e - p_e\sin\theta_e, \\
p_e' = -w\sin\beta, & q_e' = -w\cos\beta,
\end{array} \tag{1.37}$$

where the internal forces can be written as

$$p_e(s) = p_o - sw\sin\beta, \quad q_e(s) = q_o - sw\cos\beta \tag{1.38}$$

with p_0 and q_0 representing values at $s = 0$.

Equations 1.36 are substituted into equations 1.35, and equations 1.37 are utilized. The resulting linear equations in the dynamic variables are

$$\begin{array}{ll} x'_d = -\theta_d \sin\theta_e, & y'_d = \theta_d \cos\theta_e, \\ \theta'_d = m_d, & m'_d = (q_d - p_e\theta_d)\cos\theta_e - (p_d + q_e\theta_d)\sin\theta_e, \\ p'_d = \Omega^2 x_d, & q'_d = \Omega^2 y_d. \end{array} \tag{1.39}$$

There is extensive work on the elastica in the literature. Early work was conducted by Timoshenko and Gere [1], Wang [15], and Frisch-Fay [16], and later work is outlined by Stolte and Benson [17].

1.3 Numerical Techniques

The elastica equations (along with appropriate boundary conditions) may be solved numerically. Some numerical techniques for similar problems are outlined by Hermann and Kaiser [18]. Presented here are the shooting method and the finite difference method.

1.3.1 The Shooting Method

The shooting method is used to solve a boundary value problem by treating it as an initial value problem. An n^{th}-order boundary value problem

$$\tfrac{d\vec{u}}{dx} = \vec{g}(\vec{u}), \quad \vec{u}(x_0) = \vec{u_0}, \quad \vec{u}(x_1) = \vec{u_1} \tag{1.40}$$

can often be solved numerically (using a Runge Kutta method) if the value of $\vec{u}(x_0)$ is known and if use of this known value, upon solving, satisfies $\vec{u}(x_1) = \vec{u_1}$. For each unknown initial value, a shooting parameter (or set of parameters) is used as a guess and the differential equation is solved numerically. The known end conditions, $\vec{u}(x_1)$, can then be compared to the value resulting from the guess, and the shooting parameter is then adjusted until the error at x_1 is sufficiently small.

The differential equations herein are solved using the routines NDSolve in Mathematica and ode45 in MATLAB. More information concerning the shooting method is given by Burden and Faires [19].

1.3.2 Single Parameter Shooting

Suppose that, for a second-order differential equation given by

$$\tfrac{d\vec{u}}{dx} = \vec{g}(\vec{u}), \quad \vec{u} = \begin{pmatrix} u(x) \\ v(x) \end{pmatrix}, \tag{1.41}$$

the boundary conditions known are

$$u(0) = u_0, \quad u(1) = u_1. \tag{1.42}$$

Assigning a value, α, to the unknown $v(0)$ creates a numerically-solvable initial value problem given by

$$\frac{d\vec{u}}{dx} = \vec{g}(\vec{u}), \quad u(0) = u_0, \quad v(0) = \alpha. \tag{1.43}$$

The system can be solved numerically, and the resulting value of $u(1)$ is compared to the desired value, u_1.

An objective function, $f(\alpha)$, can then be defined so that it gives the difference between the resulting function value (from a chosen α) and the known boundary value, i.e.

$$f(\alpha) = u(1, \alpha) - u_1. \tag{1.44}$$

The objective function, then, gives the error of the solution as a function of the shooting parameter, α, so the exact boundary condition, $v(0) = \alpha^\star$ satisfies

$$u(1, \alpha^\star) = u_1 \Leftrightarrow f(\alpha^\star) = 0. \tag{1.45}$$

It is important to note that, for certain cases, the objective function may have more than one root. Some reasonable estimate for the value of the desired $\alpha^\star$ is necessary in these cases. This exact value, $\alpha^\star$, can be found within any desired error (limited, of course, by machine precision) using, for example, a binary search method or the more efficient Newton's Method that iteratively defines the more accurate α_{k+1} by

$$\alpha_{k+1} = \alpha_k - \frac{f(\alpha_k)}{f'(\alpha_k)}. \tag{1.46}$$

The derivative, $f'(\alpha_k) \equiv \frac{\partial f}{\partial \alpha}(\alpha_k)$, can be estimated using finite differences or by introducing a new variable vector. Because it is the technique that is used in the present study for multiparameter shooting, the latter choice is introduced.

The vector function, $\vec{b} = \begin{pmatrix} b(x) \\ c(x) \end{pmatrix}$, is defined such that

$$\vec{b}(x) = \frac{\partial \vec{u}}{\partial \alpha}, \tag{1.47}$$

and the original differential equation (1.41) is used to show

$$\frac{d\vec{b}}{dx} = \frac{d}{dx}(\frac{\partial \vec{u}}{\partial \alpha}) = \frac{\partial}{\partial \alpha}(\frac{d\vec{u}}{dx}) = \frac{\partial}{\partial \alpha}\vec{g}(\vec{u}) = \frac{d\vec{g}}{d\vec{u}}\frac{\partial \vec{u}}{\partial \alpha} = \frac{d\vec{g}}{d\vec{u}}\vec{b}. \tag{1.48}$$

The new, fourth-order differential equation

$$\tfrac{d\vec{u}}{dx} = \vec{g}(\vec{u}), \quad \tfrac{d\vec{b}}{dx} = \tfrac{d\vec{g}}{d\vec{u}}\vec{b}, \tag{1.49}$$

has initial values

$$\begin{aligned} &u(0) = u_0, && v(0) = \alpha, \\ &b(0) = \tfrac{\partial u(0)}{\partial \alpha} = \tfrac{\partial u_0}{\partial \alpha} = 0, && c(0) = \tfrac{\partial v(0)}{\partial \alpha} = \tfrac{\partial \alpha}{\partial \alpha} = 1. \end{aligned} \tag{1.50}$$

Using equation (1.44), the value of $f'(\alpha_k)$ needed for the Newton iterations is now given by

$$f'(\alpha_k) = \frac{\partial}{\partial \alpha}u(1, \alpha_k) = c(1), \tag{1.51}$$

found by having numerically solved the fourth-order differential equation using $\alpha = \alpha_k$.

For the case of the upright, prebuckled, heavy cantilever, $\beta = \pi/2$, and the boundary conditions are given by

$$x(0) = y(0) = \theta(0) = 0, \quad m(1) = p(1) = q(1) = 0. \tag{1.52}$$

The resulting equilibrium elastica equations become

$$\begin{aligned} &dx/ds = \cos\theta, && dy/ds = \sin\theta, \\ &d\theta/ds = m, && dm/ds = -w(1-s)\sin\theta, \end{aligned} \tag{1.53}$$

where $p(s) = w(1-s)$ and $q(s) = 0$.

The exact solution curve pictured in Figure 1.3 can be found using equations 1.53 and the boundary conditions given in equation 1.52. Because the variables $x(s)$ and $y(s)$ are strictly dependent on the variable $\theta(s)$, it is sufficient to solve the boundary value problem of first-order equations

$$\theta' = m, \quad m' = -w(1-s)\sin\theta, \quad \theta(0) = m(1) = 0, \tag{1.54}$$

and to then use the known initial values $x(0) = y(0) = 0$ and the solution $\theta(s)$ to find the Cartesian deflection coordinates. The shooting parameter is assigned such that $m(0) = \alpha$.

To simplify notation, the vector $\vec{u}$ is written so that

$$\vec{u} = \begin{pmatrix} u_1 \\ u_2 \\ u_3 \end{pmatrix} = \begin{pmatrix} \theta(s) \\ m(s) \\ s \end{pmatrix}, \tag{1.55}$$

giving the differential equation, $g(\vec{u})$, and its partial derivatives

$$\vec{g} = \begin{pmatrix} u_2 \\ -w(1-u_3)\sin u_1 \\ 1 \end{pmatrix}, \quad \frac{d\vec{g}}{d\vec{u}} = \begin{pmatrix} 0 & 1 & 0 \\ -w(1-u_3)\cos u_1 & 0 & w\sin u_1 \\ 0 & 0 & 1 \end{pmatrix}. \tag{1.56}$$

The new vector $\vec{b}$ is introduced such that

$$\vec{b} = \frac{\partial \vec{u}}{\partial \alpha} = \begin{pmatrix} b_1 \\ b_2 \\ b_3 \end{pmatrix}, \tag{1.57}$$

yielding the new initial value problem

$$\frac{d\vec{b}}{ds} = \frac{d\vec{g}}{d\vec{u}}\vec{b} = \begin{pmatrix} b_2 \\ -wb_1(1-u_3)\cos u_1 + wb_3 \sin u_1 \\ b_3 \end{pmatrix}, \quad \vec{b}(0) = \begin{pmatrix} 0 \\ 1 \\ 0 \end{pmatrix}. \tag{1.58}$$

Letting $b_1 = u_4$, $b_2 = u_5$, and $b_3 = u_6$ gives the sixth-order initial value problem

$$\frac{d\vec{u}}{ds} = \begin{pmatrix} u_2 \\ -w(1-u_3)\sin u_1 \\ 1 \\ u_5 \\ -wu_4(1-u_3)\cos u_1 + wu_6 \sin u_1 \\ u_6 \end{pmatrix}, \quad \vec{u}(0) = \begin{pmatrix} 0 \\ \alpha \\ 0 \\ 0 \\ 1 \\ 0 \end{pmatrix}. \tag{1.59}$$

The objective function and its derivative are then

$$f(\alpha) = u_2(1, \alpha), \quad \frac{df}{d\alpha} = u_5(1). \tag{1.60}$$

A specific self-weight, w, must be chosen, and then the system can be solved numerically, using Newton's method (equation 1.46). This single-parameter shooting method was used to find the exact relationship between the cantilever tip angle and the self-weight seen in Figure 1.3. Using the initial value $m(0) = \alpha$ found for a specific weight, equations 1.53 may be solved as an initial value problem using numerical integration to determine the exact deformation along the length of the beam (as pictured in Figure 1.4).

1.3.3 Multi-parameter Shooting

Suppose that, for an n^{th}-order system of differential equations

$$\frac{d\vec{u}}{dx} = \vec{g}(\vec{u}), \tag{1.61}$$

there exist $r < n$ known boundary conditions at x_0 and $n - r$ known boundary conditions at x_1.

As in single-parameter shooting, values α are assigned to the unknown boundary values at x_0, and, because there can be more than one unknown value, the scalar α now becomes an $n - r$ component vector, $\vec{\alpha}$. The vector-valued objective function, $\vec{f}(\vec{\alpha})$, is constructed using the $n - r$ known boundary values at x_1.

Just as for the single-parameter shooting method, new vectors are defined that correspond to each α_j such that

$$\vec{b_j} = \frac{\partial \vec{u}}{\partial \alpha_j}, \quad \frac{d\vec{b_j}}{dx} = \frac{d\vec{g}}{d\vec{u}}\vec{b_j}, \quad j = 1, 2, \ldots, n - r, \tag{1.62}$$

yielding a system of differential equations of order $(n - r + 1)n$. The vector equivalent form of the Newton iteration equation is given by

$$\vec{\alpha}_{k+1} = \vec{\alpha}_k - J_{\vec{\alpha}_k}^{-1}\vec{f}(\vec{\alpha}_k), \quad J_{\vec{\alpha}_k} = \left[\frac{\partial f_i}{\partial \alpha_j}\right]_{\vec{\alpha}_k}, \tag{1.63}$$

where the matrix components of the Jacobian are found in the solutions, $\vec{b_j}(x_1)$. The exact boundary conditions, $\vec{\alpha}^\star$, can now be found within any desired error, $|\vec{f}|$.

For the case of small-amplitude beam bending vibrations, the governing equations 1.39 and appropriate boundary conditions may be solved using the multi-parameter shooting method. For the vibration of the upright, heavy, prebuckled cantilever, the trivial equilibrium solution is given by

$$x_e(s) = s, \quad y_e(s) = \theta_e(s) = m_e(s) = q_e(s) = 0, \quad p_e(s) = w(1 - s), \tag{1.64}$$

and the simplified dynamic variable equations are

$$\begin{array}{ll} y_d' = \theta_d, & \theta_d' = m_d, \\ m_d' = (q_d - w(1 - s)\theta_d), & q_d' = \Omega^2 y_d, \end{array} \tag{1.65}$$

where $x_d(s) = p_d(s) = 0$. The known boundary conditions are $y_d(0) = \theta_d(0) = m_d(1) = q_d(1) = 0$ and $m_d(0) = \bar{m}_d$, where $\bar{m}_d$ is arbitrary (yet small), because it determines only the magnitude of vibration. The shooting parameter vector and objective function are

$$\vec{\alpha} = \begin{pmatrix} q_d(0) \\ \Omega^2 \end{pmatrix}, \quad \vec{f}(\vec{\alpha}) = \begin{pmatrix} m_d(1, \vec{\alpha}) \\ q_d(1, \vec{\alpha}) \end{pmatrix}, \tag{1.66}$$

respectively. Because the square of the natural frequency, Ω^2, has infinitely many values (corresponding to each mode), an initial guess for its value must be made according to the desired mode.

Shooting method results for the frequencies as functions of self-weight are shown in Figures 1.5 and 1.7. The mode shape resulting from this method (with $w = 0$) is compared with the analytical mode shape (given by equation 1.23) in Figure 1.10.

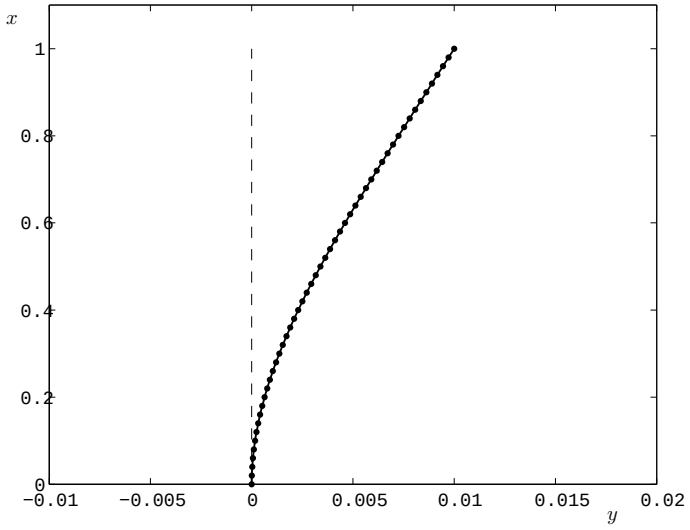

Figure 1.10: Numerical and analytical mode shape for vibration of the cantilever in the first mode (with $w = 0$): solid curve: analytical; data points: numerical (using the shooting method); dashed curve: equilibrium.

While the shooting method is useful in determining unknown initial conditions for a boundary value problem, it becomes more involved as the number of shooting parameters (or the size of $\vec{\alpha}$) is increased. Another numerical method that may be used in these cases is the finite difference method.

1.3.4 Finite Differences

For a single-variable function, $y(x)$, the Taylor Series about some point, x_o, is given by

$$y(x_o + h) = y(x_o) + y'(x_o)h + \frac{y''(x_o)}{2!}h^2 + \frac{y'''(x_o)}{3!}h^3 + \ldots, \tag{1.67}$$

and can be used to approximate the function value, $y(x_o + h)$, with increasing accuracy as more terms in the series are used. This approximation technique is the basis for the finite difference method, and the equation

$$\frac{y(x_o + h) - y(x_o)}{h} = \bar{y}'(x_0) \approx y'(x_o) \tag{1.68}$$

is the familiar Euler difference scheme, where $\bar{y}'(x_0)$ is the resulting derivative approximation. Comparing this scheme to a rewritten Taylor Series given by

$$\frac{y(x_o+h)-y(x_o)}{h} = y'(x_o) + \frac{y''(x_o)}{2!}h + \frac{y'''(x_o)}{3!}h^2 + \ldots, \tag{1.69}$$

and subtracting equation 1.68 from equation 1.69 shows that the approximation has error, $|\bar{y}'(x_0) - y'(x_0)|$, of order h. An approximation for the first derivative, $y'(x_o)$, with 2nd-order accuracy can be found by using the function values at $x_o - h$ and $x_o + h$. That is, the coefficients, c_k, may be found such that

$$c_1 y(x_o - h) + c_2 y(x_o + h) = y'(x_o) + O(h^2). \tag{1.70}$$

Expanding each term on the left hand side of equation 1.70 using a Taylor Series about x_o gives

$$\begin{aligned} y(x_o+h) &= y(x_o) + y'(x_o)h + \tfrac{y''(x_o)}{2!}h^2 + \tfrac{y'''(x_o)}{3!}h^3 + \ldots, \\ y(x_o-h) &= y(x_o) - y'(x_o)h + \tfrac{y''(x_o)}{2!}h^2 - \tfrac{y'''(x_o)}{3!}h^3 + \ldots, \end{aligned} \tag{1.71}$$

To satisfy equation 1.70, the coefficients of $y(x_o)$ and $y'(x_o)$ (where equations 1.71 are substituted into equation 1.70) must satisfy

$$c_2 + c_1 = 0, \quad (c_2 - c_1)h = 1, \tag{1.72}$$

giving $c_1 = -1/2h$ and $c_2 = 1/2h$. The simplified Taylor Series expansion resulting from this linear combination gives

$$\frac{y(x_o+h)-y(x_o-h)}{2h} = y'(x_o) + \frac{2y'''(x_o)}{3!}h^2 + \ldots, \tag{1.73}$$

indicating that this centered difference scheme

$$\frac{y(x_o+h)-y(x_o-h)}{2h} \approx y'(x_o) \tag{1.74}$$

is 2nd-order accurate. Other difference schemes have been derived for higher-order derivatives and for higher orders of accuracy [20].

The centered difference scheme may be used to find the numerical solution to the boundary value problem given by equation 1.54. First, the equations are rewritten

$$\theta' - m = 0, \quad m' + w(1-s)\sin\theta = 0. \tag{1.75}$$

The values $\theta(s)$ and $m(s)$ may be discretized along the arclength, s, so that

$$\theta_k = \theta(s_k), \quad m_k = m(s_k), \quad s_k = (k-1)\Delta s, \quad k = 1, 2, \ldots n+1, \tag{1.76}$$

where $n = 1/\Delta s$, and $n+1$ is the number of points (or nodes) along the length. A vector, $\vec{u}$, of node values is created so that

$$\vec{u} = \begin{pmatrix} u_1 \\ u_2 \\ \vdots \\ u_{2n+1} \\ u_{2n+2} \end{pmatrix} = \begin{pmatrix} \theta_1 \\ m_1 \\ \vdots \\ \theta_{n+1} \\ m_{n+1} \end{pmatrix} \tag{1.77}$$

Using the centered difference scheme given by equation 1.74, where $2h = \Delta s$, the derivatives between each node may be approximated. Because the right hand sides of equations 1.75 are zero, the values found by the approximations

$$\tfrac{\theta_{k+1}-\theta_k}{\Delta s} - \tfrac{m_k+m_{k+1}}{2}, \quad \tfrac{m_{k+1}-m_k}{\Delta s} + w(1-s_{k+1/2})\sin\left(\tfrac{\theta_k+\theta_{k+1}}{2}\right) \tag{1.78}$$

give the approximation error, where $s_{k+1/2} = (s_k + s_{k+1})/2$, and $k = 1, 2, \ldots, n$. This method generates $2n$ equations, but because there are $2(n+1)$ unknown values, two more equations are necessary to find all of the node values. These remaining equations enforce the boundary conditions $\theta(0) = u_1 = m(1) = u_{2n+2} = 0$. These error equations, along with the finite difference errors, may be written as a vector function, $\vec{f}(\vec{u})$, where

$$\begin{aligned} f_1 &= u_1 - 0, \\ f_{2k} &= \tfrac{u_{2k+1}-u_{2k-1}}{\Delta s} - \tfrac{u_{2k}+u_{2k+2}}{2}, \\ f_{2k+1} &= \tfrac{u_{2k+2}-u_{2k}}{\Delta s} + w(1-(k-1/2)\Delta s)\sin\left(\tfrac{u_{2k-1}+u_{2k+1}}{2}\right), \\ f_{2n+2} &= u_{2n+2} - 0, \end{aligned} \tag{1.79}$$

and $k = 1, 2, \ldots, n$. To compute these error vector values, initial values $\vec{u}_o$ are necessary for all $n+1$ nodes along the length. Once $\vec{f}(\vec{u}_o)$ is computed, the Newton-Raphson method (as shown in equation 1.63) may be used to find the variable values that minimize the error, $|\vec{f}|$. Because the

error function, $\vec{f}(\vec{u})$, is a vector, the Jacobian matrix must be computed. This matrix is given by

$$J = \partial f_i/\partial u_j = \begin{pmatrix} 1 & 0 & 0 & 0 & 0 & 0 & \cdots & 0 \\ -\frac{1}{\Delta s} & -\frac{1}{2} & \frac{1}{\Delta s} & -\frac{1}{2} & 0 & 0 & \cdots & 0 \\ d_1 & -\frac{1}{\Delta s} & d_1 & \frac{1}{\Delta s} & 0 & 0 & \cdots & 0 \\ 0 & 0 & -\frac{1}{\Delta s} & -\frac{1}{2} & \frac{1}{\Delta s} & -\frac{1}{2} & \ddots & 0 \\ 0 & 0 & d_2 & -\frac{1}{\Delta s} & d_2 & \frac{1}{\Delta s} & \ddots & 0 \\ \vdots & \vdots & \vdots & \ddots & \ddots & \ddots & \ddots & 0 \\ 0 & 0 & 0 & \cdots & -\frac{1}{\Delta s} & -\frac{1}{2} & \frac{1}{\Delta s} & -\frac{1}{2} \\ 0 & 0 & 0 & \cdots & d_n & -\frac{1}{\Delta s} & d_n & \frac{1}{\Delta s} \\ 0 & 0 & 0 & \cdots & 0 & 0 & 0 & 1 \end{pmatrix}, \tag{1.80}$$

where

$$d_j = \tfrac{1}{2} w \left[1 - \left(j - \tfrac{1}{2}\right) \Delta s\right] \cos\left(\tfrac{u_{2j-1}+u_{2j+1}}{2}\right), \quad j = 1, 2, \cdots, n. \tag{1.81}$$

The matrix is banded, and so sparse matrix algorithms may be used to reduce computation time [21]. The resulting vector, $\vec{u}$ (for which $|\vec{f}(\vec{u})|$ is minimized), gives converged values for θ_k and m_k at $n+1$ nodes along the length $0 \leq s \leq 1$.

As with the shooting method, a converged solution may be used as an initial guess for the problem with a slightly different parameter value. This method is useful when the relationship between equilibrium behavior and a parameter value is desired. In this case, using a solution vector for a given self-weight as the initial guess vector where the self-weight is slightly different may be used to determine the effect of self-weight, w (as shown in Figure 1.3 where the self-weight is plotted against the tip angle, $\theta(1) = \theta_{n+1} = u_{2n+1}$). More on this continuation method is given by Allgower and Georg [22].

1.3.5 Finite Difference Time-Stepping

The finite difference method may also be used in the context of large-amplitude motion of the elastica. In equations 1.36, the variables are separated into equilibrium and dynamic components, damping is neglected, and the dynamic components are also assumed to be the product of spatial and temporal functions. These assumptions, along with that of small-amplitude motion, greatly simplify the equations and allow for a reduction to ordinary differential equations 1.37 and 1.39.

By solving the original partial differential equations 1.35, without assuming the form or size of the variables, the behavior may be found without any limits on the magnitude of static or dynamic deflection.

As before, the equations are rewritten

$$\begin{array}{ll} \partial x/\partial s - \cos\theta = 0, & \partial y/\partial s - \sin\theta = 0, \\ \partial\theta/\partial s - m = 0, & \partial m/\partial s - q\cos\theta + p\sin\theta = 0, \\ \partial p/\partial s + w\sin\beta + \partial^2 x/\partial t^2 + c\partial x/\partial t = 0, & \partial q/\partial s + w\cos\beta + \partial^2 y/\partial t^2 + c\partial y/\partial t = 0. \end{array} \tag{1.82}$$

The variables can then be discretized along the arclength, s, and in time, t, such that

$$\begin{array}{lll} x_k^j = x(s_k, t^j), & y_k^j = y(s_k, t^j), & \theta_k^j = \theta(s_k, t^j), \\ m_k^j = m(s_k, t^j), & p_k^j = p(s_k, t^j), & q_k^j = q(s_k, t^j), \end{array} \tag{1.83}$$

where $t^j = j\Delta t$, $s_k = k\Delta s$, $\Delta s = 1/n$, and $n+1$ is the number of arclength nodes.

Finite difference approximations can then be used to rewrite equations 1.82 that give the approximation error at the k^{th} node and j^{th} time step. To do this, the centered difference scheme may be used for spatial derivative approximations, but another method is needed to approximate the time derivatives. A centered difference scheme would not be useful, since a solution is found at each consecutive time step and only the variable values at previous time steps are known. The necessary second-order difference scheme for the acceleration term is found by finding the constants, c_i, such that

$$c_1 z(x_o) + c_2 z(t_o - h) + c_3 z(t_o - 2h) + c_4 z(t_o - 3h) = z''(t_o) + O(h^2). \tag{1.84}$$

These values are found by expanding each term using a Taylor Series about t_o and combining the coefficients of h^o, h^1, h^2, and h^3. The resulting coefficients are

$$c_1 = 2/h^2, \quad c_2 = -5/h^2, \quad c_3 = 4/h^2, \quad c_4 = -1/h^2, \tag{1.85}$$

giving a second-order-accurate backward difference scheme. Similarly, the appropriate coefficients may be found for the second order accurate approximations of the velocity expressions. Then at a given time step, t^j, and between nodes k and $k+1$, the finite difference approximations of the left hand sides of equations 1.82 are given by

$$\begin{array}{c} \frac{x_{k+1}^j - x_k^j}{\Delta s} - \cos\theta_{k+1/2}^j, \\ \frac{y_{k+1}^j - y_k^j}{\Delta s} - \sin\theta_{k+1/2}^j, \\ \frac{\theta_{k+1}^j - \theta_k^j}{\Delta s} - m_{k+1/2}^j, \\ \frac{m_{k+1}^j - m_k^j}{\Delta s} - q_{k+1/2}^j\cos\theta_{k+1/2}^j + p_{k+1/2}^j\sin\theta_{k+1/2}^j, \\ \frac{p_{k+1}^j - p_k^j}{\Delta s} + w\sin\beta + \frac{2x_{k+1/2}^j - 5x_{k+1/2}^{j-1} + 4x_{k+1/2}^{j-2} - x_{k+1/2}^{j-3}}{\Delta t^2} + \frac{c(3x_{k+1/2}^j - 4x_{k+1/2}^{j-1} + x_{k+1/2}^{j-2})}{2\Delta t}, \\ \frac{q_{k+1}^j - q_k^j}{\Delta s} + w\cos\beta + \frac{2y_{k+1/2}^j - 5y_{k+1/2}^{j-1} + 4y_{k+1/2}^{j-2} - y_{k+1/2}^{j-3}}{\Delta t^2} + \frac{c(3y_{k+1/2}^j - 4y_{k+1/2}^{j-1} + y_{k+1/2}^{j-2})}{2\Delta t}, \end{array} \tag{1.86}$$

where the variable values at node $k + 1/2$ are given by the average of the values at nodes k and $k + 1$. The variable values at time steps t^{j-3}, t^{j-2}, and t^{j-1} are known from previous, converged solutions. To initialize the algorithm, the values for these previous time steps may be set to create an initial acceleration, velocity, or displacement. Alternatively, the system may undergo forcing; this case may be modeled by enforcing time-varying boundary conditions.

Each expression, applied between every node along the length, gives an approximation error and can be arranged as an error vector, $\vec{f}$. This vector has length $6n$, and the remaining 6 equations are comprised of the boundary conditions, giving $6n + 6$ difference equations to be solved for $6n + 6$ unknown variable values. In the case of the upright heavy cantilever, the boundary conditions $x_1 = y_1 = \theta_1 = m_{n+1} = p_{n+1} = q_{n+1} = 0$, are used to create the remaining components of the error vector.

Because the difference equations 1.86 make no assumptions as to the static or dynamic deflection size, they can be used to characterize large-amplitude dynamic behavior about a highly deflected equilibrium configuration. However, they also give accurate results for linear vibration behavior.

The equations are used to create a time series for the linear, undamped vibration of a "weightless" cantilever ($w = 0$). A linear mode shape is used to initialize the variable values, and the resulting time series is shown in Figure 1.11(a), where the tip angle, $\theta(1, t)$, is plotted as a function of nondimensional time, t. Values of $\Delta t = 0.002$ and $\Delta s = 0.02$ are used to generate results. The average period of vibration in nondimensional time is 1.787, giving $\Omega_1 \approx 3.516$, the known linear vibration frequency coefficient (as in equation 1.30).

To confirm that the motion is harmonic and to find the frequency of motion, a "fast Fourier Transform" may be performed on the time series. The discrete Fourier transform of a set of discrete function values $f(t^j)$ over N time steps ($j = 1, 2, \ldots, N$) is given by [21]

$$P_r = \sum_{j=1}^{N} f(t_j) \left(e^{-2\pi i/N} \right)^{(j-1)(r-1)}, \tag{1.87}$$

giving the Fourier coefficients of the time series at discrete frequency values,

$$f_r = (1/\Delta t)(r - 1)/N, \tag{1.88}$$

for $r = 1, 2, \cdots, N/2$. It is expected, then, that the peaks in magnitude of the Fourier Transform of the free vibration time series correspond to natural frequencies.

The resulting tip-angle magnitude of motion as a function of nondimensional frequency, Ω, is shown in Figure 1.11(b), resulting from a time series using $N = 50{,}000$. The magnitude of the

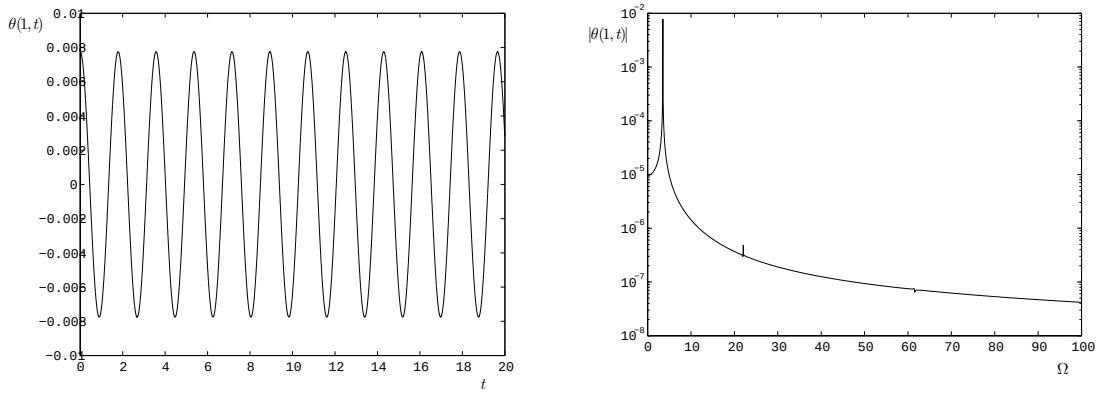

(a) (b)

Figure 1.11: (a) Tip angle, $\theta(s = 1, t)$, as a function of nondimensional time, t, found using a finite difference, time-stepping method for small-amplitude vibration of a cantilever (with $w = 0$) (b) Fourier transform of the tip angle magnitude of vibration of a cantilever (with $w = 0$)

Fourier Transform of the tip angle, θ_{n+1}, is largest at $\Omega = 3.5186$. Because the magnitude is given only at discrete frequency values, a weighted average of the frequencies corresponding to the two largest magnitude values, P_a and P_b, is given by

$$\Omega_{avg} = \frac{P_a\Omega_a + P_b\Omega_b}{P_a + P_b}, \tag{1.89}$$

and gives a more accurate peak frequency estimate. In this case, a weighted average gives an accurate value, $\Omega_{avg} \approx 3.5163$. Two other frequency peaks of much smaller magnitudes can be seen in Figure 1.11(b), occurring near the second and third linear natural frequencies (given in equation 1.30). While the motion is expected to be in exclusively the first mode (because the initial configuration was given by the mode shape corresponding to the first natural frequency), the higher modes appear because of the inherent error in finite difference schemes. However, these magnitudes, as can be seen in the Fourier Transform plot, are significantly smaller than that of the first mode, and so the motion is approximated as being purely in the first linear vibration mode. Additionally, the finite width of the funamental frequency peak indicates that there is some very light numerical damping resulting from the finite difference scheme.

If the initial configuration is one that is slightly deflected from equilibrium, but not in a single mode, the resulting Fourier Transform gives frequency peaks at each of the linear vibration frequencies, as shown in Figure 1.12, where frequency peaks are found at weighted average values of

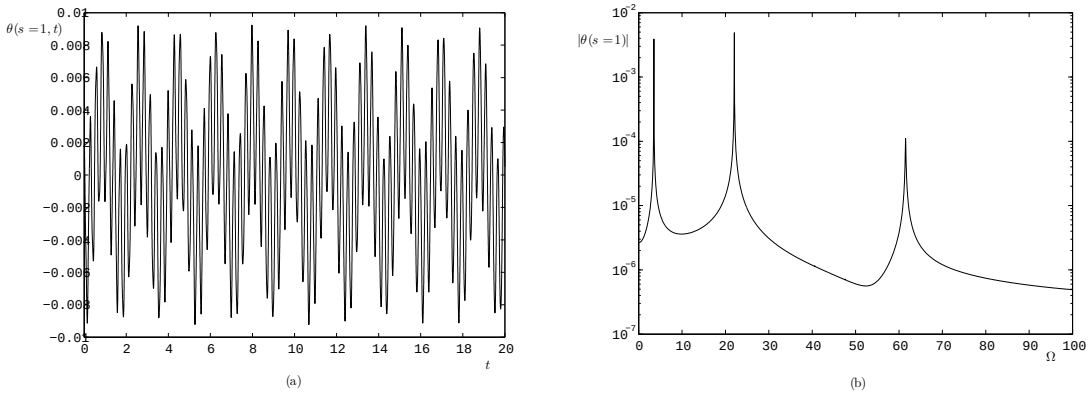

Figure 1.12: (a) Tip angle, $\theta(s = 1, t)$, as a function of nondimensional time, t, for small-amplitude, free vibration of a cantilever (with $w = 0$) (b) Fourier transform of the time series.

$\Omega_1 = 3.516, 22.048$, and 61.541 (compared with the known linear frequency values given in equation 1.30). It is clear in the corresponding time series that more than one frequency is present. The mode shapes for each natural frequency can be approximated using the discrete Fourier Transform values. The zero frequency value, P_1, gives the equilibrium configuration, and the coefficient P_r corresponding to a natural frequency f_r gives the magnitude of response. Using this method, the first two mode shapes for the cantilever are constructed and shown in Figure 1.13, where they are compared to the analytical mode shapes given by equation 1.23. For each analytical mode, the known values $b = 1.875$ and $\sigma = 0.7341$ (for the first mode) and $b = 4.694$ and $\sigma = 1.0185$ (for the second mode) are used [11].

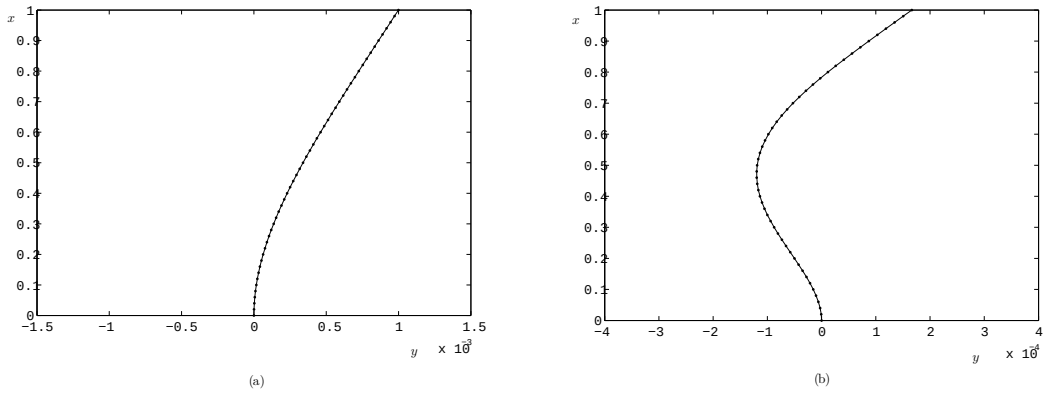

Figure 1.13: Numerical and analytical linear vibration mode shapes for the cantilever with $w = 0$ for the first two linear vibration frequencies, solid curve: analytical mode shape, data points: numerical mode shape.

So far it has been shown that the finite difference, time-stepping method gives accurate linear vibration results for a beam. However, the primary motivation for using the method is to model large-amplitude, nonlinear vibrations of a system (about linear or nonlinear equilibrium configurations). To find nonlinear frequencies and mode shapes, the amplitude of motion is gradually increased and resulting times series and Fourier Transforms are used to determine frequencies.

To execute the finite difference algorithm, the values x_k^{j-1}, x_k^{j-2}, x_k^{j-3}, y_k^{j-1}, y_k^{j-2}, y_k^{j-3} for all the nodes, $k = 1, 2, \ldots, n+1$, must be specified. So far, these values have been used to give an initial deflection with no initial velocity (i.e. $x_k^{j-1} = x_k^{j-2} = x_k^{j-3}$). Another way to begin the solution method is to specify an initial velocity, where the initial deflection is at equilibrium. This method may be used to find mode shapes (and frequencies) with increasingly larger amplitudes. The variable values are recorded for small-amplitude motion as the system passes through equilibrium, and the values are altered slightly to generate a larger initial velocity. These values are then used to initialize the time-stepping method. The Fourier Transform of the resulting time series indicates whether or not the motion was purely in the desired mode, and the resulting coefficients give a corrected mode shape for the desired amplitude. It is important to note that, for large-amplitude motion, the motion is not a pure sine wave of a single natural frequency, and so Fourier coefficients of higher harmonics must be used in determining the mode shape. The new mode shape approximation may be used as an initial condition to give an accurate, single-mode time series, and this time series is used to find an average vibration period and corresponding frequency. This numerical method for finding "nonlinear normal modes" is similar to that proposed by Slater [23], who also outlines other analytical methods in the literature. Some resulting nonlinear normal mode shapes for the upright cantilever are shown in Figure 1.14, where the corresponding frequencies are given by $\Omega_{N1} \approx 3.516$, 3.519, 3.551, 3.627, and 3.656. For the three pictured mode shapes with the smallest deflections from equilibrium, the horizontal tip deflection, $y(s = 1)$, increases with deflection size. But for the remaining mode shapes, the value of $y(s = 1)$ decreases; there is some maximum possible amplitude of horizontal tip deflection, and, for large deflections, the value decreases with deflection. This effect can be seen in the free vibration time series shown in Figure 1.15, where it is clear that the horizontal motion of the cantilever is not accurately described by a single sine wave.

The resulting backbone curve for the first vibration mode of the cantilever is shown in Figure 1.16, where it is seen that the amplitude of horizontal tip deflection motion reaches a maximum (at $|y(1, t)| \approx 0.832$) and then decreases.

This method of gradually increasing the amplitude of motion in a mode can be used to generate

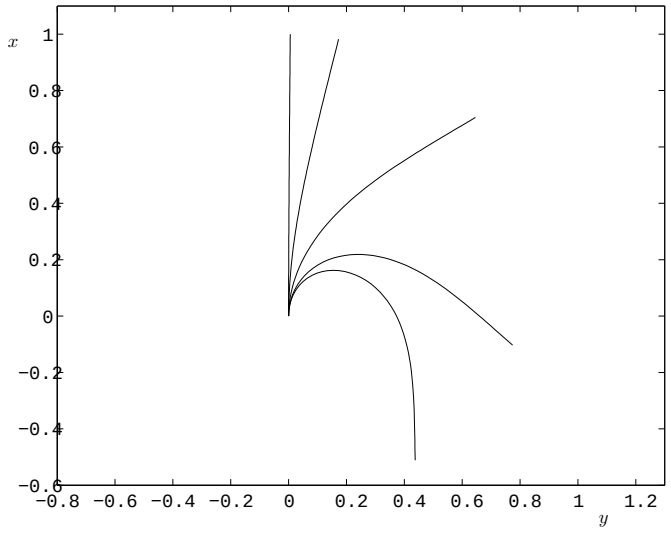

Figure 1.14: Nonlinear vibration mode shapes for an upright cantilever with $w = 0$. Corresponding frequencies for each mode shape (from left to right) are $\Omega_{N1} = 3.516, 3.519, 3.551, 3.627, 3.656$.

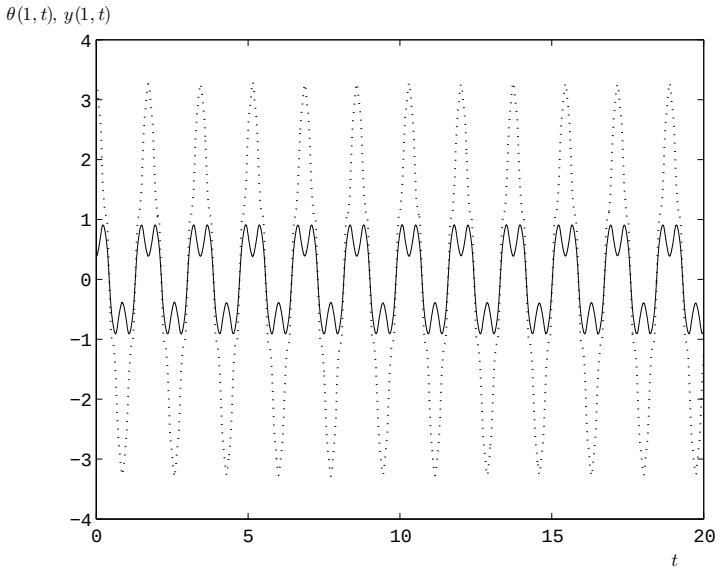

Figure 1.15: Nonlinear vibration time series for an upright cantilever with $w = 0$, solid curve: $y(1, t)$, the lateral tip motion; dotted curve: $\theta(1, t)$, the tip angle.

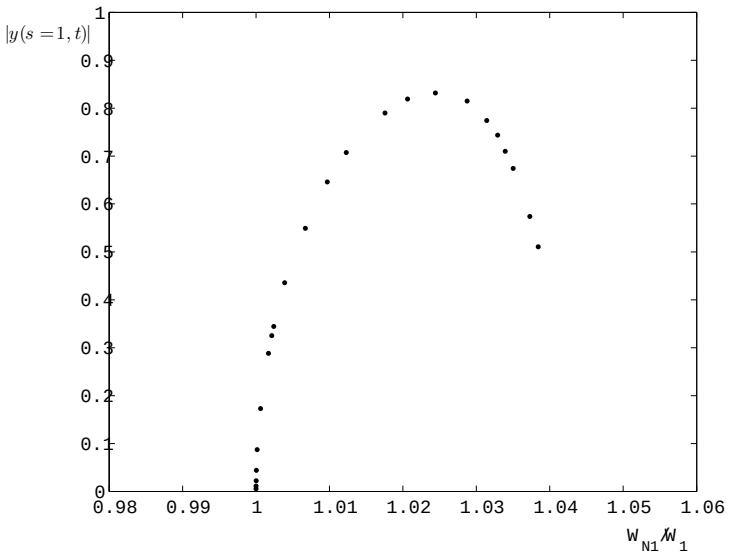

Figure 1.16: Backbone curve for the first vibration mode of a cantilever with $w = 0$ using a finite difference, time-stepping method.

backbone curves for vibration modes of a system. However, the method is not as efficient as other analytical approximation methods that produce accurate (but limited) results for vibrations of moderate amplitude sizes. These methods are presented in Section 1.4.

1.4 Analytical Methods

It has been shown that, for the linear, undamped vibration analysis of the elastica, the partial differential equations 1.35 may be simplified by assuming that the variables are of the form given in equation 1.36. The assumption results in linear ordinary differential equations in the dynamic variables that are easily solved and give accurate linear vibration results.

However, for nonlinear vibrations, the assumption of pure harmonic (or sinusoidal) motion is not valid. To simplify the equations, then, to ordinary differential equations, other assumptions of the variable form may be made. Two such methods, the Galerkin method and a perturbation method, are described here.

1.4.1 The Galerkin Method

One method for approximating the solution (without assuming a sinusoidal dynamic component of the variables) is the Galerkin Method [24]. To employ this method, the form of each of the

variables is assumed such that

$$\begin{aligned} x(s,t) &= x_e(s) + \sum_{j=1}^{n} a_j(t) x_j(s), \\ y(s,t) &= y_e(s) + \sum_{j=1}^{n} b_j(t) y_j(s), \\ \theta(s,t) &= \theta_e(s,t) + \sum_{j=1}^{n} c_j(t) \theta_j(s), \\ p(s,t) &= p_e(s) + \sum_{j=1}^{n} d_j(t) p_j(s), \\ q(s,t) &= q_e(s) + \sum_{j=1}^{n} e_j(t) q_j(s), \end{aligned} \tag{1.90}$$

where, as before, the subscript e denotes the equilibrium solutions (found by solving the boundary value problem defined by the ordinary differential equations 1.37 and the appropriate boundary conditions). The spatial functions, $x_j(s)$, are chosen as the linear mode shapes (found numerically, as shown in Section 1.3). The unknown temporal functions are found using the dynamic elastica equations and an orthogonalization procedure involving numerical integration over arclength of each dynamic equation after multiplication by one of the spatial function or its first derivative.

First, equations 1.90 are substituted into the elastica equations 1.35. For example, the first equation becomes

$$x_e'(s) + \sum_{j=1}^{n} a_j(t) x_j'(s) = \cos\left(\theta_e(s,t) + \sum_{j=1}^{n} c_j(t) \theta_j(s) \right), \tag{1.91}$$

where a prime denotes differentiation with respect to arclength, s. The equations of motion 1.35 and the equilibrium equations 1.37 are used to obtain the equations involving the dynamic variables,

giving

$$\begin{aligned}
\sum_{j=1}^{n} a_j x_j' &= \cos\theta_e \left[\cos\left(\sum_{j=1}^{n} c_j\theta_j\right) - 1\right] - \sin\theta_e \sin\left(\sum_{j=1}^{n} c_j\theta_j\right), \\
\sum_{j=1}^{n} b_j y_j' &= \sin\theta_e \left[\cos\left(\sum_{j=1}^{n} c_j\theta_j\right) - 1\right] - \cos\theta_e \sin\left(\sum_{j=1}^{n} c_j\theta_j\right), \\
\sum_{j=1}^{n} c_j\theta_j'' &= \left(q_e + \sum_{j=1}^{n} e_j q_j\right)\left[\cos\theta_e \cos\left(\sum_{j=1}^{n} c_j\theta_j\right) - \sin\theta_e \sin\left(\sum_{j=1}^{n} c_j\theta_j\right)\right] \\
&\quad - \left(p_e + \sum_{j=1}^{n} d_j p_j\right)\left[\sin\theta_e \cos\left(\sum_{j=1}^{n} c_j\theta_j\right) + \cos\theta_e \sin\left(\sum_{j=1}^{n} c_j\theta_j\right)\right] - q_e\cos\theta_e + p_e\sin\theta_e, \\
\sum_{j=1}^{n} d_j p_j' &= -\sum_{j=1}^{n} \ddot{a}_j x_j - c\sum_{j=1}^{n} \dot{a}_j x_j, \\
\sum_{j=1}^{n} e_j q_j' &= -\sum_{j=1}^{n} \ddot{b}_j y_j - c\sum_{j=1}^{n} \dot{b}_j y_j.
\end{aligned} \tag{1.92}$$

An approximation using series representations of the trigonometric functions may be used to simplify the equations. For example, the first two terms of the series expansions may be used to give the approximations

$$\cos\left(\sum_{j=1}^{n} c_j\theta_j\right) \approx 1 - \tfrac{1}{2}\left(\sum_{j=1}^{n} c_j\theta_j\right)^2, \quad \sin\left(\sum_{j=1}^{n} c_j\theta_j\right) \approx \sum_{j=1}^{n} c_j\theta_j - \frac{1}{6}\left(\sum_{j=1}^{n} c_j\theta_j\right)^3, \tag{1.93}$$

which are used to simplify the dynamic equations 1.92. The first equation, for example, becomes

$$\sum_{j=1}^{n} a_j x_j' = -\sin\theta_e \left(\sum_{j=1}^{n} c_j\theta_j\right) - \frac{1}{2}\cos\theta_e \left(\sum_{j=1}^{n} c_j\theta_j\right)^2 + \frac{1}{6}\sin\theta_e \left(\sum_{j=1}^{n} c_j\theta_j\right)^3. \tag{1.94}$$

If two mode shape functions are used, so that $n = 2$, equation 1.94 can be written

$$a_1 x_1' + a_2 x_2' = -\sin\theta_e \left(c_1\theta_1 + c_2\theta_2\right) - \frac{1}{2}\cos\theta_e \left(c_1\theta_1 + c_2\theta_2\right)^2 + \frac{1}{6}\sin\theta_e \left(c_1\theta_1 + c_2\theta_2\right)^3. \tag{1.95}$$

In the standard Galerkin method, equation 1.95 would be multiplied by x_j and then integrated over arclength for $j = 1$ and $j = 2$. However, the integrals of $x_j x_j^{'}$ over the arclength could be zero. In order to ensure that these terms are nonzero, the equation is multiplied by $x_j^{'}$, yielding nonzero,

positive integrals of $x_j^{'2}$. Multiplying the equation by x_1' and integrating along arclength from $s = 0$ to 1 gives

$$u_1 a_1 + u_2 a_2 = u_3 c_1^3 + u_4 c_1^2 c_2 + u_5 c_1^2 + u_6 c_1 c_2^2 + u_7 c_1 c_2 + u_8 c_1 + u_9 c_2^3 + u_{10} c_2^2 + u_{11} c_2, \tag{1.96}$$

where the constants u_k, defined by

$$\begin{gathered} u_1 = \int_0^1 x_1^{'2} ds, \quad u_2 = \int_0^1 x_1^{'} x_2^{'} ds, \quad u_3 = \tfrac{1}{6} \int_0^1 (\sin\theta_e)\, \theta_1^3 x_1' ds, \\ u_4 = \tfrac{1}{2} \int_0^1 (\sin\theta_e)\, \theta_1^2 \theta_2 x_1' ds, \quad u_5 = -\tfrac{1}{2} \int_0^1 (\cos\theta_e)\, \theta_1^2 x_1' ds, \quad u_6 = \tfrac{1}{2} \int_0^1 (\sin\theta_e)\, \theta_1 \theta_2^2 x_1' ds, \\ u_7 = -\int_0^1 (\cos\theta_e)\, \theta_1 \theta_2 x_1' ds, \quad u_8 = -\int_0^1 (\sin\theta_e)\, \theta_1 x_1' ds, \quad u_9 = \tfrac{1}{6} \int_0^1 (\sin\theta_e)\, \theta_2^3 x_1' ds, \\ u_{10} = -\tfrac{1}{2} \int_0^1 (\cos\theta_e)\, \theta_2^2 x_1' ds, \quad u_{11} = -\int_0^1 (\sin\theta_e)\, \theta_2 x_1' ds, \end{gathered} \tag{1.97}$$

are found using numerical integration (and the numerical solutions for the equilibrium variables and linear mode shapes). Similarly, equation 1.95 may be multiplied by x_2', and the two equations are used to find

$$\begin{aligned} a_1 &= w_1 c_1^3 + w_2 c_1^2 c_2 + w_3 c_1^2 + w_4 c_1 c_2^2 + w_5 c_1 c_2 + w_6 c_1 + w_7 c_2^3 + w_8 c_2^2 + w_9 c_2, \\ a_2 &= z_1 c_1^3 + z_2 c_1^2 c_2 + z_3 c_1^2 + z_4 c_1 c_2^2 + z_5 c_1 c_2 + z_6 c_1 + z_7 c_2^3 + z_8 c_2^2 + z_9 c_2, \end{aligned} \tag{1.98}$$

where w_k and z_k are constants found using u_k and the corresponding constants found using multiplication by x_2'. Differentiating these two equations with respect to t gives expressions for $\dot{a}_1(t)$, $\ddot{a}_1(t)$, $\dot{a}_2(t)$, and $\ddot{a}_2(t)$ as functions of $c_j(t)$ and their time derivatives.

In a similar manner, the remaining equations (in equation 1.92) may be multiplied by the spatial function derivatives ($y_j^{'}$, $p_j^{'}$, and $q_j^{'}$) to find equations that give $b_j(t)$, $d_j(t)$, and $e_j(t)$ and their first and second time derivatives as functions of c_j and the first and second time derivatives of c_j. These functions may be used to find the constants in the polynomial functions, g_1 and g_2, where

$$\ddot{c}_1 = g_1(c_1, c_2, \dot{c}_1, \dot{c}_2, \ddot{c}_1, \ddot{c}_2), \quad \ddot{c}_2 = g_2(c_1, c_2, \dot{c}_1, \dot{c}_2, \ddot{c}_1, \ddot{c}_2). \tag{1.99}$$

For a given set of initial conditions $c_j(0)$ and $\dot{c}_j(0)$, these resulting equations may be numerically integrated in time, t.

As an example, this method may be used on the problem of the vibration of a cantilever with self-weight, $w = 0$. Using the initial conditions $c_1(0) = 1$ and $c_2(0) = \dot{c}_1(0) = \dot{c}_2(0) = 0$ and damping, $c = 0$, gives a sinusoidal time series with a cycle period that corresponds to the first linear natural frequency. This result confirms linear vibration for small amplitudes of motion with the expected vibration frequency (given in equation 1.30).

To find results for larger amplitudes, the initial deflection in the first mode may be changed by varying $c_1(0)$. The resulting initial lateral deflection may then be found by solving the equation $b_1 = f(c_1, c_2)$. The resulting frequency, Ω_{N1}, increases with initial deflection, as expected, but the beam arclength of the initial deflection configuration also increases with $c_1(0)$. The relationship between initial lateral tip deflection, $y(s = 1, t = 0)$ and the resulting arclength ratio of the beam to the initial length, L/L_o, is shown in Figure 1.17. Because the desired model is of an inextensible beam, this method is only valid for very small dynamic deflections, and so another method to model moderate-to-large deflections is needed.

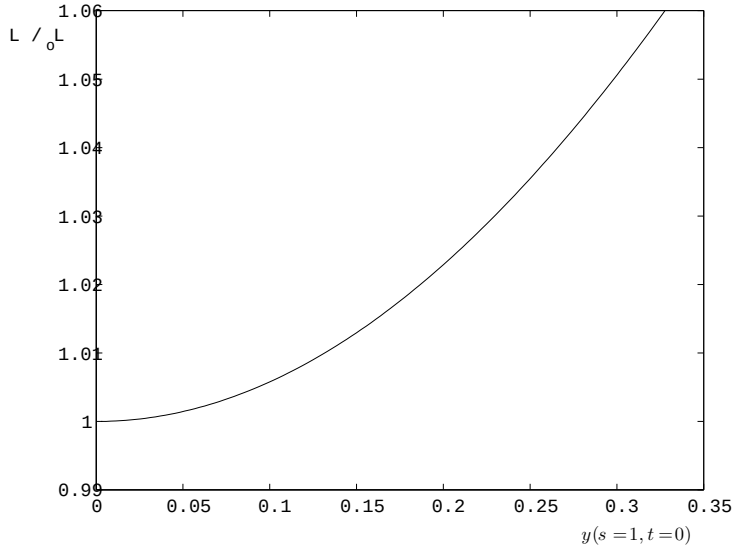

Figure 1.17: Initial deflected configuration arclength as a function of lateral, first-mode, tip deflection of a cantilever with $w = 0$ using the Galerkin method.

1.4.2 A Perturbation Method

The perturbation method makes use of a power series of functions as the assumed solution form. In addition, if the solution has components that occur at different time scales, the perturbation method of multiple scales may be used [25].

As an example, vibrations of the prebuckled, upright, heavy cantilever are analyzed. For the

dynamic elastica equations 1.35, the solution forms of the variables are assumed such that

$$\begin{aligned} x(s,t) &= x_e(s) + \sum_{j=1}^{n} \epsilon^j x_j(s, t_o, t_1, t_2), \\ y(s,t) &= y_e(s) + \sum_{j=1}^{n} \epsilon^j y_j(s, t_o, t_1, t_2), \\ \theta(s,t) &= \theta_e(s) + \sum_{j=1}^{n} \epsilon^j \theta_j(s, t_o, t_1, t_2), \\ p(s,t) &= p_e(s) + \sum_{j=1}^{n} \epsilon^j p_j(s, t_o, t_1, t_2), \\ q(s,t) &= q_e(s) + \sum_{j=1}^{n} \epsilon^j q_j(s, t_o, t_1, t_2), \end{aligned} \tag{1.100}$$

where ϵ is a small scalar parameter, $t_o = t$, $t_1 = \epsilon t$, $t_2 = \epsilon^2 t$, and, as before, the subscript e denotes equilbrium solutions. These equilibrium solutions, for the cantilever, are given in equation 1.64. The solution forms, along with the series approximations

$$\begin{aligned} \cos\left(\sum_{j=1}^{n} \epsilon^j \theta_j\right) &\approx 1 - \tfrac{1}{2}\left(\sum_{j=1}^{n} \epsilon^j \theta_j\right)^2 + \tfrac{1}{24}\left(\sum_{j=1}^{n} \epsilon^j \theta_j\right)^4, \\ \sin\left(\sum_{j=1}^{n} \epsilon^j \theta_j\right) &\approx \sum_{j=1}^{n} \epsilon^j \theta_j - \frac{1}{6}\left(\sum_{j=1}^{n} \epsilon^j \theta_j\right)^3 + \frac{1}{120}\left(\sum_{j=1}^{n} \epsilon^j \theta_j\right)^5, \end{aligned} \tag{1.101}$$

are substituted into equations 1.35. The derivatives with respect to time, written in terms of the three time scales, are given by [26]

$$\begin{aligned} \tfrac{\partial}{\partial t} &= \tfrac{\partial}{\partial t_o} + \epsilon \tfrac{\partial}{\partial t_1} + \epsilon^2 \tfrac{\partial}{\partial t_2}, \\ \tfrac{\partial^2}{\partial t^2} &= \tfrac{\partial^2}{\partial t_o^2} + 2\epsilon \tfrac{\partial}{\partial t_o}\tfrac{\partial}{\partial t_1} + \epsilon^2\left(\tfrac{\partial^2}{\partial t_1^2} + 2\tfrac{\partial}{\partial t_o}\tfrac{\partial}{\partial t_2}\right) + 2\epsilon^3 \tfrac{\partial}{\partial t_1}\tfrac{\partial}{\partial t_2} + \epsilon^4 \tfrac{\partial^2}{\partial t_2^2}. \end{aligned} \tag{1.102}$$

If damping is neglected ($c = 0$), the terms of order ϵ^1, when combined, give

$$\begin{aligned} x_1' = -\theta_1 \sin\theta_e = 0, \quad y_1' = \theta_1 \cos\theta_e = \theta_1, \quad p_1' = -\left(\partial^2 x_1/\partial t^2\right), \\ q_1' = -\left(\partial^2 y_1/\partial t^2\right), \quad \theta_1'' = (q_1 - p_e\theta_1)\cos\theta_e - (p_1 + q_e\theta_1)\sin\theta_e = q_1 - p_e\theta_1, \end{aligned} \tag{1.103}$$

where a prime denotes differentiation with respect to arclength, s. These equations are similar to the linear vibration equations 1.39 (where equations 1.64 have been applied for the equilibrium variables). This result is expected, because they correspond to amplitudes that are small enough

so that higher-order terms can be neglected. Applying the boundary conditions $x(s=0,t)=0$ and $p(s=1,t)=0$, the solutions

$$x_1(s,t,t_1,t_2)=0, \quad p_1(s,t,t_1,t_2)=0 \tag{1.104}$$

are determined. Equations 1.103 may be arranged to obtain

$$y_1^{''''}+w(1-s)y_1^{''}-wy_1^{'}+\left(\partial^2 y_1/\partial t^2\right)=0. \tag{1.105}$$

This equation is equivalent to equation 1.26, giving small-amplitude vibrations of the cantilever.

The solution is assumed here to take the form [26]

$$y_1(s,t,t_1,t_2)=A_n(t_1,t_2)\phi_n(s)e^{i\Omega_n t}+B_n(t_1,t_2)\phi_n(s)e^{-i\Omega_n t} \tag{1.106}$$

where n indicates the mode of vibration, ϕ_n is the n^{th} linear mode shape, and $B_n(t_1,t_2)$ is the complex conjugate of $A_n(t_1,t_2)$. The component $A_n(t_1,t_2)$ gives the effects of motion at slower time scales on the solution. The combined terms of order ϵ^2 give

$$\begin{gathered}
x_2'=-\tfrac{1}{2}\theta_1^2, \\
y_2'=\theta_2, \\
p_2^{'}=-\left(\partial^2 x_2/\partial t^2\right)-2\left(\partial^2 x_1/\partial t_1\partial t\right)=-\left(\partial^2 x_2/\partial t^2\right), \\
q_2^{'}=-\left(\partial^2 y_2/\partial t^2\right)-2\left(\partial^2 y_1/\partial t_1\partial t\right), \\
\theta_2^{''}=-p_e\theta_2-\tfrac{1}{2}q_e\theta_1^2-p_1\theta_1+q_2=-w(1-s)\theta_2+q_2.
\end{gathered} \tag{1.107}$$

These equations are combined, giving

$$y_2^{''''}+w(1-s)y_2^{''}-wy_2^{'}+\left(\partial y_2/\partial t^2\right)=-2\left(\partial^2 y_1/\partial t_1\partial t\right). \tag{1.108}$$

This equation is equivalent to the differential equation for y_1 (equation 1.105) with the exception of the right hand side "forcing" term. The homogeneous solution, then, of y_2 may take the same form as that of y_1 (given in equation 1.106). For bounded solutions, no terms of the form $e^{i\Omega_n t}$ may appear in the forcing term; these terms are called "secular" [25]. The term containing this exponential term is given by

$$i\Omega_n\phi_n\partial A_n/\partial t_1, \tag{1.109}$$

and, to be eliminated, gives $\partial A_n/\partial t_1=0$. This result implies that the solution given in equation 1.106 has no t_1-dependence. The solution may be rewritten

$$y_1(s,t,t_2)=A_n(t_2)\phi_n(s)e^{i\Omega_n t}+B_n(t_2)\phi_n(s)e^{-i\Omega_n t}. \tag{1.110}$$

The second time derivative (in equation 1.102) is now given by

$$\frac{\partial^2}{\partial t^2} = \frac{\partial^2}{\partial t_o^2} + 2\epsilon^2 \frac{\partial}{\partial t_o}\frac{\partial}{\partial t_2} + \epsilon^4 \frac{\partial^2}{\partial t_2^2}, \tag{1.111}$$

and the terms of order ϵ^3 give

$$\begin{aligned} x_3^{'} &= -\theta_1\theta_2, \\ y_3^{'} &= \theta_3 - \tfrac{1}{6}\theta_1^3, \\ p_3^{'} &= -\left(\partial^2 x_3/\partial t^2\right), \\ q_3^{'} &= -\left(\partial^2 y_3/\partial t^2\right) - 2\left(\partial^2 y_1/\partial t_2 \partial t\right), \\ \theta_3^{''} &= -p_e\theta_3 + \tfrac{1}{6}p_e\theta_1^3 - p_2\theta_1 - \tfrac{1}{2}q_1\theta_1^2 + q_3. \end{aligned} \tag{1.112}$$

These equations may again be used, along with equations 1.103 and 1.107 and the solutions

$$x_2 = \int -\tfrac{1}{2}y_1^{'2} ds, \quad p_2 = \int \left(-\partial^2 x_2/\partial t^2\right) ds + p_o, \quad q_1 = \int \left(-\partial^2 y_1/\partial t^2\right) ds + q_o \tag{1.113}$$

(where p_o and q_o satisfy $p_2(s=1,t) = q_1(s=1,t) = 0$), to generate a differential equation for y_3. The homogeneous part of this equation takes the same form as that of equation 1.105. To eliminate the secular terms, they are multiplied by ϕ_n, integrated from $s=0$ to $s=1$, and the result is set equal to zero, giving

$$2i\Omega_n \frac{dA_n}{dt_2}\int_0^1 \phi_n^2 ds + A_n^2 B_n \int_0^1 \phi_n \gamma_n ds = 0 \tag{1.114}$$

where

$$\begin{aligned} \gamma_n = {} & \tfrac{3}{2}\Omega_n^2 \phi_n \phi_n^{'2} + 3\Omega_n^2 q_o \phi_n^{'}\phi_n^{''} + 3\Omega_n^2 \phi_n^{'}\phi_n^{''}\textstyle\int_0^1 \phi_n ds + 3\phi_n^{''3} + 9\phi_n^{'}\phi_n^{''}\phi_n^{'''} \\ & + \tfrac{3}{2}\phi_n^{'2}\phi_n^{''''} - 2\Omega_n^2 \phi_n^{'}\textstyle\int_0^1 \phi_n^{'2} ds - 2\Omega_n^2 \phi_n^{''}\int_0^1\int_0^s \phi_n^{'2} ds ds - 2\Omega_n^2 p_o \phi_n^{''}. \end{aligned} \tag{1.115}$$

The form of $A_n(t_2)$ may be assumed such that [26]

$$A_n(t_2) = \frac{1}{2}a_n(t_2)e^{i\alpha_n(t_2)}, \tag{1.116}$$

where $a_n(t_2)$ and $\alpha_n(t_2)$ give the response amplitude and phase angle. Substituting this expression into equation 1.114 and separating the real and imaginary parts gives

$$\dot{a}_n \Omega_n e^{i\alpha_n(t_2)} \textstyle\int_0^1 \phi_n^2 ds = 0, \quad \dot{\alpha}_n = \tfrac{1}{8}a_n^2 \lambda_n \tag{1.117}$$

where

$$\lambda_n = \frac{\int_0^1 \phi_n \gamma_n ds}{\Omega_n \int_0^1 \phi_n^2 ds}, \tag{1.118}$$

and $\dot{a}_n = da_n/dt_2$ and $\dot{\alpha}_n = d\alpha_n/dt_2$. The value of λ_n for a given mode number may be found by numerical integration using the known linear natural frequency, Ω_n, mode shape, ϕ_n, and initial values, p_o and q_o. Because α_n is the phase angle of motion, the derivative $\dot{\alpha}_n$ gives the angular frequency. The response given in equation 1.106 can then be rewritten

$$y_1(s,t,t_2) = \frac{1}{2} a_n \phi_n(s) e^{i(\dot{\alpha}_n t_2 + \Omega_n t)} + \frac{1}{2} \bar{a}_n \phi_n(s) e^{-i(\dot{\alpha}_n t_2 + \Omega_n t)}, \tag{1.119}$$

where the coefficient of it in the exponent gives a nonlinear frequency estimate of

$$\Omega_N \approx \Omega_n + \frac{1}{8} a_n^2 \lambda_n. \tag{1.120}$$

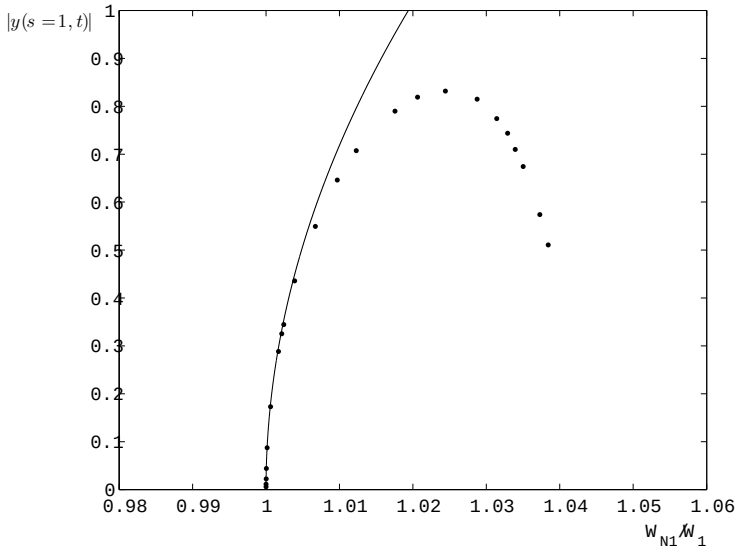

Figure 1.18: Backbone curves for a cantilever beam (with $w = 0$) using finite difference and perturbation methods, solid curve: perturbation method, data points: finite difference method.

The variation in frequency from the linear-vibration frequency is then given by the sign of λ_n. If $\lambda_n < 0$, the frequency decreases with the amplitude of motion (i.e., the response in mode n of the system is softening), and for $\lambda_n > 0$, the frequency increases (i.e., the response in mode n is hardening).

This perturbation method was used to find the heavy cantilever vibration results shown in Figure 1.8 where, for each self-weight value, $|y_1(s=1,t,t_2)| = a_1|\phi_1(1)|$ is plotted against Ω_{N1}/Ω_n. The backbone curves found using this method and the finite difference method (with $w = 0$) are shown in Figure 1.18 and are seen to agree closely up to a lateral dynamic deflection of about 40 percent of the beam length.

Equation 1.120 may be used to find backbone curves for higher vibration modes of the upright heavy cantilever. In addition, this equation and equation 1.115 may be used to find the variation in frequencies of vibration of an upright heavy beam with any boundary conditions if the vibrations are about the trivial equilibrium configuration. For these cases the corresponding linear mode shape $\phi(s)$ must be found and p_o and q_o must be chosen such that the boundary conditions are satisfied.

Clearly, the quadratic formula for the backbone curve (equation 1.120) is limiting. To find a more accurate solution, the series approximation shown in equations 1.101 may be expanded to include more terms or the terms of order ϵ^4 and ϵ^5 may be used to find a higher-order frequency-amplitude relationship. But because the method gives frequency, Ω_N, as a function of the magnitude of $A_n(t_2)$ (i.e., $\Omega_N = f(|A_n|)$), the method will only give results up to the maximum lateral deflection ($|y(s=1,t)| \approx 0.832$).

1.5 Experimental Methods

The theoretical frequency results in Figure 1.7 can be verified experimentally. A point-to-point laser vibrometer (*Ometron VH300+*) is used to measure the velocity at certain points along a system for small-amplitude vibration experiments. The system can be excited manually at different locations (and in different directions) or through forced excitation, using a shaker (*MB Dynamics PM50A Vibration Exciter*). For both cases, the resulting velocity data can then be interpreted using Brüel & Kjær's PULSE analyzer software. This software calculates the autospectrum $G_{xx}(k)$, defined as the average of the magnitude of the Fourier spectrum squared. Because the instrumentation collects velocity data at discrete time steps, a discrete Fourier transform is performed (given in equations 1.87 and 1.88).

A frequency span and increment can be specified, along with a windowing type. For the experiments herein, the Hanning window is used [11]. The resulting data can be analyzed and frequencies corresponding to autospectrum peaks are identified. In the case that the peak frequency is estimated to lie between two consecutive sampling frequencies, a weighted average method is again used (shown in equation 1.89).

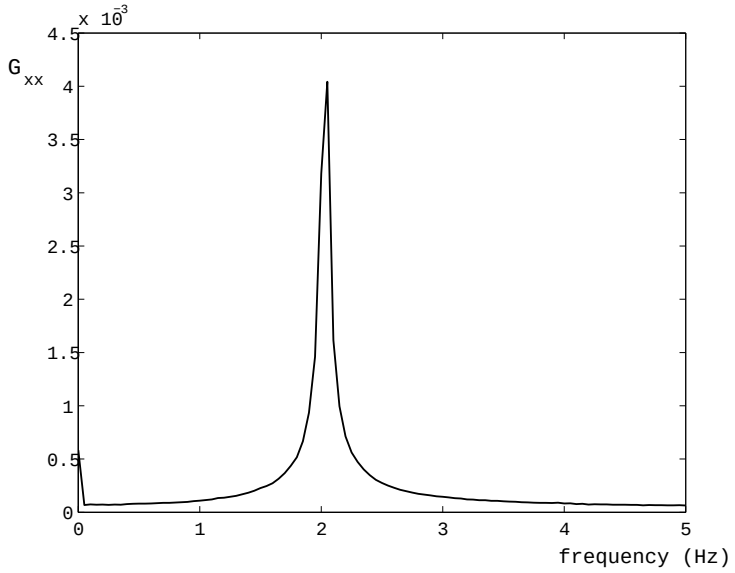

Figure 1.19: Autospectrum for the hanging cantilever with nondimensional weight $w = 4.534$. The weighted average peak frequency is 2.028 Hz, $\Omega = 4.542$.

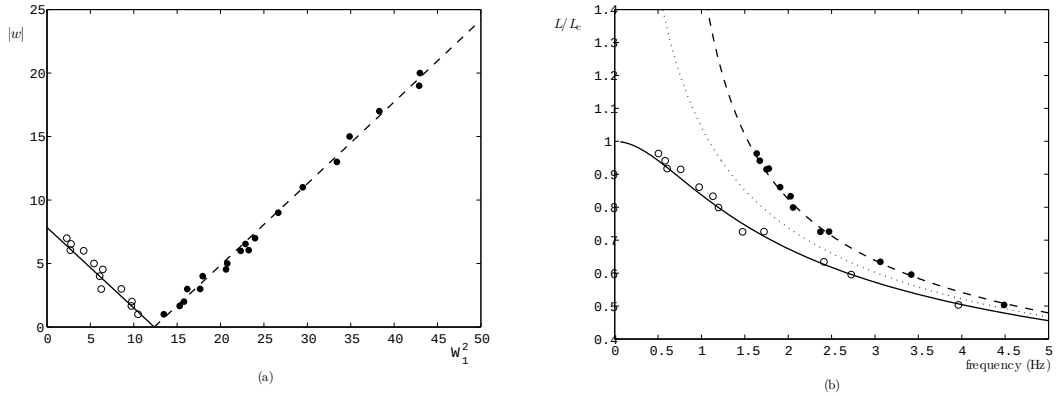

Figure 1.20: Experimental and theoretical results for the first frequency of the heavy, vertical cantilever, (a) nondimensional weight vs frequency squared, (b) dimensional plot of the same experimental and theoretical data. Open circles and solid curve: upright cantilever; closed circles and dashed curve: hanging cantilever; dotted line: frequencies found by neglecting self-weight using equations 1.30 and 1.10.

Thin polycarbonate strips are used in the experiments. The specific weight is 11.2 kN/m^3 and Young's modulus is 2.4 GPa. An autospectrum for the cantilever is shown in Figure 1.19 and experimental data for the upright and hanging cantilever are shown in Figure 1.20. In Figure 1.20(b), the data are plotted with dimensional values, where L/L_c is the beam length (normalized by the critical length) and the middle, dotted curve is found analytically using equations 1.30 and 1.10.

An experimental modal analysis can also be performed. Me'Scope VES (*Vibrant Technology, Inc.*) interprets incoming signals from the laser vibrometer, and a modal impact hammer (*Endevco 2302-50*) is used to excite the system in a specified direction and at several specified locations. Each resulting autospectrum is normalized with respect to the input force, and the software creates curve fits of each resulting frequency response function. Each point on the system can then be animated with the peak frequencies and calculated amplitudes.

1.6 Preliminary Work

The discussed numerical and experimental methods have been used to study some systems with both linear and nonlinear static configurations, along with the linear vibrations about those static configurations. Here, the analysis is used to characterize the effect of gravity on the linear vibrations of vertical cantilevers. In addition, the equilibria and linear vibrations of a clamped-clamped heavy beam and a highly deformed beam configuration are studied.

1.6.1 Mode-Splitting in the Heavy Vertical Cantilever

There are many examples of "mode-splitting" in the literature. This occurs when a symmetry in the system is broken, and is often due to a slight difference in geometry, e.g., a beam whose cross section is not quite square. In this study, this frequency detuning effect is caused by gravity (or by the beam orientation and the resulting effect of gravity on the system) [27].

The upright and hanging cantilevers are depicted in Figure 1.6, and, here, the effect of orientation on the dynamic behavior is studied. Assuming harmonic motion, the nondimensional governing equation of motion (for the prebuckled upright or hanging cantilever) is given in equation 1.28, where the variables have been nondimensionalized as shown in equation 1.25 and again damping (which is on the order of 0.5% in experiments) is neglected in the analysis. As before, the sign of the weight parameter, w, gives the beam orientation; for $w > 0$, the beam is upright, and for $w < 0$, the beam is in a hanging orientation. The case $w = 0$ corresponds to a short cantilever in a horizontal

orientation.

The upright and hanging systems have identical dynamic behavior if weight (and hence gravity) is ignored, resulting in the natural frequencies given in equation 1.30. In effect, this expression implies that the restoring force due to elastic bending is much greater than the restoring force due to gravity. The case corresponding to the other extreme (where the bending stiffness of the beam is negligible) results in the frequencies shown in equation 1.31 for the hanging orientation.

For experimental verification, a number of thin polycarbonate strips are fabricated such that frequencies for a range of the nondimensional parameter w can be examined. The base (where the beam is clamped) is attached to an electro-magnetic shaker and the system subject to a broadband, random excitation. A laser vibrometer can then be used to acquire velocity data from discrete locations along both beams, and subsequent signal processing used to obtain frequency response data. The cross-sectional dimensions of the strips are fixed at 25.4 mm $\times$ 0.508 mm. For example, a length of 0.166 m gives w values of +1, -1, and 0 for the upward, downward, and "horizontal" configurations, respectively. For the horizontal ($w = 0$) case the fundamental frequency was measured at 4.113 Hz, which compares to a value of 4.3 Hz obtained via equation 1.30.

If the same system is rotated 90 degrees in either direction (to create either the upright or hanging configuration), the frequency separation (mode splitting) is seen (as shown in Figure 1.21(a)). Now there are two adjacent peaks with dimensional fundamental frequencies of 3.962 Hz ($w = 1$, or upright) and 4.488 Hz ($w = -1$, or hanging). Figure 1.21(b) shows a similar result when $|w| = 4$ with an underlying dimensional horizontal frequency of 1.625 Hz, in which all the parameters are kept the same as in Figure 1.21(a) other than a length increase to 0.264 m.

Because the upright cantilever undergoes buckling when $w = 7.837$, the trivial equilibrium loses its stability at this self-weight value [3]. Thus, the results shown in Figure 1.21(a) (for which $w = 1$) correspond to a cantilever whose length is $(1/7.837)^{1/3} = 50\%$ of its buckling length, and 80% for the cantilever corresponding to the results shown in Figure 1.21(b).

Experiments are conducted for a range of different lengths, and hence, w-values, and the results are shown graphically (along with the numerical results shown in Figure 1.7) in Figure 1.22. For a given w, $\Delta\Omega$ gives the difference between the nondimensional frequencies of the hanging and upright configurations. Finally, the splitting of the fundamental frequencies as a function of w is shown in Figure 1.23(a), with the equivalent scaled results for the first four frequencies shown in part (b), where, for a given self-weight, w,

$$\frac{\Delta\Omega}{\Omega_c} = \frac{\Omega_{w<0} - \Omega_{w>0}}{\Omega_c}, \tag{1.121}$$

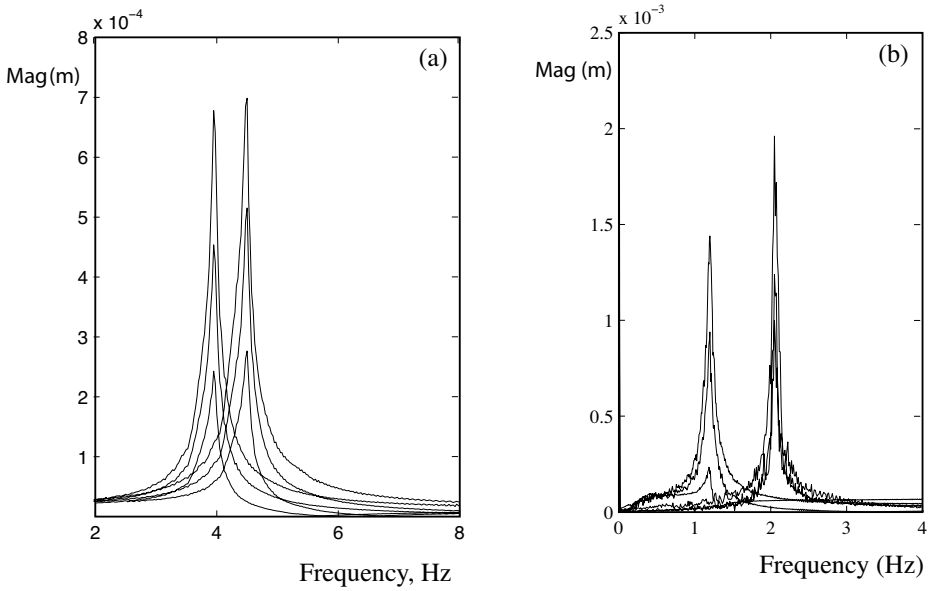

Figure 1.21: Experimental frequency response spectrum for a cantilever in a gravitational field, (a) $|w| = 1.0$, (b) $|w| = 4.0$. Data was acquired from six measurement points along the complete length.

and, for each mode, Ω_c is the natural frequency in that mode corresponding to $w = 0$.

The natural frequencies of very slender vertical cantilevers are affected by their orientation due to gravity. The important parameter is $w = \pm mgL^3/EI$ which reflects both the orientation (in terms of its sign) and the influence of bending versus gravity (in terms of its magnitude). If the orientation is purely vertical, then the equilibrium configuration is trivial, but the dynamic response is different according to whether the beam is held upright or suspended downwards. In the former case the frequencies are reduced due to the compressive nature of the self-weight loading (with the possibility of buckling). For the same beam, the latter case displays higher natural frequencies due to the stiffening effect of the beam weight, and as $w \to -\infty$ the system approaches the behavior of a hanging chain.

1.6.2 The Heavy Beam and Pinched Loop

A slender, straight beam resting on a flat, rigid foundation does not buckle when subjected to a compressive load, since the load cannot overcome the effect of the beam's weight. However, it buckles if its ends are moved toward each other. Postbuckling of such a beam is examined, both theoretically and experimentally, for horizontal and inclined foundations. The beam is modeled as an elastica, and equilibrium states with large deflections are computed, including cases in which

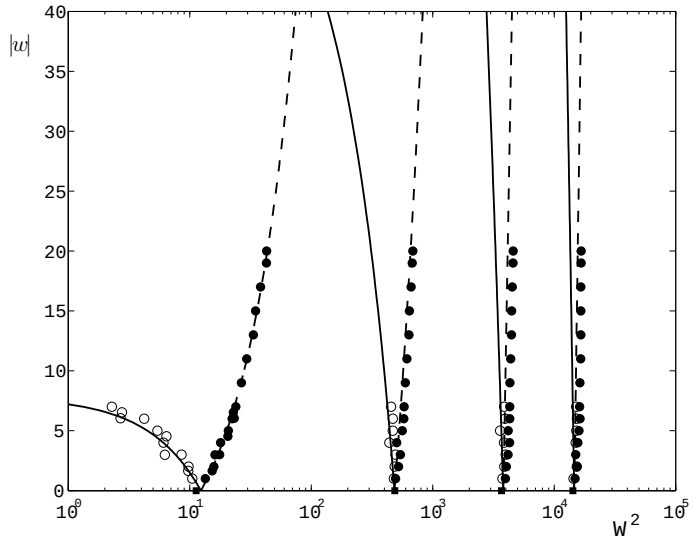

Figure 1.22: The four lowest linear vibration frequencies of the cantilever and their dependence on $|w|$: experiment and analysis, open circles and continuous curve: upright configuration, closed circles and dashed curve: hanging configuration, squares: $w = 0$, or experimental, horizontal configuration results.

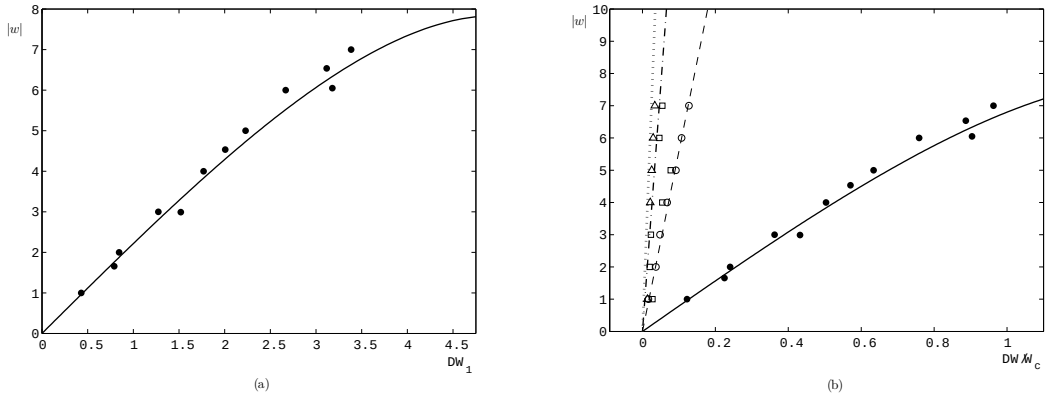

Figure 1.23: The split in the natural frequencies due to orientation as a function of $|w|$, experiment and analysis: (a) mode 1, (b) from left to right: modes 4, 3, 2, 1.

self-contact occurs. Frequencies and mode shapes for small vibrations about equilibrium are also determined. In addition, the case of self-contact is examined by clamping the two ends together to form a teardrop shape. The clamped end is held at various angles with the loop either upright, horizontal, downward, or halfway between these positions. The length of the loop is increased, and, again, the resulting equilibrium shapes, as well as small in-plane vibrations about equilibrium, are investigated analytically and experimentally.

The heavy beam may rest on a foundation that is horizontal or inclined. The inclined clamped-clamped heavy beam is depicted in Figure 1.24(a). The ends of the beam are moved toward each other (yielding an end-shortening, Δ).

In addition to the nondimensionalizations given in equations 1.25 and 1.34, the nondimensional end-shortening parameter, δ, is defined such that

$$\delta = \Delta / L. \tag{1.122}$$

The resulting equilibrium equations are given in equation 1.37. The shooting method is used to satisfy the boundary conditions $x_e(0) = y_e(0) = \theta_e(0) = y_e(1) = \theta_e(1) = 0$ and $x_e(1) = 1 - \delta$.

Some resulting static deflection shapes of the beam with $w = 125$ are shown in Figure 1.24(b), which also relates the vertical midpoint beam deflection (for the case of the initially horizontal beam) to the end-shortening. The dotted line and upper solid line correspond to the case of a rigid foundation lying beneath the beam, while the remaining curves and deflection shapes are some possible results for the case of no supporting foundation. The dashed and solid curves correspond to unstable and stable solutions, respectively.

For $w = 0$, the beam buckles at $p_o = 39.478 \approx 4\pi^2$, the well-established nondimensional critical buckling load for a clamped-clamped beam [1]. An analysis was also performed for several values of weight, $w > 0$. With $\beta = 0$, and in the presence of a horizontal foundation, the ends of the strip are moved together and:

- the strip initially has some finite length lying flat against the foundation (the strip is called "long" for this case and corresponds to the dotted line in Figure 1.24(b) [15]),
- if the weight is not too large, the strip becomes "short" (the strip does not touch the foundation between its ends) for some end-shortening value [15],
- for small weights, two sides of the strip contact each other, forming a bulb shape, at some end-shortening value,

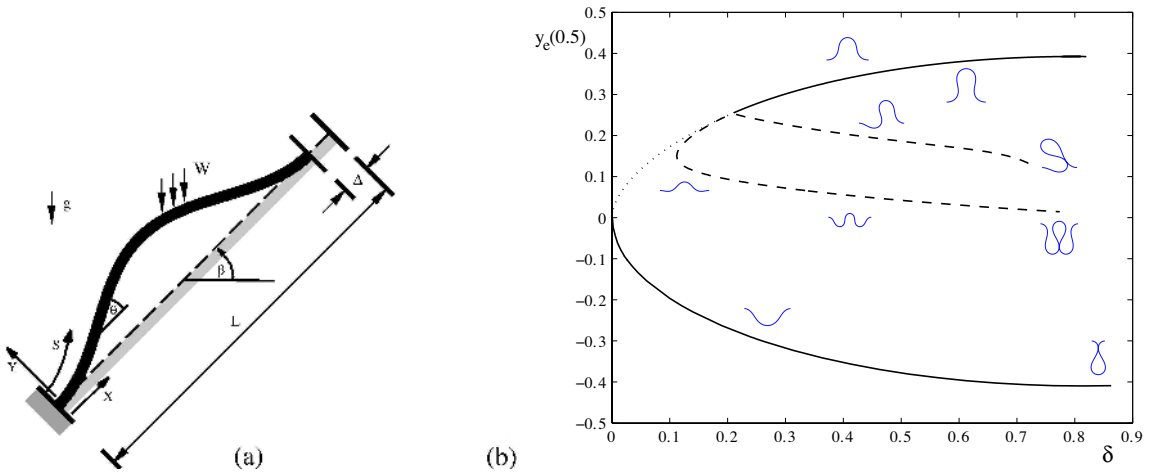

Figure 1.24: (a) Schematic of heavy inclined strip. (b) Midpoint deflection of the horizontal strip as a function of end-shortening, and corresponding equilibrium shapes for $w = 125$ and $\beta = 0$.

- for large weight values, the buckled segment tilts at a certain value of end-shortening, then self-contact occurs, and then the segment continues tilting until it contacts the foundation [28],
- for very large w-values, the strip is always long, up to self-contact.

For inclination angles, $0 < \beta < \pi/2$,

- as the higher end is initially moved downward toward the lower end, a flat segment exists adjacent to the higher end but not the lower end, and the strip is termed "short-long",
- self-contact occurs for some end-shortening value.

For $\beta = \pi/2$, the strip is vertical and corresponds to the case of the heavy column with fixed ends. The strip is always short and the foundation is irrelevant.

To isolate the case of clamped heavy beam self-contact, the ends of a straight, thin, uniform, flexible strip are bent until they meet, and are clamped together [29]. The strip then forms a teardrop shape, as shown in Figure 1.25(a), and is called a pinched loop. To put the analysis in nondimensional terms without involving the length L (since this is a convenient parameter to vary in experiments), the nondimensional parameters are defined such that

$$\begin{gathered} a = (EI/W)^{1/3}, \quad l = L/a, \quad x = X/a, \quad y = Y/a, \\ s = S/a, \quad p = Pa^2/EI, \quad q = Qa^2/EI, \quad m = Ma/EI, \end{gathered} \tag{1.123}$$

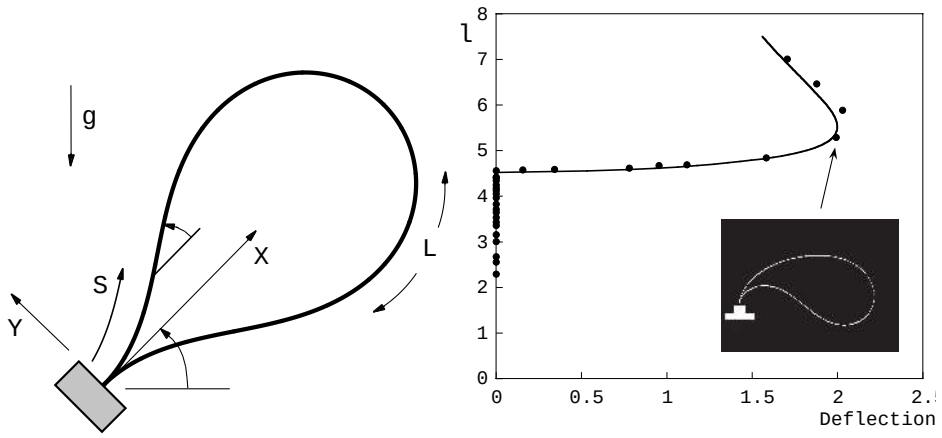

Figure 1.25: (a) Geometry of pinched loop; (b) Horizontal midpoint deflection of upright loop as a function of length. Continuous line, analytical; •, experimental.

This nondimensionalization is then valid for any nonzero weight per unit length, W. The resulting equilibrium elastica equations are

$$\begin{array}{ll} \partial x_e/\partial s = \cos\theta_e, & \partial y_e/\partial s = \sin\theta_e, \\ \partial\theta_e/\partial s = m_e, & \partial m_e/\partial s = q_e\cos\theta_e - p_e\sin\theta_e, \\ \partial p_e/\partial s = -\sin\beta, & \partial q_e/\partial s = -\cos\beta. \end{array} \tag{1.124}$$

The weight per unit length of the loop does not appear explicitly in these equations, and the nondimensional length, l, of the loop and orientation angle, β, are varied. The equations are numerically integrated along $0 \le s \le l$ using the shooting method to satisfy the boundary conditions $x_e(0) = y_e(0) = \theta_e(0) = x_e(l) = y_e(l) = 0$ and $\theta_e(l) = -\pi$.

As the length, l, is increased:

- in-plane buckling occurs at a critical length, $l = 4.5$, for the upright loop ($\beta = \pi/2$), and a supercritical pitchfork bifurcation is observed (the horizontal midpoint deflection as a function of length, l, is shown in Figure 1.25(b)),
- for other orientations, except the hanging one ($\beta = -\pi/2$), deflections also become large as the length is increased, and no buckling occurs,
- for the hanging loop, the equilibrium configuration remains symmetric, and the shape becomes slightly thinner and longer.

A linear dynamic analysis can be used to determine stability of equilibrium states (as in Figure 1.24(b)) and to predict buckling [8]. The linear vibration elastica equations for the heavy beam

are given in equation 1.39. These equations are used to obtain natural frequencies and corresponding mode shapes of the system. A similar derivation and analysis can be performed for the pinched loop.

For the heavy, horizontal, clamped beam, the natural frequencies can be found for strips that are short. The fundamental frequency is zero when the strip becomes short, increases with end-shortening, then decreases up to self-contact. For the inclined strip, the frequency is zero at the long-short transition, and corresponding mode shapes can be found.

For the case of the upright pinched loop

- as the length of the loop is increased, the fundamental frequency decreases until it is zero at the critical length $l = 4.50$.
- as the length is increased further and the loop droops (postbuckling deformation), the fundamental frequency increases.

For other orientation angles ($-\pi/2 \leq \beta < \pi/2$)

- the fundamental frequency decreases continuously for increasing length,
- if angles very close to $\beta = \pi/2$ were considered and l were increased, the corresponding fundamental frequency would decrease until l approached 4.50 and then would increase (similarly to the typical behavior of a slightly imperfect system),
- the differences between the fundamental frequencies for the different orientation angles are small if the length of the loop is either sufficiently small or sufficiently large (i.e., the fundamental frequency becomes almost independent of the orientation).

The first four mode shapes for the upright loop (experimental and analytical) are shown in Figure 1.26. The first vibration mode corresponds to a horizontal rocking about the equilibrium configuration, essentially pivoting about the clamped end. The second and fourth mode shapes are symmetric with respect to the vertical.

These linear and nonlinear static analyses and linear vibrations studies are the foundation for further applications of the elastica equations to other problems, including the study of highly-deformed structures as vibration isolators, and the study of the nonlinear dynamics of flexible beams. In addition to these specific applications, the equation formulation and numerical, analytical, and experimental methods described here are useful for the analysis of a diverse set of structural behavior systems.

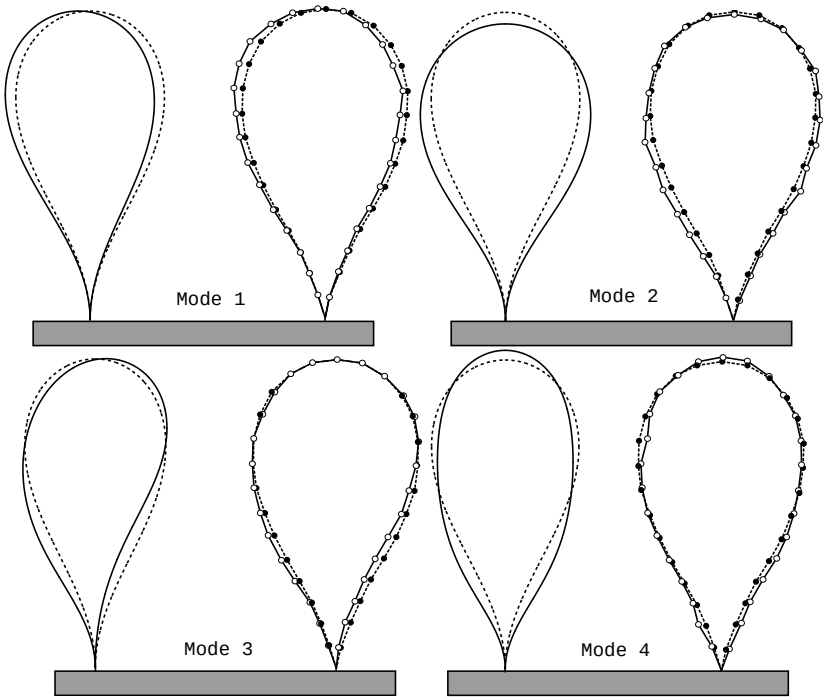

Figure 1.26: First four mode shapes for upright loop. Dashed curve, equilibrium (analytical); continuous curve, mode (analytical); •, equilibrium (experimental); ∘, mode (experimental).

Chapter 2

Vibration Isolation

2.1 Introduction and Background

There are many practical systems that require vibration isolation, where the reduction of vibration is desired in a system with a vibrating, or dynamically excited, component. A vibration isolator is placed between the vibration source and a mass to minimize the mass motion. For example, a control system that monitors the engine and other components of a car may be mounted in the vehicle, but vibrations may damage or shorten the lifespan of the system [11]. The control system must then be attached to the automobile with a vibration isolator. Minimization of the motion transmitted to the vehicle passengers is also desirable and can be accomplished with isolators. Equipment mounted in spacecraft and aircraft may also require protection from the unavoidable vibrations that the vessels undergo when in use [30]. Isolators may be made of "highly-damped materials" that change the system stiffness, including rubber, cork, or springs that are placed at one or more locations on the system [11].

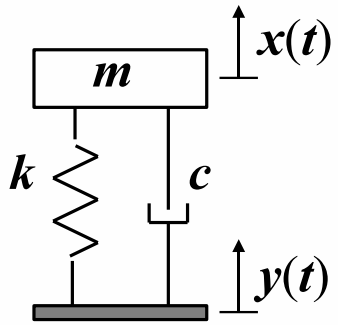

Figure 2.1: Spring-mass-damper system with base excitation, $y(t)$.

A simple isolator often may be modeled by a spring-mass-damper system with base excitation, as shown in Figure 2.1. The system consists of a spring with stiffness, k, that supports a mass, m, and a small amount of linear viscous damping is assumed. The mass displacement is $x(t)$ and the

base excitation is $y(t)$. The equation of motion, found by balancing forces, is given by

$$m\ddot{x} + c(\dot{x} - \dot{y}) + k(x - y) = 0, \tag{2.1}$$

If the base excitation, $y(t)$, is sinusoidal, such that $y(t) = A\sin\omega t$, the equation may be rearranged to give

$$m\ddot{x} + c\dot{x} + kx = cA\omega\cos\omega t + kA\sin\omega t. \tag{2.2}$$

The particular solution, $x_p(t)$, is found by solving for the constants, C_1 and C_2, where

$$x(t) = C_1\cos\omega t + C_2\sin\omega t, \tag{2.3}$$

that satisfy the differential equation. The ratio of the magnitude of the particular solution to the base excitation (or input) magnitude, A, is then the "displacement transmissibility," and this ratio is the value to be minimized in vibration isolation. In this case, the transmissibility is given by

$$Tr = \frac{|x_p(t)|}{A} = \sqrt{\frac{1 + (2\zeta\omega/\omega_n)^2}{\left[1 - (\omega/\omega_n)^2\right]^2 + (2\zeta\omega/\omega_n)^2}}, \tag{2.4}$$

where the damping ratio is $\zeta = c/2m\omega_n$ and the natural frequency is $\omega_n = \sqrt{k/m}$, found by setting $A = 0$ and finding the homogeneous solution, $x_h(t)$. It is clear by examining equation 2.4 that for small damping coefficient (or ζ) values, the transmissibility is largest for forcing frequencies, ω, near the natural frequency, ω_n. This transmissibility is plotted in Figure 2.2, as a function of the forcing frequency ratio, ω/ω_n, for various damping ratios. The magnitude of mass motion is equal to the forcing magnitude (or the transmissibility, $|x(t)|/A = 1$) for $\omega/\omega_n = 0$ and $\sqrt{2}$, regardless of the damping ratio. For forcing frequencies between these values, the transmissibility is always greater than unity; the transmitted motion is greater than the forcing amplitude, and the mass motion is amplified. For damping ratios $\omega/\omega_n > \sqrt{2}$, the transmissibility is less than one, and isolation occurs. Because the desired transmissibility occurs for forcing frequencies that are greater than the natural frequency of the system, generally an isolator with a small fundamental frequency is desired for effective isolation [31].

An effective isolator, then, can be created with a linear spring that has a small stiffness, k. But for the system depicted in Figure 2.1, the stiffness has an effect on both the natural frequency and the static deflection of the mass. The stiffness of a linear spring is the proportionality constant relating the displacement, x, to the applied force, F, or $F = kx$ (i.e., the force-deflection curve is linear). The static displacement that occurs by placing the mass on the spring is then x_o, where

$$mg = kx_o. \tag{2.5}$$

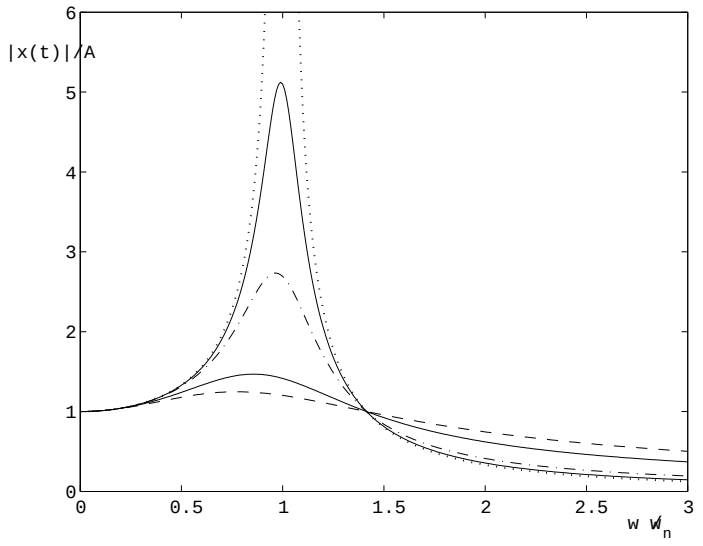

Figure 2.2: Transmissibility plot for a linear spring-mass-damper system for damping ratios $\zeta = 10^{-6}$ (uppermost curve), 0.1, 0.2, 0.5, 0.75.

Because the natural frequency of the system is $\omega_n = \sqrt{k/m}$, it can be given in terms of the static displacement (using equation 2.5) by

$$\omega_n = \sqrt{\frac{g}{x_o}}. \tag{2.6}$$

Because the static deflection, x_o, and natural frequency, ω_n, are related by equation 2.6, a decrease in one causes an increase in the other, making evident the limitations of this linear spring isolator. An ideal isolator, then, has a stiffness, k, that is not constant, giving a force-deflection curve that is nonlinear [32]. An example is illustrated in Figure 2.3. The static deflection is small (meaning that, for a range of force values, $F < mg$, the stiffness, or force-deflection curve slope, is large), and the local stiffness (or slope) is small (as in Figure 2.3(c)).

The use of some nonlinear structures as vibration isolators has been studied in the literature. Ellison, Ahmadi, and Kehoe [30] investigated the use of circular steel rings to isolate both horizontal and vertical motion. Vibrations were studied analytically and experimentally. Plaut, Alloway, and Virgin [33] studied two rigid bars, hinged to one another (where a rotational spring and damper are also located at the hinge) that act as a vertical isolator . Both linear and nonlinear responses were investigated and chaotic responses were found. Virgin and Davis [34] investigated the use of a pinned-pinned, postbuckled column isolator . Force-deflection curves were found experimentally

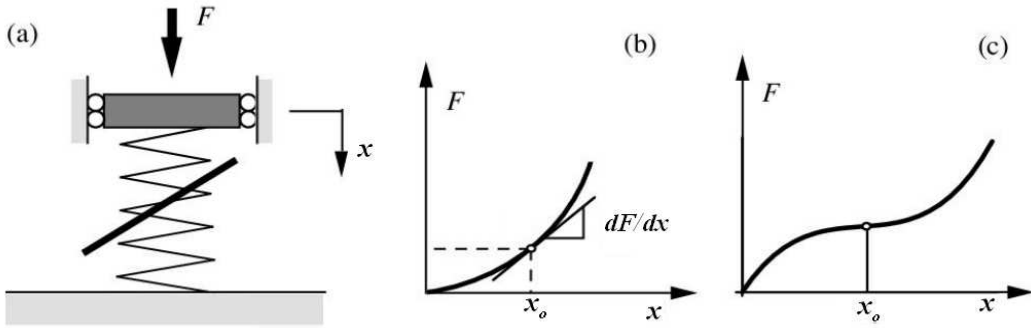

Figure 2.3: Example of a nonlinear spring with varying stiffness, $k = dF/dx$.

and analytically, and the transmissibility beyond resonance (as a function of ω/ω_n) was found using experimental data. Bonello [35] studied a pinned-pinned beam isolator, where the nonlinear stiffness of the beam was exploited by creating an adaptive system that changes the beam curvature (and hence the stiffness).

Vertical isolators comprised of buckled clamped-clamped beams were introduced and investigated by Winterflood et al [36–38]. Analysis of these isolators using the elastica equations was also performed [31, 39, 40], where the case of pre-bent columns was also studied (the columns are deflected in the first buckling mode before undergoing static mass loading).

Here, the use of a clamped-clamped beam as a vertical or horizontal motion isolator is studied. Numerical methods are used to confirm the system transmissibility for various parameter values. In addition, another isolator in the form of a highly-deformed structure is investigated. This structure gives a considerable range of stiffness control; system parameters may easily be adjusted to reach the desired natural frequency, and so a system with a frequency range of effective isolation may be created. The elastica equations are used to model the system, and experimental results are compared with the numerical analysis.

2.2 Buckled Strut Isolator

2.2.1 Vertical System

The vertical isolator system is shown in Figure 2.4. The experimental system is comprised of four buckled polycarbonate struts with the upper ends attached to a plate (or plates) having mass, M. The mass motion is given by $X(S = L, T)$, and the lower end of each strut is attached to a shaker that provides a vertical base excitation, $U(T)$. The motion of the mass is constrained (as shown in

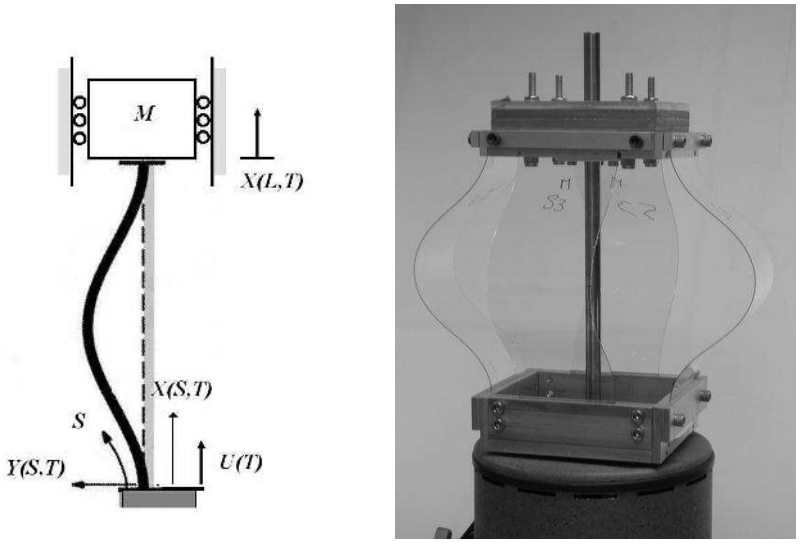

Figure 2.4: Shematic diagram and experimental configuration of buckled strut(s) used as a spring with base excitation, $U(T)$.

the schematic) such that it is purely vertical. This constraint is enforced in the experimental system by placing a rod through the center of the mass.

The nonlinear elastica equations (given in equations 1.35) may be used to investigate this isolator system's behavior, where the nondimensional parameters are given by equations 1.25, 1.34, and 1.122. The end-shortening, $\delta = \Delta/L$, resulting from the static mass load, M, is the static deflection (x_o, in the previous section). The nondimensionalized mass load is given by

$$f = MgL^2/EI. \tag{2.7}$$

It is important to note that, if more than one strut is used in the isolator system (as in the experimental system shown in Figure 2.4), the mass load, f, gives the applied force per column, so that

$$f_{total} = nf, \tag{2.8}$$

where n is the number of struts in the system, and each strut in the system deflects identically (in equilibrium and dynamic behavior). The length and stiffness, then, in equation 2.7 are those of a single strut. Under this assumption, it is sufficient to study the static and dynamic deflection of only one strut in the analysis. The boundary conditions to be satisfied are given by [31]

$$x(0,t) = u(t), \quad y(0,t) = y(1,t) = \theta(0,t) = \theta(1,t) = 0, \quad p(1,t) = f + f\frac{\partial^2 x(1,t)}{\partial t^2}, \tag{2.9}$$

where the final equation is found by summing the forces at $s = 1$. The equilibrium solution for the strut may be found by numerically integrating equation 1.37. The shooting method is used, with $\beta = \pi/2$, to satisfy the boundary conditions $x_e(0) = y_e(0) = \theta_e(0) = y_e(1) = \theta_e(1) = 0$ and $p_e(1) = f$ for varying self-weight values, w. The resulting force-deflection curves are plotted in Figure 2.5 for $w = 0$, 5, 10, and 25, along with some static configuration plots for varying f-values and $w = 0$. The advantage of using this structure as an isolator is evident: a large axial load results in a small static deflection and the initial postbuckling force-deflection slope (or stiffness) is also small.

Some system disadvantages can also be seen, however, by examining the force-deflection plot. For a fixed w-value, an increase in the mass load (or in the nondimensional load, f) results in a stiffness increase. Clearly this increase results from a change in the dimensional mass value, M, and so such a change increases both terms (the stiffness, k, and the mass, M) in the approximation of linear vibrations about the static equilibrium (given by $\omega = \sqrt{k/M}$ where k is the slope of the dimensional force-deflection curve). A different isolator system that allows a change in stiffness without a consequential change in the mass load may be preferable for this reason. There is also a system limitation on the mass load; the struts in the system must be buckled and, because the mass load is used to cause buckling, there is a minimum mass load, f, (for given w and n values) that may be isolated using this vertical system. To avoid self-contact, however, there is also a maximum mass load that may be isolated.

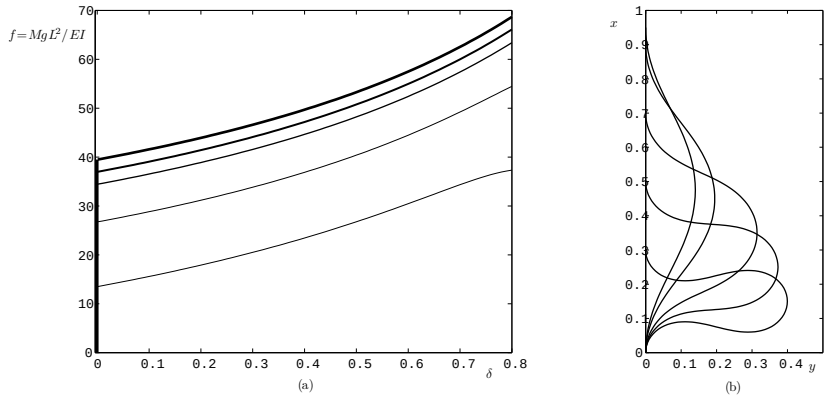

Figure 2.5: (a) Force-deflection curves for $w = 0$ (uppermost curve), 5, 10, 25, 50. (b) Vertical clamped-clamped beam isolator static configurations for $f = 40.5$, 41.6, 46.6, 53.3, and 62.5, with $w = 0$.

Experimental force-deflection data are shown in Figure 2.6 along with numerical results. The

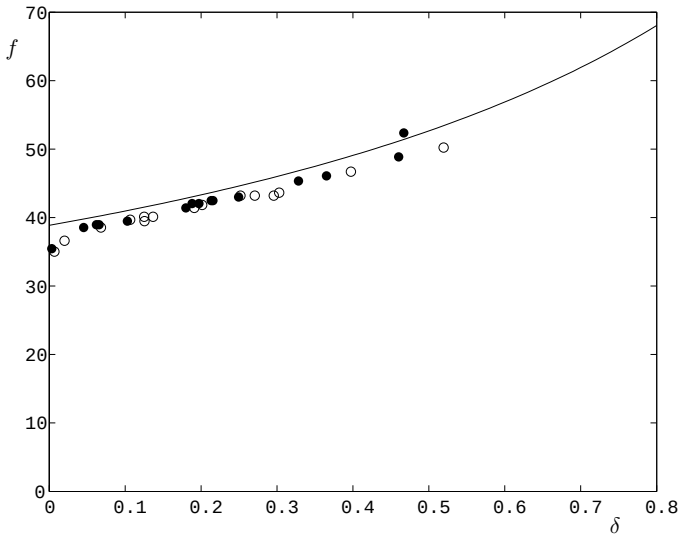

Figure 2.6: Force-deflection curve for vertical isolator: experiment and analysis, with $w = 1.23$ and $p_c = 38.86$. Continuous curve: numerical results, data points: experimental data (closed circles: outward deflection, open circles: inward deflection).

strut has a cross-sectional area of $0.787mm \times 76.2$ mm and length, $L = 0.2334$ m, resulting in $w = 1.23$. The nondimensional critical buckling load for this w-value is $p_c = 38.86$. The closed circles and open circles indicate opposite buckling directions. The data points for small static deflection values and their variation from the numerical data show that the strut is geometrically imperfect.

Equations 1.39 are used to find free vibration results for the system, using the boundary conditions $x_d(0) = y_d(0) = \theta_d(0) = y_d(0) = \theta_d(0) = 0$ and $p_1(1) = -f\Omega^2 x_1(1)$. In Figure 2.7, the fundamental system frequency is plotted as a function of mass load, f, for $w = 0$. If a change in the mass load value, f, affected only the dimensional mass term, M, in the linear natural frequency expression ($\omega = \sqrt{k/M}$), the relationship between the frequency and mass load would be given by $\Omega \propto 1/\sqrt{f}$ (i.e., the frequency would decrease with an increase in mass), but again, a change in the mass load also results in a stiffness change. Instead, the frequency of the curve increases for all values of f beyond the critical buckling load, $f_c = 4\pi^2$, where the slope of the curve is large for mass loads near f_c. The first three mode shapes are shown in Figure 2.8 for $f = 40$ and $w = 0$, and the dashed curve and open circle give the equilibrium configuration (and position of the mass). The solid curves and closed circles represent the mode shapes. These mode shapes correspond to

natural frequencies $\Omega_1 = 0.698$, $\Omega_2 = 44.73$, and $\Omega_3 = 75.26$.

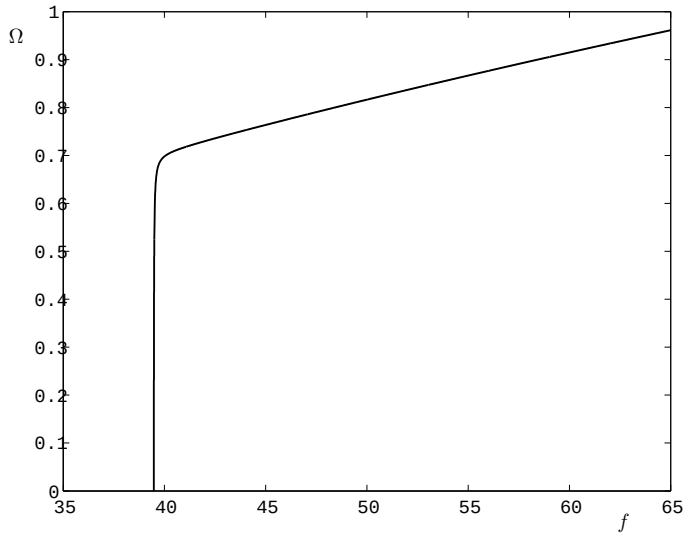

Figure 2.7: Nondimensional frequency, Ω, as a function of nondimensional mass load, f, for the vertical clamped-clamped beam isolator with $w = 0$.

In equations 1.36 and 1.39, damping is neglected ($c = 0$). Here, damping is a parameter of interest and significantly affects system dynamics. Linear vibrations may still be assumed in this analysis, because small-amplitude vibrations at forcing frequencies beyond resonance are of interest. An appropriate solution form for the variables is then given by

$$\begin{array}{ll} x(s,t) = x_e(s) + x_a(s)\sin\Omega t + x_b(s)\cos\Omega t, & y(s,t) = y_e(s) + y_a(s)\sin\Omega t + y_b(s)\cos\Omega t, \\ \theta(s,t) = \theta_e(s) + \theta_a(s)\sin\Omega t + \theta_b(s)\cos\Omega t, & m(s,t) = m_e(s) + m_a(s)\sin\Omega t + m_b(s)\cos\Omega t, \\ p(s,t) = p_e(s) + p_a(s)\sin\Omega t + p_b(s)\cos\Omega t, & q(s,t) = q_e(s) + q_a(s)\sin\Omega t + q_b(s)\cos\Omega t, \end{array} \tag{2.10}$$

where the subscripts a and b denote the dynamic variable solutions. Expressing the forms in this way is equivalent to assuming, for each variable, $x(s,t) = x_e(s) + x_d(s)e^{i\Omega t}$ [40]. Substituting these equations into equations 1.35 and using equilibrium equations 1.37 gives the linear dynamics equations

$$\begin{array}{ll} x_a^{'} = -\theta_a \sin\theta_e, & x_b^{'} = -\theta_b \sin\theta_e, \\ y_a^{'} = \theta_a \cos\theta_e, & y_b^{'} = \theta_b \cos\theta_e, \\ \theta_a^{'} = m_a, & \theta_b^{'} = m_b, \\ m_a^{'} = (q_a - p_e\theta_a)\cos\theta_e - (p_a + q_e\theta_a)\sin\theta_e, & m_b^{'} = (q_b - p_e\theta_b)\cos\theta_e - (p_b + q_e\theta_b)\sin\theta_e, \\ p_a^{'} = \Omega^2 x_a + c\Omega x_b, & p_b^{'} = \Omega^2 x_b - c\Omega x_a, \\ q_a^{'} = \Omega^2 y_a + c\Omega y_b, & q_b^{'} = \Omega^2 y_b - c\Omega y_a. \end{array} \tag{2.11}$$

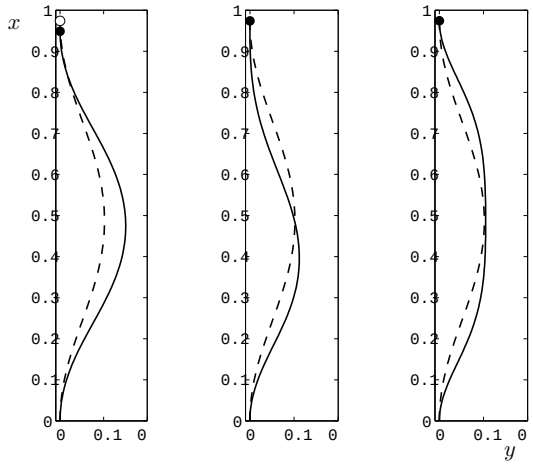

Figure 2.8: Vertical clamped-clamped beam mode shapes for $w = 0$, $\Omega_1 = 0.698$ (leftmost plot), $\Omega_2 = 44.26$, and $\Omega_3 = 75.28$. Dashed line and open circle: equilibrium configuration, solid line and closed circle: mode shape.

The form of base excitation, $u(t)$, is assumed to be sinusoidal and is given by

$$u(t) = u_o \sin \Omega t. \tag{2.12}$$

The nondimensional forcing amplitude, u_o, is defined as $u_o = U_o/L$, where U_o is the dimensional excitation amplitude. Using the converged equilibrium solution, equations 2.11 may be integrated numerically using the shooting method to satisfy the boundary conditions

$$\begin{gathered} x_a(0) = u_o, \\ x_b(0) = y_a(0) = y_b(0) = \theta_a(0) = \theta_b(0) = 0, \\ y_a(1) = y_b(1) = \theta_a(1) = \theta_b(1) = 0, \\ p_a(1) = -f\Omega^2 x_a(1), \quad p_b(1) = -f\Omega^2 x_b(1), \end{gathered} \tag{2.13}$$

for specified values of self-weight, w, and forcing amplitude and frequency, u_o and Ω.

The transmissibility for this system is given by

$$Tr = \frac{\sqrt{x_a(1)^2 + x_b(1)^2}}{u_o}, \tag{2.14}$$

which is equivalent to the ratio of the Fourier Transform (or autospectrum) magnitude of the mass motion to that of the base excitation. Numerical transmissibility results are shown in Figure 2.9 using the parameter values $w = 0$, $f = 40$, and $c = 1$ and 5. These results are in agreement with Plaut et al. [39]. As expected, the first three transmissibility peaks occur at forcing frequency values

$\Omega = 0.69$, 44.7, and 75.3 that are near the first three natural frequencies (given in Figure 2.8). It can be seen that forcing near the third natural frequency of the system gives a transmissibility just above unity for light damping ($c = 1$). A larger damping value results in effective isolation for forcing frequencies above the fundamental frequency. Typically, however, the amount of damping in a system is not easy to change.

For systems such as this one, where multiple transmissibility peaks are present (corresponding to the natural frequencies of the system), there may be a forcing frequency between consecutive peaks where the contributions by the natural frequencies to the steady-state vibration effectively cancel each other. At this forcing frequency, an "anti-resonance" is present, and can be seen in the tranmissibility plot in Figure 2.9 at $\Omega = 4.13$ and $\Omega = 103.81$ [41].

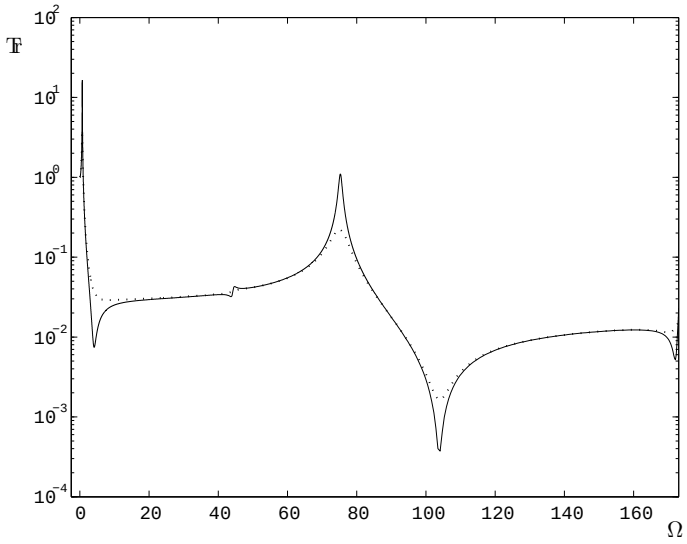

Figure 2.9: Transmissibility curve for vertical clamped-clamped beam isolator with $w = 0$, $f = 40$, and $c = 1$ (solid curve) and 5 (dotted curve).

Experimental transmissibility data may be found by fixing the forcing frequency and amplitude and measuring the response amplitude (or amplitude of mass motion). The frequency and amplitudes are recorded and the measurement is repeated for a range of forcing frequency values. A plate mass of $M = 2.537$ kg gives a nondimensional mass load per strut of $f = 50.25$ (where $n = 4$). The numerical analysis for the system with these parameter values (where $w = 1.23$, as above) gives an undamped natural frequency of 0.851 Hz. Resulting experimental transmissibility data are plotted in Figure 2.10, along with numerical results for varying nondimensional damping coefficient values,

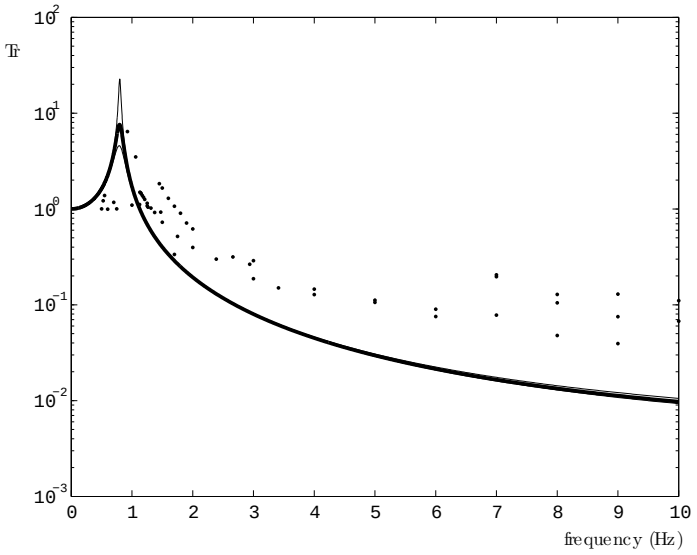

Figure 2.10: Experimental and numerical transmissibility curves for the vertical isolator system, $w = 1.23$, $f = 50.2534$. Dotted curves: $c = 5$ (upper curve), 25, solid curve: $c = 15$, data points: experimental data.

$c = 5$, 15, and 25. Experimental resonance occurs at 0.925 Hz. The nondimensional damping value that gives a peak frequency transmissibility value of the same order as the experimental results is $c = 15$ (giving a numerical damped natural frequency of 0.797 Hz).

The significant disagreement between the experimental and numerical data may be due to a number of factors. In the analysis, it is assumed that the struts are ideal (i.e., straight when there is no axial load) and each of the four struts behaves identically (i.e., each strut supports a quarter of the total mass load and deflects by the same end-shortening, δ). It can be seen in Figure 2.7 that a small change in the mass load for the initially postbuckled beam results in a significant change in the natural frequency. It is likely, for this reason, that even a slight difference in the initial imperfections of the struts causes a significant variation in their dynamic behavior, and coupling of the individual natural frequencies of the four struts may occur, altering the dynamic behavior of the system as a whole. This system asymmetry may also cause slight static or dynamic rotation of the mass plate, resulting in significant friction along the central rod.

The main disadvantages of this vertical isolator then are an inherent system asymmetry and a lack of stiffness control. Two other isolator systems that address these problems are investigated here.

2.2.2 Horizontal System

A horizontal clamped-clamped beam isolator is shown in Figure 2.11, where two beams (of length L_1 and L_2) are attached to either end of the mass to be isolated. A sinusoidal input excitation, $U(T) = U_o \sin \omega t$, acts in the horizontal direction at the left end of the left beam, and the right end of the right beam is fixed. The mass moves only in the horizontal direction. Because the system stiffness is determined by the static axial load (or end-shortening), it is independent of the mass load, f (defined as above in equation 2.7), and so this system has a level of stiffness control that is lacking in the previous, vertical isolator system.

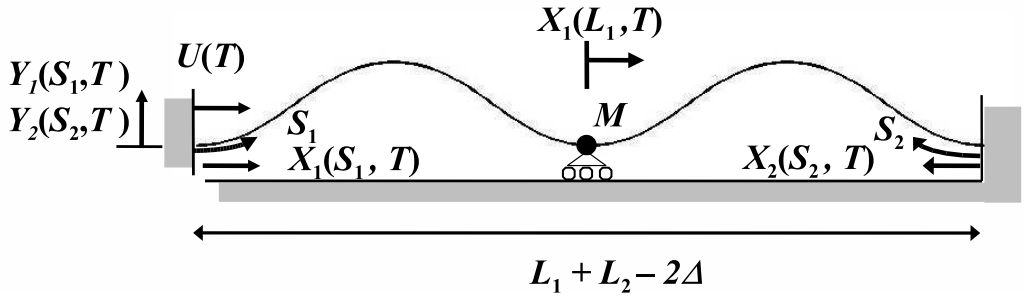

Figure 2.11: Horizontal isolator schematic.

The elastica equations (equations 1.35) may again be used to study this system, along with the same nondimensional variables and parameters as for the horizontal isolator. To numerically integrate the equations using the shooting method, it is convenient to use two arclength variables, where S_1 and S_2 represent the arclengths of the left and right struts, respectively, as shown in Figure 2.11. These arclength variables are nondimensionalized by the strut lengths (so that $s_1 = S_1/L_1$ and $s_2 = S_2/L_2$) and the boundary conditions are given by

$$\begin{gathered} x_1(0,t) = u(t), \\ y_1(0,t) = y_2(0,t) = \theta_1(0,t) = \theta_2(0,t) = 0, \\ y_1(1,t) = y_2(1,t) = \theta_1(1,t) = \theta_2(1,t) = 0, \\ x_1(1,t) + x_2(1,t) = 2 - 2\delta - u(t), \\ p_1(1,t) = p_2(1,t) + f\frac{\partial^2 x_1(1,t)}{\partial t^2}, \end{gathered} \tag{2.15}$$

where 2δ is the total end-shortening on the two struts. Assuming the struts are identical, the end-shortening of each strut is δ.

It is important to note that, unlike in the vertical system, even if the two struts are assumed to be identical (or have the same w-value), they must be analyzed simultaneously. The boundary

conditions for each are coupled and the assumption that they deflect dynamically in phase is no longer valid. In fact, it will be shown that system resonance occurs when the struts are out of phase with one another.

For a given end-shortening and w-value, the equilibrium equations (equations 1.37) may be solved (using $\beta = 0$) to satisfy

$$\begin{gathered} x_{ej}(0) = y_{ej}(0) = \theta_{ej}(0) = 0, \\ x_{e1}(1) + x_{e2}(1) = 2 - 2\delta, \quad y_{ej}(1) = \theta_{ej}(1) = 0, \end{gathered} \tag{2.16}$$

where $j = 1$ (for the left strut) or $j = 2$ (for the right strut).

Equations 1.39 are again used to find the fundamental frequency of the system, using the boundary conditions. In Figure 2.12, the fundamental frequency as a function of mass load, f, is shown for $w = 0$ (for both struts) and end-shortening values $\delta = 0.05$, 0.1, 0.25, 0.5, and 0.7. Unlike for the vertical isolator system, the frequency here is seen to decrease with an increase in the mass load. Because the stiffness is determined only by the end-shortening (which, for this system, is independent of the mass load) and self-weight of the struts, this horizontal system is useful for a much larger range of mass load values than the vertical isolator system. The mass load does not need to be above the critical buckling load and it also does not affect static self-contact (which is determined by the end-shortening).

The modes of vibration for this system are similar to those shown for the vertical case (in Figure 2.8); here, the left and right struts are exactly out of phase. For $\delta = 0.1$ and $f = 40$, the first three natural frequencies are $\Omega = 1.036$, 43.89, and 75.93.

To consider forced vibrations, damping is included, and the variables may be written in the form given in equations 2.10 and solved numerically. The dynamic variable boundary conditions are found using equations 2.15 and 2.16, resulting in

$$\begin{gathered} x_{a1}(0) = u_o, \\ x_{b1}(0) = x_{a2}(0) = x_{b2}(0) = y_{aj}(0) = y_{bj}(0) = \theta_{aj}(0) = \theta_{bj}(0) = 0, \\ x_{a1}(1) + x_{a2}(1) = 0, \quad x_{b1}(1) + x_{b2}(1) = 0, \\ y_{aj}(1) = y_{bj}(1) = \theta_{aj}(1) = \theta_{bj}(1) = 0, \\ p_{a1}(1) = p_{a2}(1) - f\Omega^2 x_{a1}(1), \quad p_{b1}(1) = p_{b2}(1) - f\Omega^2 x_{b1}(1). \end{gathered} \tag{2.17}$$

The system transmissibility may be found numerically by varying the forcing frequency. But if the excitation is constant, such that $u(t) = u_o$, and the two beams are identical, then the resulting mass deflection is given by $x_1(1,t) = u_o/2$ (using the boundary conditions given in equations 2.15).

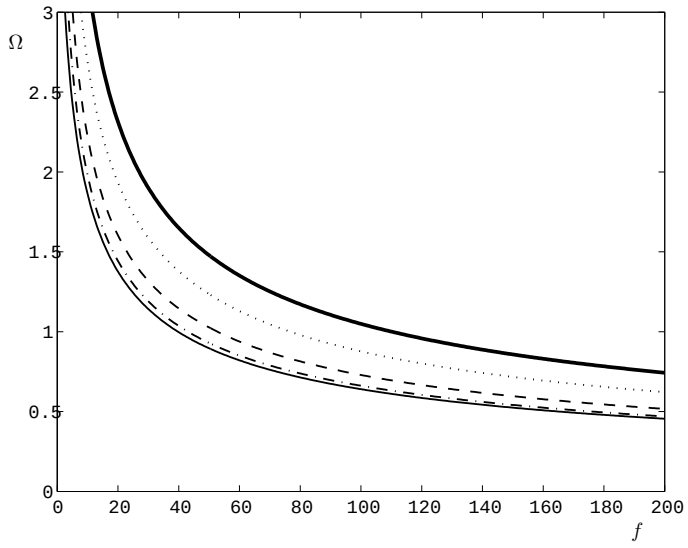

Figure 2.12: Nondimensional frequency, Ω, as a function of mass load, f, for the horizontal clamped-clamped beam isolator with $w = 0$ and $\delta = 0.05$ (lowermost curve), 0.1, 0.25, 0.5, and 0.7.

So effective isolation occurs for transmissibility values

$$Tr = \frac{\sqrt{x_{a1}(1)^2 + x_{b1}(1)^2}}{u_o} < \frac{1}{2}, \tag{2.18}$$

and the transmissibility for $\Omega = 0$ is Tr = 0.5. Numerical results for $w = 0$, $\delta = 0.1$, $f = 40$, and $c = 1$ are shown in Figure 2.13. As for the vertical isolator, the transmissibility peaks occur near the natural frequencies. The steady-state vibration shapes corresponding to the first three transmissibility peaks for this case are shown in Figure 2.14. The equilibrium configuration is plotted with the dashed curve (and the mass location at equilibrium is plotted with an open circle). For motion near the first transmissibility peak (the first plot in Figure 2.14), steady-state motion is similar to that of the first mode (where the struts are out of phase). However, unlike for the vertical isolator, the vibration shapes at the second and third transmissibility peaks are noticeably different from the second and third mode shapes. While each strut moves in the second and third modes, the amplitudes of motion of the left and right strut are significantly different. The left strut is seen to move with a much larger amplitude. Some motion is transmitted to the right strut, but because the amplitude of mass motion (and hence, excitation of the right strut) is much smaller than that of the actual excitation, $u(t)$, the amplitude of motion of the right strut is also smaller. This phenomenon is called "mode localization" and, in this and other cases, may be exploited for isolation [42]. Mode

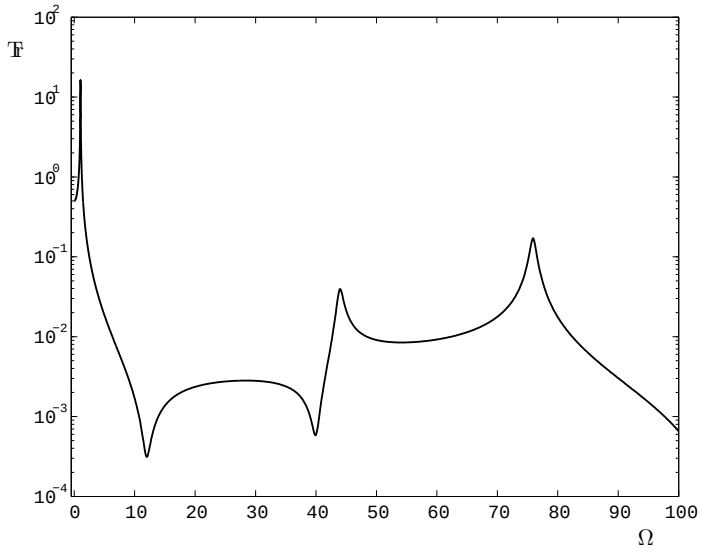

Figure 2.13: Transmissibility for the horizontal isolator system with $w = 0$, $f = 40$, $\delta = 0.1$, and $c = 1$.

localization in a similar multispan, coupled beam system was studied by Vakakis et al. [43], where vibration amplitude ratios of the various beams were found as a function of the torsional stiffeners connecting the beams. The advantage of this phenomenon in the application studied here is that, even at transmissibility peaks, effective isolation occurs, because the majority of the energy (or motion) is in the left strut. There are also two anti-resonances that occur between the first two transmissibility peaks. The vibration shapes corresponding to these frequencies ($\Omega = 12.01, 39.92$) are shown in Figure 2.15. Although this system permits a large range of mass load values, improves the level of stiffness control, and gives dynamic mode localization results that produce effective isolation, there are still some system disadvantages. Experimentally, a similar difficulty of system asymmetry arises for this isolator system as for the vertical system, especially since the axial motion of the left strut and right strut are coupled. A system with only one isolator structure eliminates coupling, and an example of such an isolator is presented next.

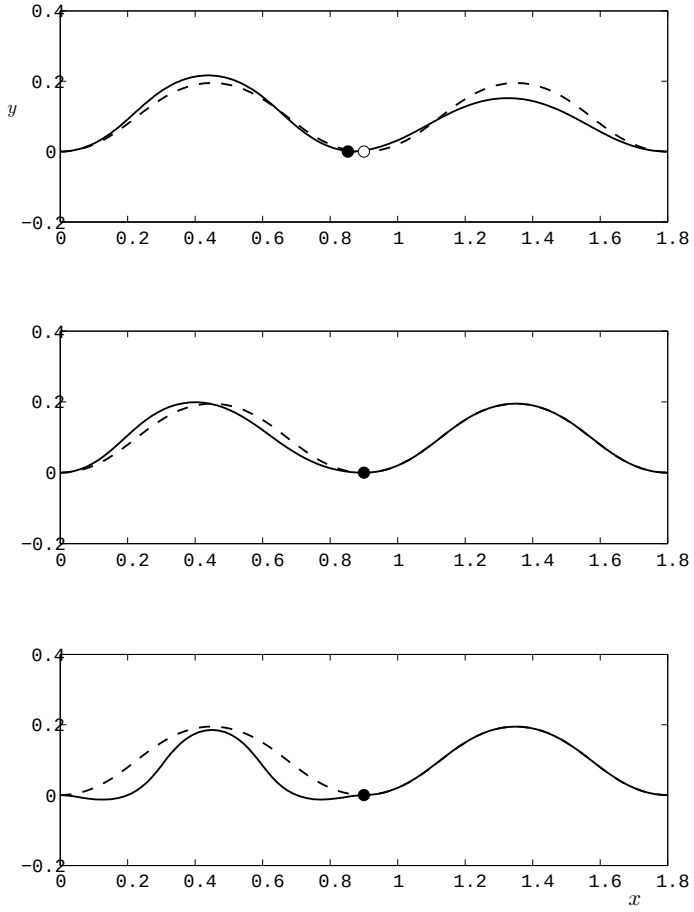

Figure 2.14: Steady-state vibration shapes for the horizontal isolator system at the first three transmissibility peaks with $w = 0$, $\delta = 0.1$, and $f = 40$. Dashed curve and open circle: equilibrium, continuous curves and closed circles: vibration shapes.

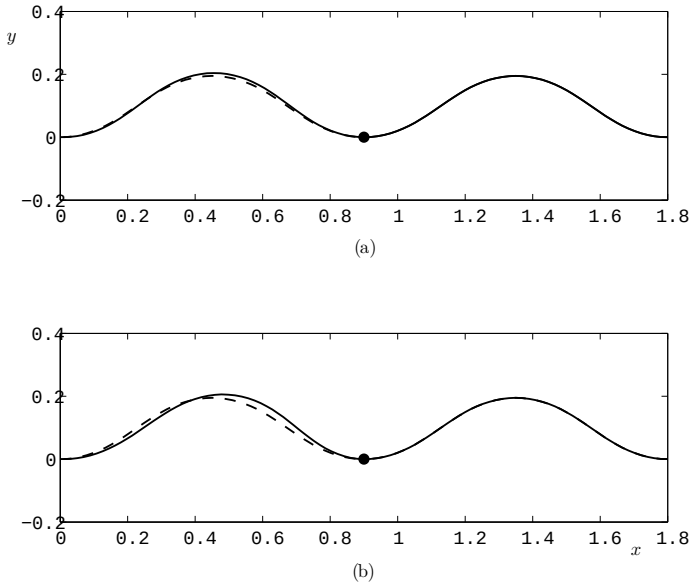

Figure 2.15: Steady-state vibration shapes for the horizontal isolator system at antiresonances, (a) $\Omega = 12.01$ and (b) 39.92, with $w = 0$, $\delta = 0.1$, and $f = 40$. Dashed curve: equilibrium, continuous curves: vibration shapes.

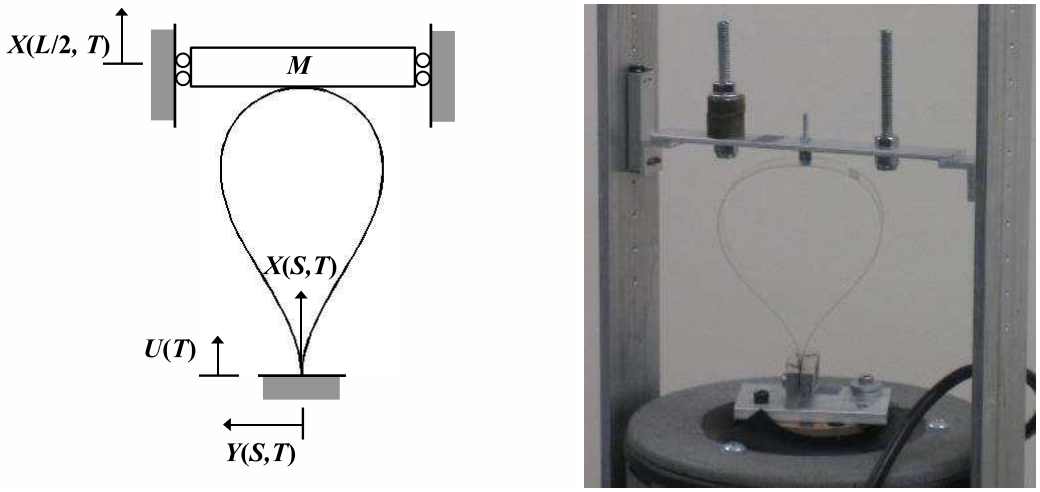

Figure 2.16: Pinched loop isolator schematic and experimental system.

2.3 Pinched Loop Isolator

2.3.1 Introduction and Analytical Formulation

The pinched loop isolator is shown in Figure 2.16. Excitation occurs at the base where the strip ends are clamped together and the mass is attached to the midpoint of the strip and allowed to move vertically. In the experimental system, the mass may be altered by adding or removing weights on the bar attached to the polycarbonate strip, and the mass is attached to a vertical crossed roller slide. The pinched loop was introduced in Section 1.6.2, and, in additon to the nondimensional variables given in equation 1.123, the nondimensional time and frequency parameters are defined such that [29]

$$t = T\sqrt{g/a}, \quad \Omega = \omega\sqrt{a/g}, \tag{2.19}$$

where ω is a dimensional vibration frequency. Again, this nondimensionalization is valid for any nonzero weight per unit length, $W > 0$. The nondimensional mass load is defined here as

$$f = Fa^2/EI, \tag{2.20}$$

where $F = Mg$. Because it is assumed to be applied as a vertical point load at $s = l/2$ and given the structural symmetry of the loop (with a constraint against horizontal motion at $s = l/2$), it is sufficient to numerically analyze only half of the strip, so that $0 \leq s \leq l/2$, where the point load at $s = l/2$ is $f/2$. The governing elastica equations using the defined nondimensional parameters are

$$\begin{array}{ll} \partial x/\partial s = \cos\theta, & \partial y/\partial s = \sin\theta, \\ \partial\theta/\partial s = m, & \partial m/\partial s = q\cos\theta - p\sin\theta, \\ \partial p/\partial s = -\sin\beta - \partial^2 x/\partial t^2, & \partial q/\partial s = -cos\beta - \partial^2 y/\partial t^2, \end{array} \tag{2.21}$$

where the corresponding equilibrium equations are given in equations 1.124. The boundary conditions are

$$\begin{array}{c} x(0,t) = u(t), \quad y(0,t) = \theta(0,t) = 0, \\ y(l/2,t) = 0, \quad \theta(l/2,t) = -\pi/2, \quad p(l/2,t) = f/2 + (f/2)\frac{\partial^2 x(l/2,t)}{\partial t^2}. \end{array} \tag{2.22}$$

2.3.2 Equilibrium

For the equilibrium solution, the nondimensional length, l, and mass load, f, are specified (and $\beta = \pi/2$), and numerical integration is performed along $0 \leq s \leq l/2$ to satisfy $x_e(0) = y_e(0) =$

$\theta_e(0) = y_e(l/2) = 0$, $\theta_e(l/2) = -\pi/2$, and $p_e(l/2) = f/2$. The vertical mass deflection (or vertical deflection of the loop at $s = l/2$) is called δ, where

$$\delta = x_e(l/2)|_{f=0} - x_e(l/2). \tag{2.23}$$

Again, this upright loop configuration loses stability [29], but here the arc length is kept below the critical value ($l = 4.50$). Some resulting equilibrium configurations for a nondimensional length, $l = 2$, are shown in Figure 2.17(a). The uppermost curve gives the static shape with no mass load ($f = 0$), and the remaining curves result from mass loads $f = 10$, 20, ..., 90, and 98.6. The final curve corresponding to $f = 98.6$ gives the static configuration just before self-contact. Force-deflection curves are plotted in Figure 2.17(b) for nondimensional lengths $l = 1.5$, 2, 2.5, and 3 for static deflections up to $\delta = 0.584$, 0.778, 0.972, and 1.164, respectively. Each curve is continued up to self-contact. As expected, an increase in loop length is seen to cause a decrease in the stiffness (or force-deflection curve slope), and the initial slope of the curve is large (indicating that the loop has a large initial stiffness - a desirable characteristic for a vibration isolator). It is evident that the mass load may be used to tailor the system stiffness (to give effective isolation).

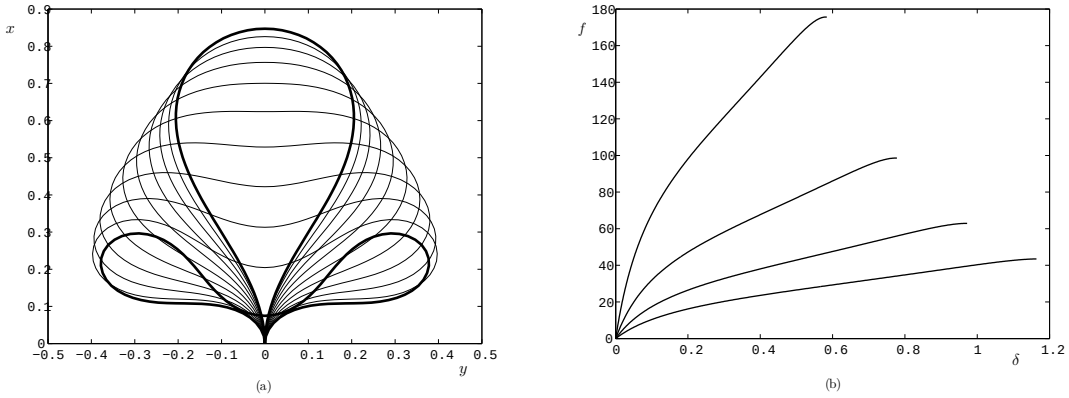

Figure 2.17: Numerical equilibrium results for the pinched loop isolator. (a) Static configurations for $l = 2$ and mass loads, $f = 0$, 10, 20, ..., 90, 98.6. (b) Force-deflection curves for nondimensional lengths, $l = 1.5$ (uppermost curve), 2, 2.5, 3.

Experimental equilibrium configuration results for $l = 1.7416$ (using a polycarbonate strip with cross-sectional area 25.4 mm $\times$ 0.508 mm, giving a nondimensional parameter value $a = 0.1664$) are shown in Figure 2.18, where upward loads ($f < 0$) are included. The continuous curve gives numerical results, and the experimental data points agree well with the theory.

The vertical stiffness, $k = df/d\delta$, may be found by estimating the slope of the static force-deflection curve, and these results are shown in Figure 2.19 as a function of loop length, l, for four

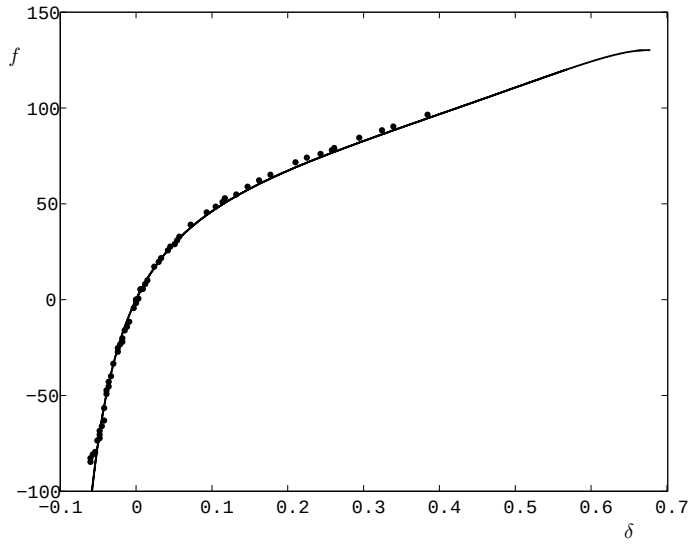

Figure 2.18: Force-deflection curve for the pinched loop isolator with $l = 1.7416$. Solid curve: numerical results, data points: experimental results.

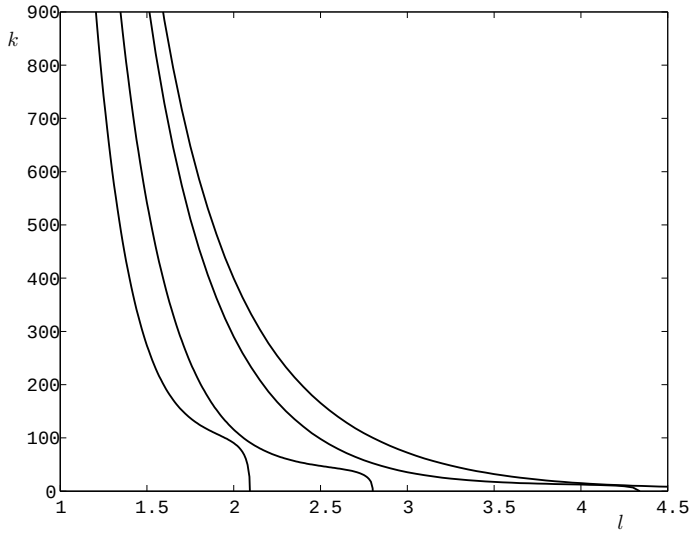

Figure 2.19: Vertical stiffness ($k = df/d\delta$) of the pinched loop isolator as a function of length, l, for mass loads (from left to right), $f = 90$, 50, 20, 10.

mass load values (from left to right), $f = 90$, 50, 20, and 10. The curve corresponding to each mass load is plotted until the stiffness drops to zero (corresponding to a horizontal tangency on the force-deflection curve and a loss of stability).

2.3.3 Free Vibration

Free vibration frequencies and mode shapes for the system are found using the equilibrium solution (for given values of l and f), equations 1.39, and the shooting method to satisfy $x_d(0) = y_d(0) = \theta_d(0) = y_d(l/2) = \theta_d(l/2) = 0$ and $p_d(l/2) = -(f/2)\Omega^2 x_d(l/2)$. The first frequency is plotted in Figure 2.20 for the four nondimensional lengths $l = 3$, 2.5, 2, and 1.5. For each length, frequencies are found up to self-contact, which, for $l = 3$ and 2, occurs before the system becomes unstable (i.e., before the frequency drops to zero). As with the horizontal clamped-clamped beam isolator, the frequency decreases with the mass load. Similarly to the vertical isolator, however, the mass load affects both the inertia at $s = l/2$ and the local stiffness of the system. One advantage of this system, when compared with the previous vertical isolator, is that no minimum mass load is required for isolation, as shown in Figure 2.20, where a frequency is found for each length at $f = 0$.

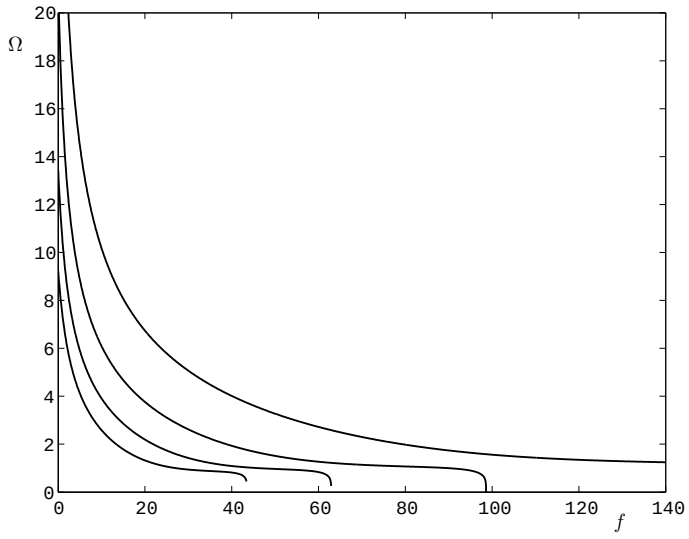

Figure 2.20: Frequency as a function of mass load for the pinched loop isolator, with (from left to right) $l = 3$, 2.5, 2, 1.5.

The first three natural frequencies as a function of mass load, f, are shown in Figure 2.21 for $l = 2$ (up to self-contact). With no mass load ($f = 0$), the natural frequencies for this case are

$\Omega_1 = 21.13$, $\Omega_2 = 59.59$, and $\Omega_3 = 120.56$. Each of the frequencies decreases initially, and the third frequency reaches a minimum at $f = 66.7$, then increases for larger mass load values. The corresponding loop isolator mode shapes are shown in Figure 2.22 for $l = 2$ and $f = 10$ (giving $\delta = 0.021$). The dashed curve gives the equilibrium configuration, and the mode shapes are similar to those for the free vibration of the pinched loop (shown in Figure 1.26). Here, only the symmetric mode shapes (the second and fourth mode shapes in Figure 1.26) appear because the midpoint of the loop (at $s = l/2$) is constrained to move in the vertical direction only. The resulting nondimensional frequencies for this case are $\Omega = 6.09$, 41.89, and 98.40.

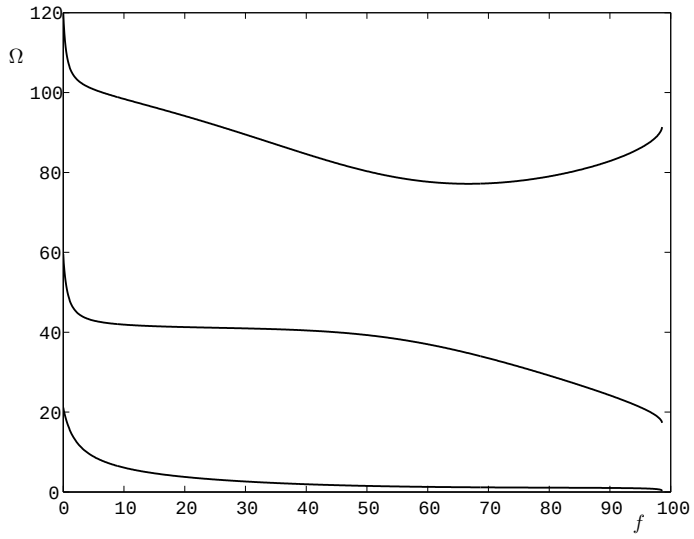

Figure 2.21: First three natural frequencies as a function of mass load for the pinched loop isolator with $l = 2$.

2.3.4 Vibration Isolation

Forced vibration results are again found using the solution forms given in equations 2.10 and the resulting dynamic variable equations 2.11. Here, the boundary conditions are

$$\begin{gathered} x_a(0) = u_o, \quad x_b(0) = y_a(0) = y_b(0) = \theta_a(0) = \theta_b(0) = 0, \\ y_a(l/2) = y_b(l/2) = \theta_a(l/2) = \theta_b(l/2) = 0, \\ p_a(l/2) = -\tfrac{f}{2}\Omega^2 x_a(l/2), \quad p_b(l/2) = -\tfrac{f}{2}\Omega^2 x_b(l/2), \end{gathered} \tag{2.24}$$

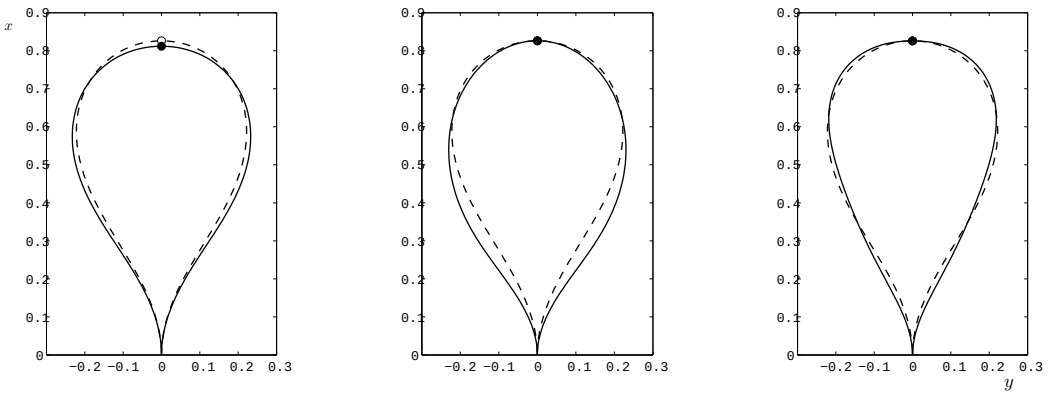

Figure 2.22: Pinched loop isolator mode shapes for $l = 2$ and $f = 10$ ($\delta = 0.021$). Dashed curve and open circle: equilibrium, solid curves and closed circles: mode shape. The first three natural frequencies are $\Omega = 6.09$, 41.89, and 98.40.

for specified values of forcing amplitude, u_o, and frequency, Ω, and the transmissibility is given by

$$Tr = \frac{\sqrt{x_a(l/2)^2 + x_b(l/2)^2}}{u_o}. \tag{2.25}$$

Numerical transmissibility results for $l = 2$, $f = 10$, and $c = 0.5$ are shown in Figure 2.23, where, as for the vertical clamped-clamped beam isolator, dynamic vibration shapes corresponding to the first three transmissibility peaks (at forcing frequencies near the first three natural frequencies) are similar to the corresponding mode shapes. Experimental transmissibility results are found by attaching the loop base to a shaker (as seen in Figure 2.16) that oscillates in the vertical direction. The shaker output (or excitation) is in the form of a sinusoidal sweep over a specified range of frequencies. The motions of both the sliding mass and the base are measured and the resulting Fourier Transform ratio gives the transmissibility. Experimental results are shown in Figures 2.24 and 2.25. Figure 2.24 gives results for a nondimensional length $l = 1.987$, where $f = 29.29$ in (a) and $f = 44.60$ in (b). The natural frequencies for this case are found numerically using the free vibration equations, giving 3.33, 50.74, and 111.45 Hz for $f = 29.29$ and 2.13, 49.62, and 102.45 Hz for $f = 44.60$. The experimental transmissibility peaks occur at 3.68, 52.56, and 120.47 Hz and 2.56, 51.63, and 112 Hz for $f = 29.29$ and $f = 44.60$, respectively. In Figure 2.24, results for $l = 1.479$ are plotted, where $f = 29.29$ in (a) and $f = 44.60$ in (b). The numerically-computed natural frequencies are 6.49, 91.93, and 214.10 Hz for $f = 29.29$ and 4.60, 91.50, and 206.19 Hz for $f = 44.60$. The experimental transmissibility peaks occur at 6.81, 94.25, and 222.06 Hz and 4.94, 94.19, and 215.88 Hz for $f = 29.29$ and $f = 44.60$, respectively. For both lengths, numerical

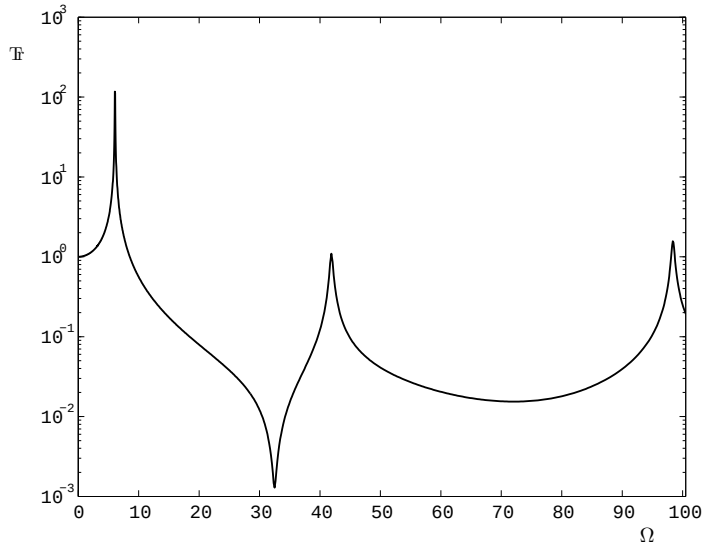

Figure 2.23: Numerical transmissibility results for the pinched loop isolator with $l = 2$, $f = 10$, and $c = 0.5$.

tranmissibility results are found using a damping coefficient of $c = 1$. Although experimental peaks occur near the numerically-computed natural frequencies, anti-resonances do not appear in the experimental measurements. Because anti-resonances correspond to very small amplitudes of mass motion, experimental measurements at these frequencies are more vulnerable to noise, making them difficult to detect [41].

In the experimental results for each case, there are some additional transmissibility peaks that do not appear in the numerical results. These peaks may correspond to vibration shapes with rotation at the midpoint (where, in the analytical formulation, it is assumed that $\theta(l/2, t) = -\pi/2$). The attachment point of the mass load also has a finite width, experimentally; the analysis assumes this force is applied as a point load. Finally, there may be some asymmetry in the experimental system due to an error in the attachment point location of the mass load. These additional peaks, however, have transmissibility values less than unity, indicating that the pinched loop is an effective isolator.

In both the numerical and experimental results, there is a considerable attenuation of the transmissibility for forcing frequencies above resonance, and it is this resonant frequency that can be tuned by either altering the loop length or static mass load of the system.

While in this case the mass motion is constrained to be purely vertical, the pinched loop isolator

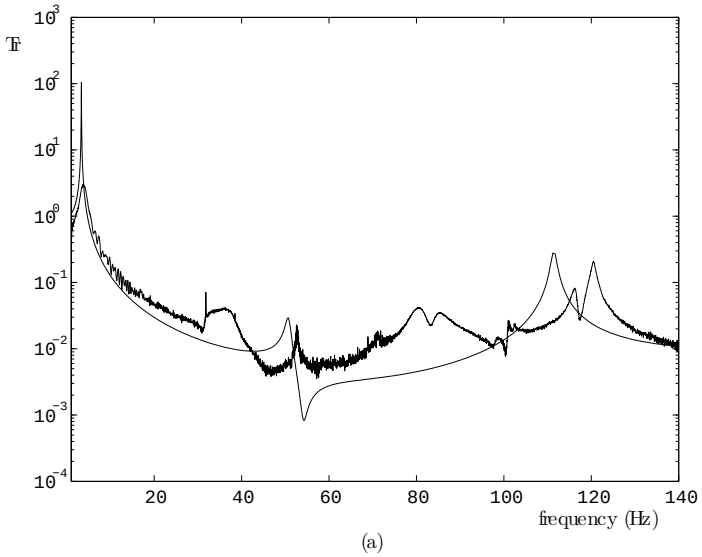

(a)

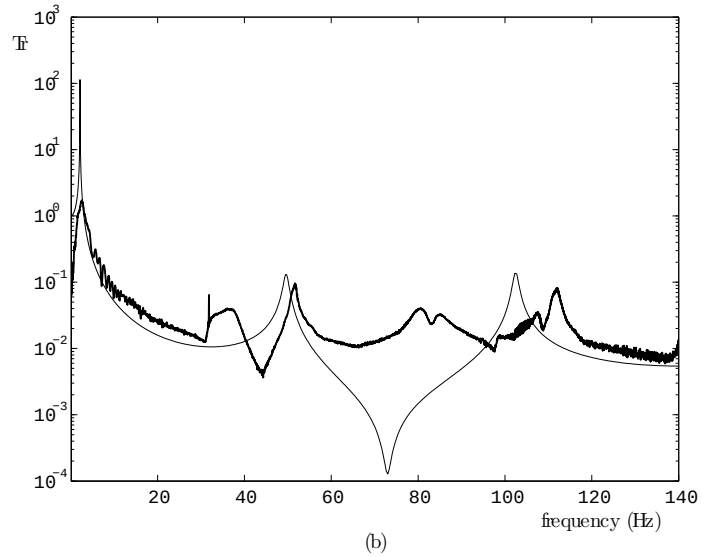

(b)

Figure 2.24: Experimental and numerical transmissibility results for the pinched loop isolator, $l = 1.987$, (a) $f = 29.29$, (b) $f = 44.60$.

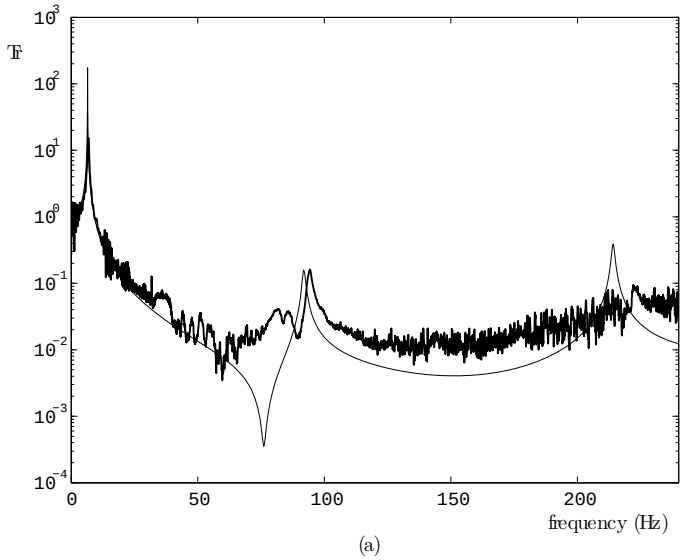

Figure 2.25: Experimental and numerical transmissibility results for the pinched loop isolator, $l = 1.479$, (a) $f = 29.29$, (b) $f = 44.60$.

system is one that may also be studied as a horizontal motion isolator or even a system that isolates motion in both directions simultaneously. This system characteristic makes this isolator particularly advantageous over a helical spring system, where the motion must be limited to be exclusively in one direction.

2.4 Conclusions

Vibration isolation is required in a number of dynamics applications. There are advantages to using a nonlinear vibration isolator, and some such systems have been studied in the literature. Here, three nonlinear isolator systems were investigated, where highly-deformed elastic structures were used as the spring elements. Each has some level of stiffness control, allowing isolation over a desired frequency range.

Both the vertical clamped-clamped beam system and the pinched loop isolator satisfy the requirement of a large initial stiffness, along with a relatively small local stiffness under a nonzero mass load. Numerical results for each system indicate that displacement transmissibility is small for forcing frequencies beyond the fundamental resonance. Experimental results for each confirm that these systems are effective isolators. The horizontal system is also effective in that mode localization occurs in the strut that undergoes direct excitation. Each system also has an amount of system asymmetry in the analysis and/or experiment.

Chapter 3

Nonlinear Beam Vibrations

3.1 Introduction

The governing equation for free, linear, beam bending vibration about a trivial equilibrium configuration is given in equation 1.17, where the self-weight of the beam is neglected. As shown in Sections 1.1.2, analytical mode shapes may be assumed and used to find corresponding exact, analytical frequencies for specified boundary conditions. Even if the self-weight is included, small-amplitude vibration modes and frequencies about a stable, trivial equilibrium (as in Section 1.1.2 and 1.3) or a highly-deformed equilibrium (as in Section 1.6 and Chapter 2) are easily found using numerical integration and the shooting method. These results are accurate for small-amplitude beam vibrations, but if large-amplitude vibration results are desired, other analytical or numerical methods (some of which are outlined in Chapter 1) are necessary.

A number of studies of nonlinear beam vibrations (and solution approximation methods) appear in the literature. Marur outlined many of the analytical and numerical solution methods that have been used [44]. Governing equations were typically derived via energy methods [45, 46] or by summing the assumed forces acting on the system (as in the present study). Many of the studies have been performed using Cartesian (rather than arclength) coordinates, limiting the vibration amplitudes and static deflection sizes that may be considered [47–51]. Most used analytical methods where the solution forms were assumed (as the product of spatial and temporal functions, for example) [45, 52]. Typically the analytical methods used include perturbation, Galerkin, and/or harmonic balance methods [53–56]. Other studies have been performed on beam vibrations that cause snap-through [57,58] and on nonlinear vibrations that result in chaotic behavior [59,60]. There is also some experimental work in the literature [54,59,61,62], where the results were compared with analytical methods or, as in Nandakumar and Chatterjee [63], experimental results were used to derive a nonlinear model for dynamic beam deflection.

Here, as in previous sections, the beam is assumed to be inextensible, and shear deformation is neglected. The elastica equations are considered, and perturbation and finite difference methods (both outlined in Chapter 1) are used to study various boundary condition and self-weight cases. Results are compared with those available in the literature.

3.2 Trivial Equilibrium Configurations

First, nonlinear vibrations about trivial equlibrium configurations with various boundary conditions are studied. The nondimensional quantities given in equations 1.25 and 1.34 are used, where setting $w = 0$ is equivalent to neglecting the self-weight of the system.

Luongo et al. [46] studied nonlinear vibrations for the four boundary condition cases shown in Figure 3.1, where, for each case, A gives the maximum amplitude of motion in the first vibration mode. Self-weight was neglected in the analysis, and both immovable and movable ends were considered. Because in the present study the beam is assumed to be inextensible, results are compared with the movable end case results (indicated in the schematic by rolling boundary conditions). Some

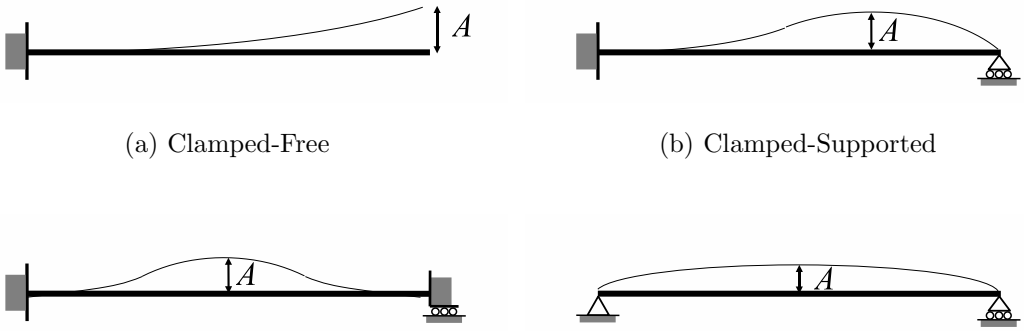

(a) Clamped-Free (b) Clamped-Supported

(c) Clamped-Slider (d) Pinned-Supported

Figure 3.1: Boundary condition cases for a study of nonlinear vibrations about trivial equilibrium configurations [46].

perturbation method results for the clamped-free (cantilever) case (corresponding to Figure 3.1(a)) are shown in Section 1.4.2, where the method is performed on the elastica equations. The resulting backbone curve (with $w = 0$) corresponding to motion in the first mode is plotted with the solid curve in Figure 1.18. Because the vibration frequency, Ω_{N1}, increases with amplitude, the system is hardening in the first mode. Again, this curve may be expressed analytically by equation 1.120 where Ω_1 is the first linear natural frequency, a_1 is the amplitude of lateral tip motion, and λ_1 is a function of the frequency, Ω_1, mode shape, $\phi_1(s)$, and constants, p_o and q_o, resulting from the boundary conditions. As shown in Figure 1.10, the first cantilever vibration mode shape that is found numerically (using the shooting method) agrees very closely with the analytical mode shape (given by equation 1.23 with $b = 1.875$ and $\sigma = 0.7341$), where weight is neglected (or $w = 0$).

So the same value of λ_n (and consequently the same analytical nonlinear frequency-amplitude relationship) results from the use of either the numerical or analytical mode shape. Note that, because the vibrations considered here are about trivial equilibria, and x gives the longitudinal coordinate, $x = s$ (and $\phi(s) = \phi(x)$).

Luongo et al. [46] derived an analytical expression for the free vibration frequency-amplitude relationship using arclength coordinates, an energy method, and a perturbation method, resulting in [46]

$$\frac{\Omega_{Nn}}{\Omega_n} = 1 + \left(\frac{3b}{8} - \frac{c}{4}\right) a^2 + \left[-\frac{15b^2}{256} + \frac{9c}{64}(c-b)\right] a^4, \tag{3.1}$$

where

$$b = \frac{2\int_0^1 \phi_n'^2 \phi_n''^2 ds}{\int_0^1 \phi_n''^2 ds}, \quad c = \frac{\int_0^1 \left(\int_0^s \phi_n'^2 ds\right)^2 ds}{\int_0^1 \phi_n^2 ds}, \tag{3.2}$$

and $A = a\phi_n(s_m)$, where s_m gives the arclength coordinate at which the maximum deflection in the mode occurs (i.e., the location at which A is measured in Figure 3.1). For first-mode ($n = 1$) vibration of the cantilever (with $w = 0$), the results from the study are plotted (where $s_m = 1$), together with the backbone curve resulting from a perturbation method using the elastica equations, in Figure 3.2. The dashed curve is plotted using equation 3.1, and the quadratic equation (generated by using only the first two terms of equation 3.1) is plotted with a solid curve. The second-order elastica perturbation results (plotted with data points and given by equation 1.120) agree closely with the quadratic approximation found by Luongo et al. [46], and the approximations are in agreement up to a deflection size of about $A = 0.35$, or 35 percent of the beam length.

The first-mode backbone curves for the three remaining boundary conditions shown in Figure 3.1 were also found by Luongo et al. [46]. For these cases, equations 3.1 and 3.2 still apply, where ϕ_1 is the analytical first-frequency mode shape for specified boundary conditions. For the clamped-supported and clamped-slider beams, the analytical mode shapes are given by equation 1.23, where $b = 3.927$ and $\sigma = 1.0008$ (for the clamped-supported case, with $s_m = 0.58$) and $b = 4.730$ and $\sigma = 0.9825$ (for the clamped-slider case, with $s_m = 0.5$) [11]. The analytical mode shape for vibration in the first mode of the pinned-supported beam is given by $\phi_1(s) = \sin \pi s$ (and $s_m = 0.5$).

The analytical backbone equation resulting from the elastica perturbation analysis (equation 1.120) also applies for the remaining boundary condition cases. Again, the equation involves the linear vibration frequency, Ω_1, and mode shape, ϕ_1, which may be found analytically (given above, for each case) or numerically (using the shooting method). The remaining unknown values in

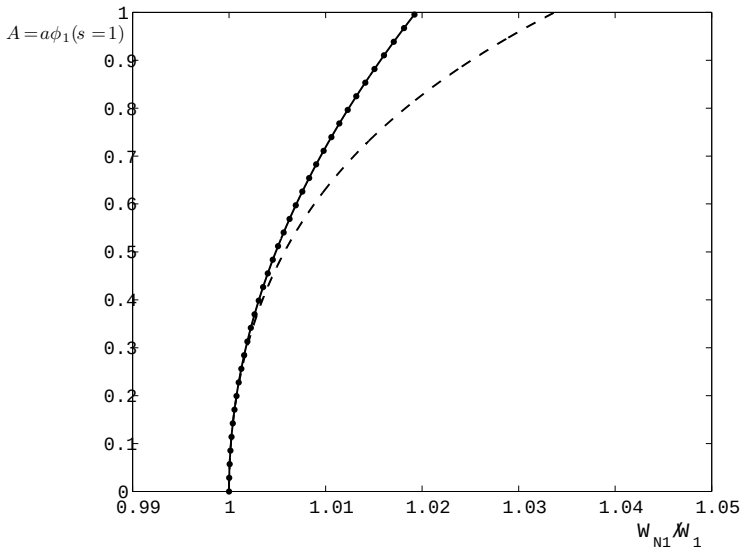

Figure 3.2: Backbone curves for cantilever vibration (with $w = 0$) in the first mode. Data points: elastica perturbation method; solid curve: energy perturbation method, quadratic equation; dashed curve: energy perturbation method, fourth-order equation [46].

equation 1.120 are p_o and q_o, which, as shown in Section 1.4.2, are determined by the boundary conditions. For the clamped-supported case, the values are chosen such that they satisfy $p(s = 1, t) = 0$ and $q(s = 0.58, t) = 0$. For the clamped-slider and pinned-supported cases, $p(1, t) = 0$ and $q(0.5, t) = 0$. The resulting backbone curves are plotted in Figure 3.3, where, for each boundary condition case, the quadratic and fourth-order equations derived by Luongo et al. [46] are plotted along with the elastica perturbation results. For each of the boundary conditions, the system is softening in the first mode, and agreement between the two quadratic curves (from the elastica and energy methods) is good. However, for each pair of curves (quadratic and fourth-order) the agreement is only good up to about 6 percent of the beam length (or $A = 0.06$). This range of agreement is significantly smaller than that for the cantilever vibration, because the degree of change in the nonlinear frequency (or the amount of system softening or hardening) is larger. For example, for the clamped-slider boundary condition, a frequency decrease of about 2 percent occurs for a dynamic amplitude of $A = 0.07$, compared with a similar increase in frequency for the cantilever corresponding to an amplitude of $A = 0.8$, or 80 percent of the beam length.

As shown in Section 1.3.5, a finite difference method may also be used to generate the backbone curve for nonlinear vibrations. The amplitude of steady-state free vibration in the lateral direction ($|y(s = 1, t)|$ of the upright cantilever, approximated above by $A = a\phi(s = 1)$) is found, and

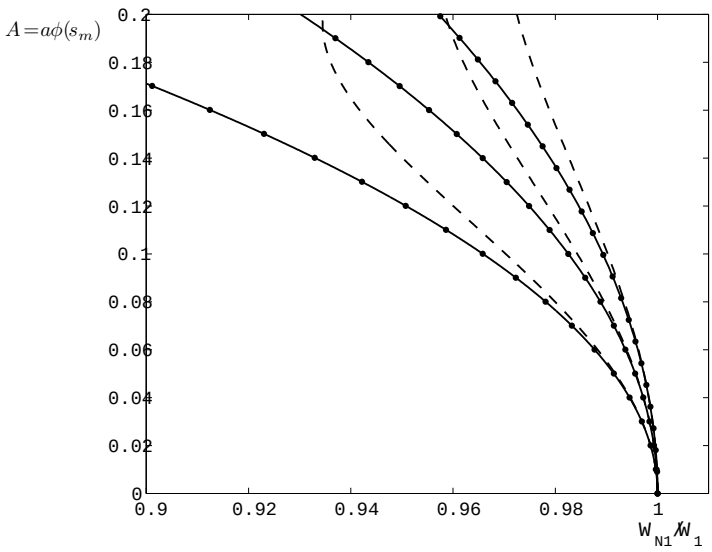

Figure 3.3: Backbone curves for vibration in the first mode of beams (with $w = 0$) with various boundary conditions. Data points: elastica perturbation method; solid curve: energy perturbation method, quadratic equation; dashed curve: energy perturbation method, fourth-order equation [46]. Each pair of curves represents the boundary conditions: (left to right) clamped-slider, pinned-supported, clamped-supported.

the period of vibration at the resulting amplitude is determined, giving the nonlinear vibration frequency, Ω_{N1}. These results are plotted as data points, along with the second- and fourth-order backbone approximations, in Figure 3.4. It can be seen in the figure that the fourth-order equation gives results that are accurate for a larger range of amplitudes than the second-order approximation. However, these perturbation results are not as accurate as those from the finite difference method, which captures the "fold-over" that occurs for large deflections, where the lateral deflection reaches a maximum, $y(s = 1, t) \approx 0.832$, and then decreases. This behavior can be seen in Figure 1.14, where nonlinear vibration shapes are plotted for various deflection sizes.

For each boundary condition case, the second-order elastica perturbation approximations agree very closely with the quadratic equations derived by Luongo et al., but one advantage of the elastica perturbation method is that it may be used to analyze nonlinear vibrations of heavy beams (where $w > 0$). Equation 1.120 may again be used, where the linear mode shape, $\phi(s)$, is found numerically for a specified nonzero weight, w, and boundary conditions, using the shooting method (where $\phi(s) = y_d(s)$). In the case of the upright heavy cantilever, the trivial equilibrium configuration is stable for weight values $0 \leq w < 7.837$. Backbone curve approximations resulting from this analysis are shown for three nonzero, pre-buckling weight values, $w = 5.859$, 2.989, 1.655, along with the

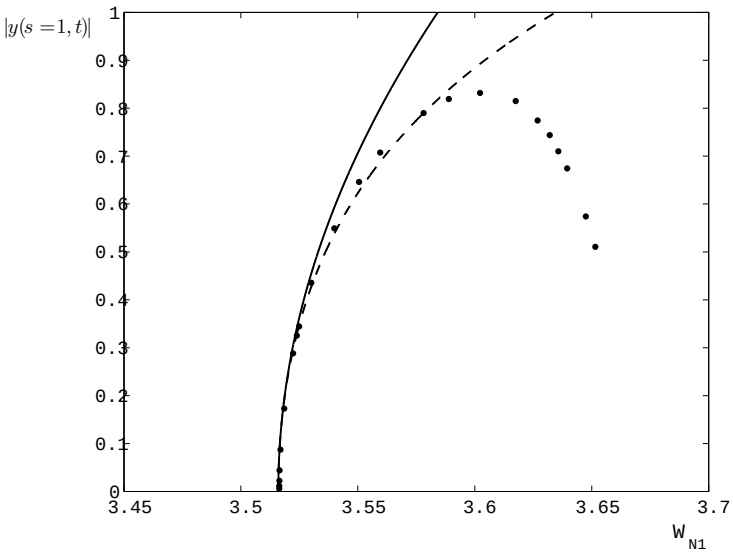

Figure 3.4: Backbone curve approximations for the cantilever with $w = 0$. Solid curve: second-order approximation; dashed curve: fourth-order approximation; data points: finite difference results from steady-state free vibrations.

results for $w = 0$, in Figure 3.5. For these four weight values, the fundamental frequencies are $\Omega_1 = 1.769$, 2.768, 3.124, and 3.516, respectively. Also plotted (as data points) are finite difference method results for each of the self-weight values. It can be seen that, as the self-weight is increased, the system is increasingly hardening in the first mode, and the second-order elastica perturbation method results are accurate up to a dynamic amplitude of about half of the beam length (or $|y(1,t)| = 0.5$). The finite difference method may also be used to determine the nonlinear dynamic beam response to excitation. For horizontal base excitation of the heavy cantilever, the method is applied as outlined in Section 1.3.5. Equations 1.86 are again used, where a nonzero damping is included ($c > 0$), and the boundary conditions are changed such that

$$\begin{gathered} x(0,t) = \theta(0,t) = 0, \quad y(0,t) = u(t), \\ m(1,t) = p(1,t) = q(1,t) = 0, \end{gathered} \tag{3.3}$$

where $u(t)$ gives the horizontal base excitation (and $u(t)$ is nondimensionalized as before, where $u = U/L$). For the discretized system, these boundary conditions become

$$\begin{gathered} x_1^j = \theta_1^j = 0, \quad y_1^j = u^j, \\ m_{n+1}^j = p_{n+1}^j = q_{j+1}^j = 0, \end{gathered} \tag{3.4}$$

where $u^j = u(t^j)$. If the base excitation is sinusoidal (with a constant amplitude and frequency), then the excitation function is given by $u^j = u_o \sin \Omega t^j$. However, if an excitation with a varying frequency

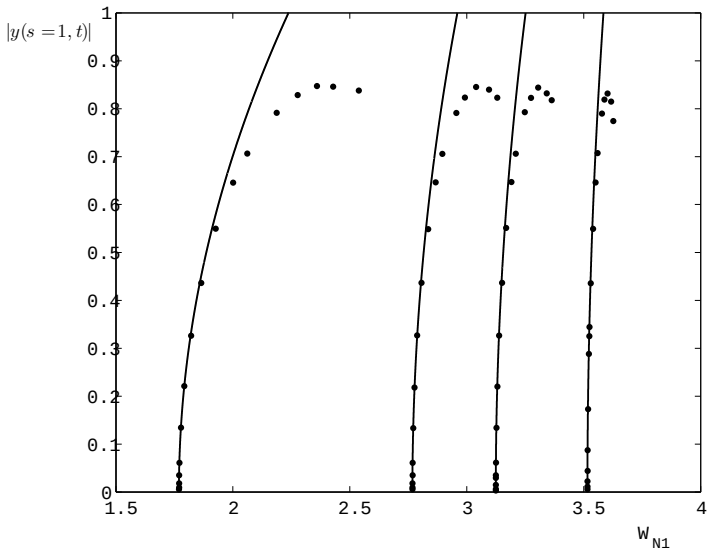

Figure 3.5: Backbone curve approximations for the upright heavy cantilever with weight values (from left to right) $w = 5.859$, 2.989, 1.655, 0, where the natural frequencies are $\Omega_1 = 1.769$, 2.768, 3.124, 3.516, respectively. Solid curve: elastica perturbation results; closed circles: finite difference method results.

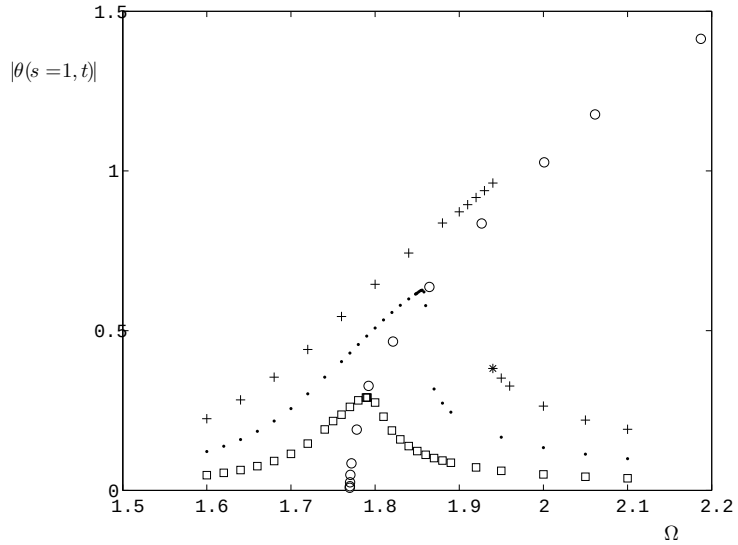

Figure 3.6: Numerical amplitude response data for the heavy, upright cantilever (with $w = 5.859$), using the finite difference method. Open circles: backbone approximation from free-vibration analysis; squares: $u_o = 0.005$; data points: $u_o = 0.013$; crosses and asterisk: $u_o = 0.025$.

is to be modeled, a sine sweep function can be applied. For a linear sinusoidal sweep excitation over a time range $0 < t < t_f$, with beginning and ending frequencies Ω_o and Ω_f, respectively, the frequency as a function of time is given by

$$\Omega(t) = \Omega_o + t\left(\Omega_f - \Omega_o\right)/t_f. \tag{3.5}$$

The "chirp function", $u(t)$, is then given by $u(t) = u_o \sin\phi(t)$, where $\dot{\phi}(t) = \Omega(t)$. The function can then be written

$$u(t) = u_o \sin\left(\Omega_o t + \frac{1}{2t_f}(\Omega_f - \Omega_o)t^2\right). \tag{3.6}$$

Similarly, an excitation function with an exponential sine sweep is found and given by

$$u(t) = u_o \sin\left((\Omega_o - \Omega_f)e^{-t} + \Omega_f t\right). \tag{3.7}$$

The steady-state response amplitudes (for constant-frequency base excitation, $u = u_o \sin\Omega t$, using the finite difference method) are shown in Figure 3.6 for $w = 5.859$, along with the backbone curve found using finite differences. The tip angle amplitude is plotted, and the damping constant is $c = 0.06$. The forcing amplitudes are $u_o = 0.005$, 0.013, and 0.025. It can be seen that, for larger forcing amplitudes, the response amplitude is discontinuous just beyond nonlinear resonance for this hardening system. A smaller-amplitude, steady-state motion is found (plotted with an asterisk) by applying an exponential sine sweep (as given in equation 3.7) with $\Omega_o = 3.0$. It can be seen that these lightly damped, forced vibration results agree well with the numerical backbone curve data.

Finally, it is shown that lightly damped, free vibration results may be used to find accurate backbone curve data. Nandakumar and Chatterjee [63] used this method with an experimental cantilever system to generate a backbone curve. Here, the finite difference method is again used for the heavy, upright cantilever with $w = 5.859$. The damping coefficient is set to a small, nonzero value, $c = 0.03$, and a large initial deflection is used to initialize the algorithm. The initial, deflected configuration is shown in Figure 3.7(a). The amplitude of motion decays, and the resulting time series of tip angle motion, $\theta(1,t)$, is shown in Figure 3.7(b). These time series data are used to generate a backbone curve. Between consecutive maxima, the maximum motion amplitudes are averaged, and the period is measured by $t_2 - t_1$, where t_1 is the time at which the graph crosses the t-axis (with a negative slope), and t_2 is the next time where this occurs. The amplitudes and frequencies of motion for each cycle are recorded and plotted as data points in Figure 3.8, where the steady-state motion data are also shown. The lightly damped free vibration data are seen to closely agree with backbone curve generated from undamped, steady-state motion. Generating the

(a) Initial, Deflected Shape

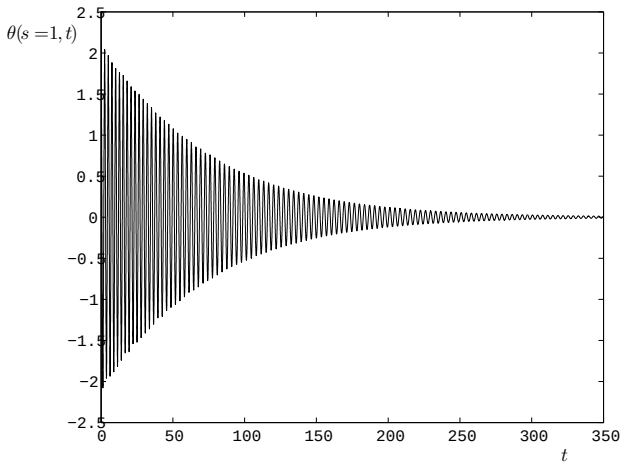

(b) Time series, cantilever tip angle

Figure 3.7: Damped, free vibration of the heavy cantilever with $w = 5.859$, $c = 0.03$, and $\theta(s = 1, t = 0) = 2.062$.

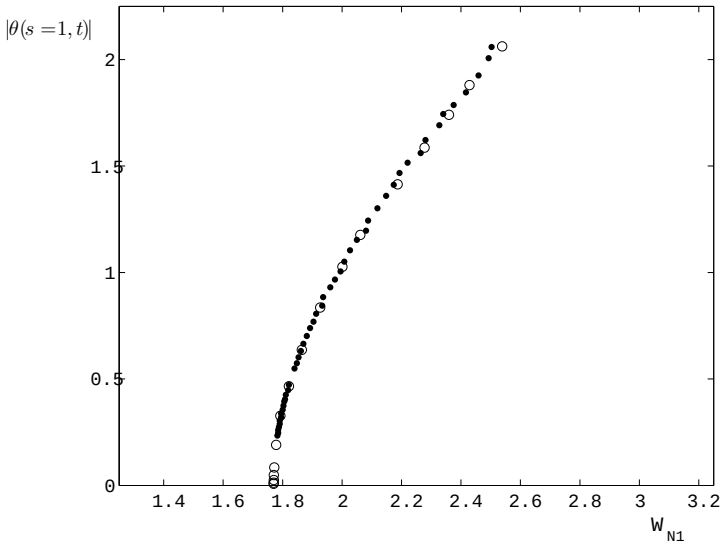

Figure 3.8: Backbone curve approximations for the heavy, upright cantilever (with $w = 5.859$) from steady-state vibration and lightly damped vibration results (using a finite difference method). Open circles: steady state vibration; closed circles: damped, free vibration.

backbone curve with this method greatly reduces computation time; several data points may be found from a single, damped-motion time series.

3.3 Highly Deformed Equilibrium Configurations

So far, results have been shown for large-amplitude beam vibrations about trivial equilibrium configurations. The finite difference method, however, may be used to model motion about highly deformed equilibria. The clamped-clamped beam, for example, was introduced in Section 1.6.2. For a specified nondimensional end-shortening, δ, and self-weight, w, the buckled static shape may be found via the shooting method. Small-amplitude vibration frequencies and mode shapes may also be determined with this method (also described in Section 1.6.2). Analytical backbone curves for this case (with a specified end-shortening and self-weight) can be found using a perturbation method, but for cases with nontrivial equilibria, the equations become considerably more involved. Here, the finite difference method is used to compute large-amplitude motions of the clamped-clamped beam.

As shown in the preceding section, accurate backbone curve approximations may be found by modeling lightly damped, free vibration. Here, backbone curves are obtained by finding steady-state, undamped, free vibration frequencies and amplitudes for large-amplitude motion. The initial

deflections for these cases are determined by forcing the lightly damped system at the linear-vibration fundamental frequency. For the case of the horizontal, clamped-clamped, heavy beam, the horizontal excitation takes the form

$$u(t) = u_o \sin \Omega_1 t, \tag{3.8}$$

giving the boundary conditions

$$x(0,t) = u_o \sin \Omega_1 t, \quad x(1,t) = 1 - \delta + u_o \sin \Omega_1 t. \tag{3.9}$$

The system is forced in this manner, and a local deflection maximum is found. This configuration is then used as an initial deflection for free, undamped vibration, where the horizontal coordinates are reset such that

$$x_{free}(s,0) = x_f(s,t_f) - u_o \sin \Omega t_f, \tag{3.10}$$

where t_f is the time at which the desired deflection occurs in the horizontal excitation results, and x_f gives the horizontal deflection at t_f with forcing. Free, undamped, vibration may be initialized with this initial deflection and the amplitudes and period of motion are recorded. The finite difference method may again be used with a small damping coefficient value to find motion of slightly smaller amplitudes. The amplitudes and frequency are again recorded and this procedure is repeated to generate a backbone curve for the specified parameters.

For end-shortening $\delta = 0.05$ and self-weight $w = 0$, this method is used, where the initial deflection for motion at the largest recorded amplitude is plotted in Figure 3.9(a). For larger initial deflection magnitudes, numerical convergence could not be met in the free vibration algorithm. The resulting backbone curve is shown in Figure 3.9(b), where the measured amplitude is the angle of the tangent to the beam at the midpoint (i.e., $|\theta(0.5,t)|$). It can be seen that the system is initially hardening, but becomes softening for larger amplitudes.

Phase projections for $\theta(0.5,t)$ are shown in Figure 3.10 for free vibration at various initial deflection magnitudes. For small-amplitude vibrations, the phase projections are ellipses (where the ratio of the intersections with the velocity and displacement axes is the natural frequency, Ω_j, of the j^{th} mode). For the specified parameter values, $\Omega_1 = 44.16$. It is clear that, for large amplitudes of motion, the phase projection is not elliptical. Some numerical damping is also evident in this outermost curve thickness.

The horizontal and vertical motions at points on the left half of the beam are plotted in Figures 3.11(a) and 3.12(a) for free vibration, where the initial deflection is as shown in Figure 3.9(a). It can be seen that the time series are very different along varying arclength coordinates, and that

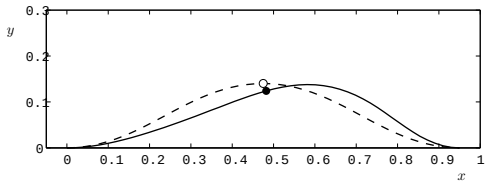

(a) Initial deflection.

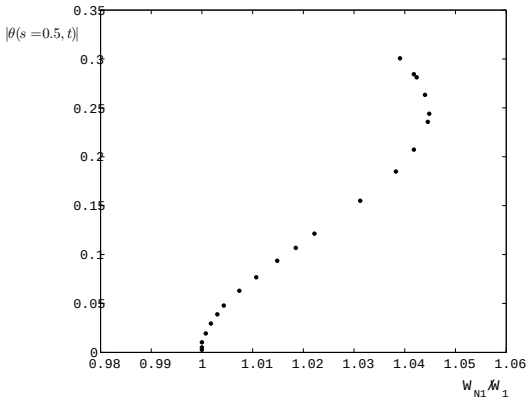

(b) Backbone curve approximation

Figure 3.9: Initial deflection and backbone curve approximation using finite differences for the postbuckled, clamped-clamped beam with $w = 0$ and $\delta = 0.05$ (giving a linear natural frequency of $\Omega_1 = 44.16$). In (a) the dashed curve gives the equilibrium configuration and the solid curve gives the deflected shape. Circles are located at $s = 0.5$ on each configuration.

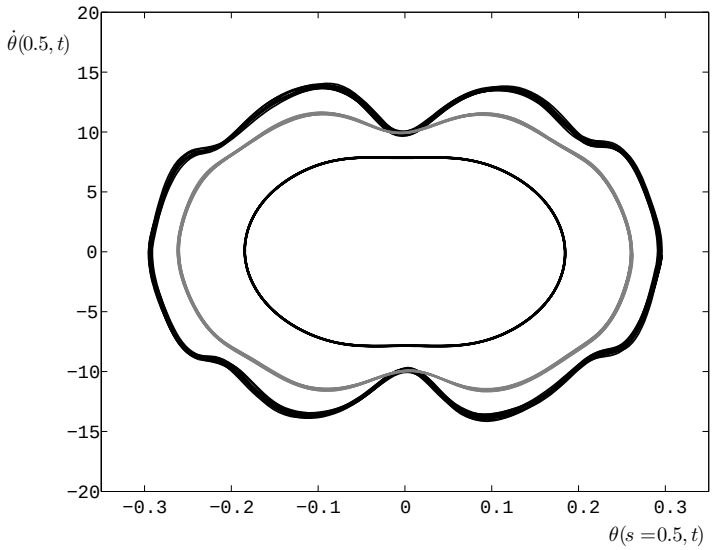

Figure 3.10: Phase projections of the midpoint angle motion of the clamped-clamped beam with $w = 0$ and $\delta = 0.05$ for varying amplitudes.

higher harmonics of the first frequency are present. In Figure 3.12(a), the time series of vertical motion at $s = 0.1$, 0.3, and 0.5 are plotted. The vertical equilibrium deflections at these points are $y_e(0.1, 0.3, 0.5) = 0.014$, 0.092, and 0.140, and it can be seen that the vertical motions at these beam locations are not symmetric about the equilibrium values. In fact, the beam midpoint ($s = 0.5$) can be seen to never even dynamically pass through equilibrium. This behavior can also be seen in the phase projection of vertical motion at $s = 0.5$ plotted in Figure 3.12(b). The projections in this figure and Figure 3.11(b) also indicate that the midpoint bounces between the time series maxima of each cycle.

A similar process is used to approximate the backbone curve for end-shortening $\delta = 0.5$ (and, as before, $w = 0$). The initial deflection used to generate the free vibration data is shown in Figure 3.13(a), and the resulting backbone curve approximation is plotted in Figure 3.13(b). Here, the curve is initially softening and then becomes hardening at larger amplitudes. The free-vibration phase projection for $\theta(0.5, t)$ corresponding to the largest initial deflection is shown in Figure 3.14.

Results may also be found for the case of a nonzero self-weight. Here, $w = 32.56$, as chosen by Santillan et al. [14], and the backbone curve approximations for $\delta = 0.05$ and 0.5 are shown in Figure 3.15 along with the numerical data for $w = 0$. The amplitude, A, is plotted, where

$$A = \frac{max(x(0.24, t)) - min(x(0.24, t))}{2}. \tag{3.11}$$

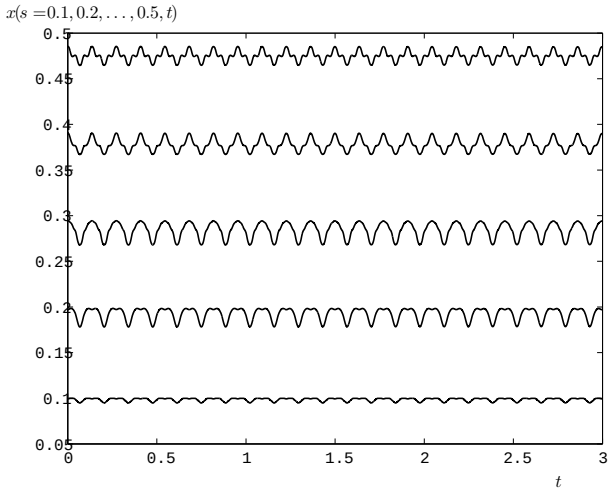

(a) Time series.

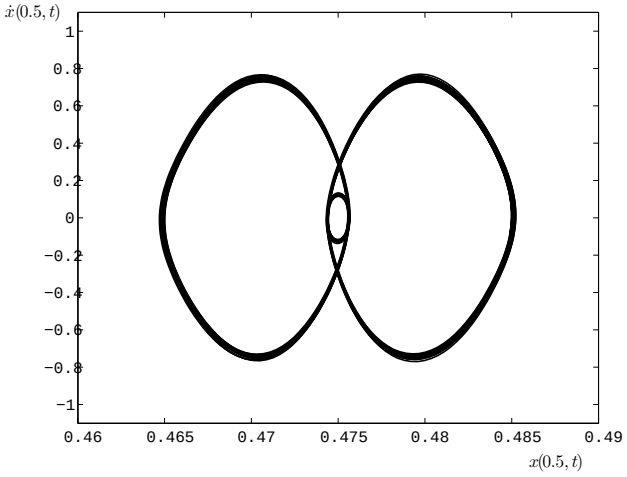

(b) Phase projection.

Figure 3.11: Time series and phase projection of the horizontal motion of the clamped-clamped beam (with $w = 0$ and $\delta = 0.05$). (a) Horizontal motion at $s = 0.1, 0.2, \ldots, 0.5$. (b) Phase projection of horizontal motion at $s = 0.5$.

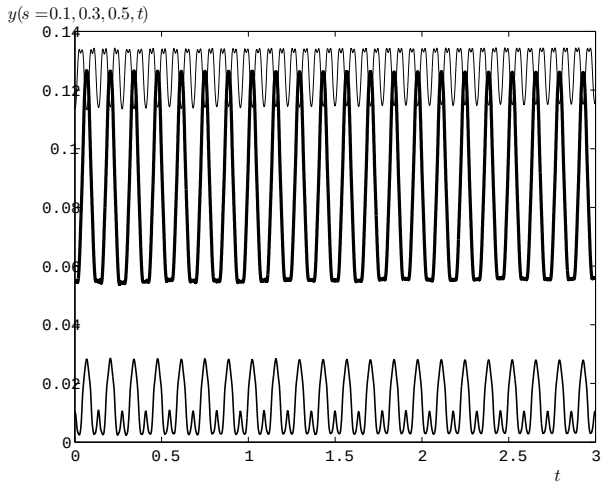

(a) Time series.

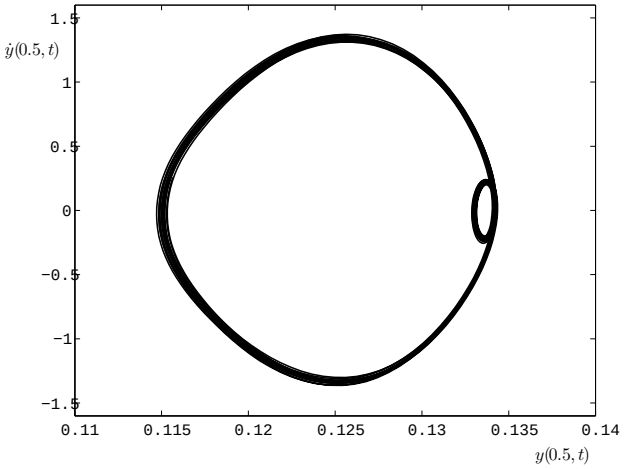

(b) Phase projection

Figure 3.12: Time series and phase projection of the vertical motion of the clamped-clamped beam (with $w = 0$ and $\delta = 0.05$). (a) Vertical motion at $s = 0.1$, 0.3, and 0.5. Vertical equilibrium deflections at these points are $y_e(s = 0.1, 0.3, 0.5) = 0.014$, 0.092, and 0.140. (b) Phase projection of vertical motion at $s = 0.5$.

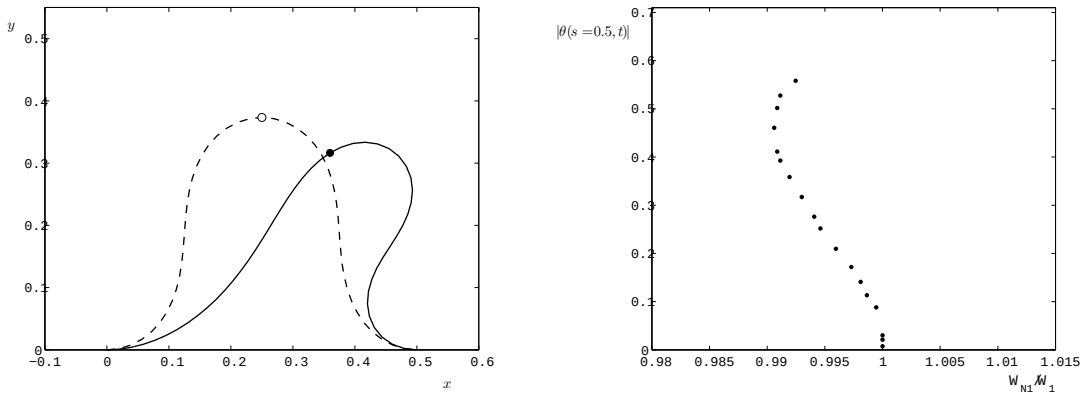

(a) Initial deflection. (b) Backbone curve approximation

Figure 3.13: Initial deflection and backbone curve approximation using finite differences for the postbuckled, clamped-clamped beam with $w = 0$ and $\delta = 0.5$ (with $\Omega_1 = 37.28$). In (a) the dashed curve gives the equilibrium configuration and the solid curve gives the deflected shape. Circles are located at $s = 0.5$ on each configuration.

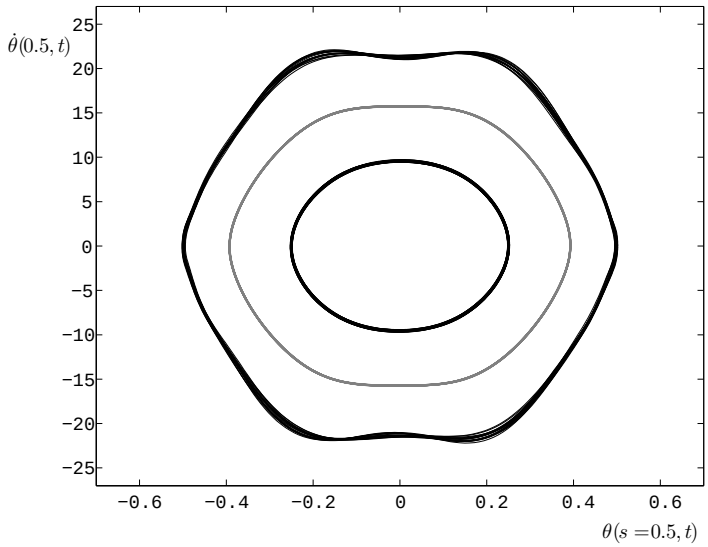

Figure 3.14: Phase projections of the midpoint angle motion of the clamped-clamped beam with $w = 0$ and $\delta = 0.05$ for varying amplitudes.

Again, the motion is not symmetric about equilibrium for large-amplitude motion. For $\delta = 0.05$, the self-weight causes the backbone curve to become more hardening. Even for very small dynamic amplitudes, the frequency is seen to increase significantly. This behavior may explain why, for these self-weight and end-shortening values, the experimental data lie to the right of the numerical data (calculated by assuming harmonic motion) in Figure 7 of Santillan et al. [14]. For $\delta = 0.5$, the system is initially softening in the first mode, but the variation in frequency is more gradual (and in Figure 7 of Santillan et al. [14], the experimental data are more consistent with the numerical solution for this end-shortening value).

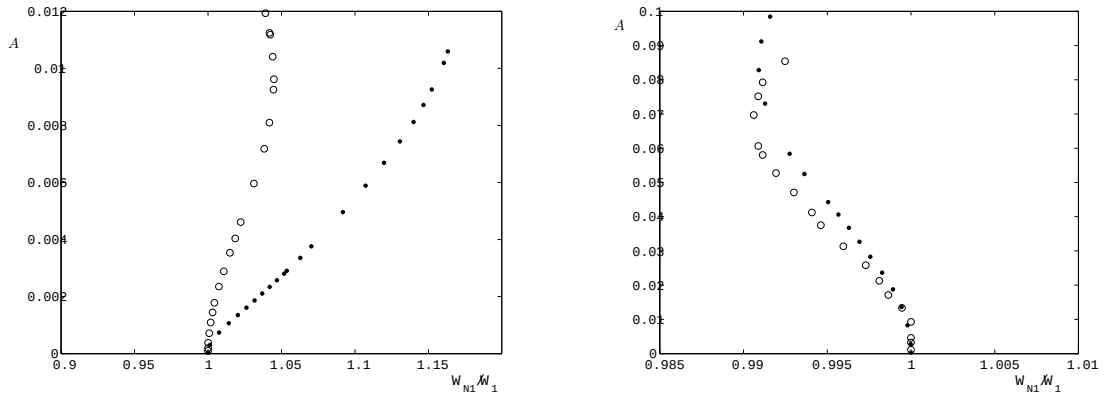

(a) $\delta = 0.05$ (b) $\delta = 0.5$

Figure 3.15: Backbone curve approximations for the clamped-clamped beam with $\delta = 0.05$ and 0.5. A is defined in equation 3.11. Open circles: $w = 0$; closed circles: $w = 32.56$.

Backbone curves may also be found for varying end-shortening values (with $w = 32.56$). The curves are found for larger amplitude ranges as the end-shortening is increased; the horizontal component of motion is small compared to the vertical for small end-shortening, but the motion becomes primarily horizontal as the end-shortening increases. For $\delta = 0.7$, the range of amplitudes is limited by self-contact. It can be seen that the variation in frequency with amplitude of the system varies significantly with end-shortening. For $\delta = 0.1$, 0.2, and 0.3, the system is initially hardening in the first mode, but the backbone curves change direction only for $\delta = 0.1$ and 0.2. For larger end-shortening values, the system is initially softening, and, for $\delta = 0.4$, 0.5, and 0.6, becomes hardening at larger amplitudes.

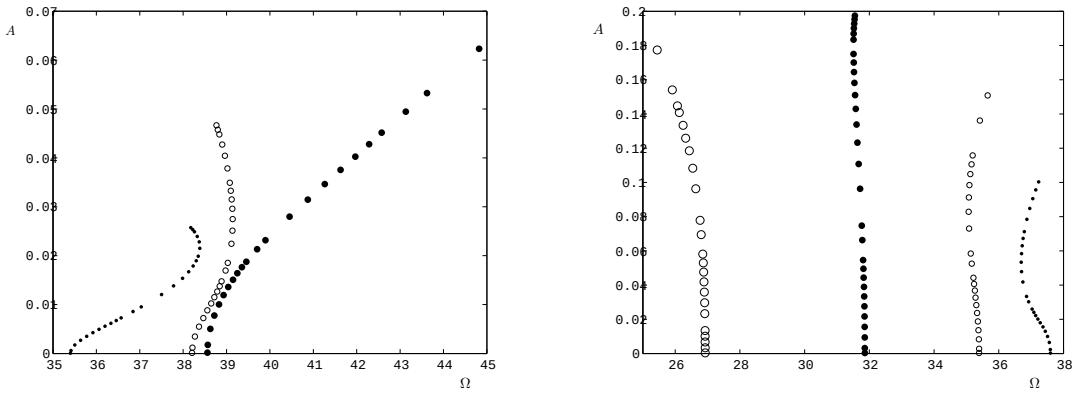

(a) $\delta = 0.1, 0.2, 0.3$ (from left to right)

(b) $\delta = 0.7, 0.6, 0.5, 0.4$ (from left to right)

Figure 3.16: Backbone curve approximations for the heavy, postbuckled clamped-clamped beam (with $w = 32.56$) with varying end-shortening. A is defined in equation 3.11.

3.4 Conclusions

In this section, the perturbation and finite difference methods were used to characterize large-amplitude beam vibrations. Some work on various boundary condition cases has been conducted in the literature, where typically analytical methods are used to solve the governing equations. Results for four boundary condition cases (with trivial equilibria) were compared with those in the literature. These results were found using both a perturbation method and a finite difference method. The elastica equations were also used to find analytical and numerical backbone curves for the upright, prebuckled, heavy cantilever with nonzero self-weight values. The system was shown to be increasingly hardening with self-weight. Amplitude-response curves were obtained for the forced cantilever (with nonzero damping), where the forcing was in the form of horizontal base excitation, and a lightly damped system was shown to give accurate backbone curve results.

Finally, nonlinear vibrations of a postbuckled clamped-clamped beam were investigated. Phase projections and time series show that large-amplitude motion may not be accurately modeled using a single harmonic function. Backbone curves were approximated for two end-shortening values, where self-weight was neglected, and these results were compared to those for a nonzero weight. The amplitude-frequency relationships were also determined for various end-shortening cases with this nonzero weight.

Chapter 4

Future Directions

There are several directions for future work involving this type of elastica analysis. The numerical, analytical, and experimental methods outlined here may be used to investigate the elastica as a model in many applications. The elastica may be used to model cables and subsea pipelines, where additional loading types are considered (e.g., buoyancy, air/fluid flow). Small cantilever beams are also being used in Atomic Force Microscopy (AFM) applications to detect surface features at the molecular level, and so an analysis of the beam dynamics (where appropriate forces are included) is necessary. Highly-deformed, flexible beams are being studied in sensor applications as well [64, 65], and the elastica analysis is certainly useful in characterizing these systems. In some applications, it becomes necessary to model beam contact with a surface. Pipelines resting on the seabed, for example, may buckle under thermal loading, and the uplifted segment may propagate along the pipeline, creating a rolling contact with the seabed. A similar behavior may occur in the handling of paper and fabrics, and this contact may be modeled using the finite difference method. Also, the analysis here is two-dimensional; a natural extension of the research is to conduct a three-dimensional study. The analysis may be applied to problems over a wide range of size scales; DNA strands, for example, may be studied with this analysis [66]. With such an investigation, twisting, torsion, and other out-of-plane motion may be modeled. For many of these behavior types, it is necessary to model dynamic self-contact. Snap-through of the clamped-clamped beam was not modeled here, but may occur for large amplitude forcing in the lateral or longitudinal direction. This behavior type may certainly be studied thoroughly using the method described. Finally, the studies here are performed with the assumption of beam inextensibility. Another research extension, then, is to allow extensibility, or stretching, of the beam.

Here, a preliminary study is performed on the dynamics of subsea risers modeled as slender elastica structures.

4.1 Subsea Pipelines

The use of highly flexible risers for oil drilling purposes is widespread. In terms of simple modeling, a freely hanging riser with minimal bending stiffness can be considered as a catenary.

However, it is common practice to incorporate a buoyant portion relatively close to the sea-bed, and this results in the standard configurations of lazy wave, steep wave, lazy-S, and steep-S, according to whether the riser rests along the sea-bed and the means by which the buoyancy is achieved [67]. It is also reasonable to assume that the riser possesses some bending stiffness.

Here, equilibrium configurations are computed for a baseline case in which typical values of the various parameters are set. Then the following parameters are varied systematically: length of the buoyant section; length of the upper unbuoyed section of the riser relative to water depth; degree of buoyancy; and magnitude of a cross current. Once an equilibrium configuration has been computed, a small-amplitude vibration analysis is conducted (also utilizing a finite difference approach) and described in terms of natural frequencies and mode shapes.

The dimensional baseline values here were taken from the paper by Hong [68], who used an alternative analysis and focused on the lazy-wave configuration. A large-deflection catenary study incorporating a slip joint at the vessel and the effect of steady current is described by Huang and Chucheepsakul [69]. Extensive parameter studies of risers including dynamics for the steep-wave and lazy-wave configurations have been performed by Seyed and Patel [70], and Liu Bergdahl [71], respectively. Some related vibration studies for hanging cables are described by Ahmadi, Smith and Thompson, and Bylsma et al [72–74], and the effect of flow past a circular section has also been studied in the literature [75, 76].

A number of simplifications are used in this study. The analysis is planar and thus no twisting behavior is possible [77], damping is neglected, the riser is assumed to be inextensible, the connection to the vessel is not subject to oscillations, and the numerical examples do not include internal flow. There is nothing in the analysis restricting the riser from lying beneath the seafloor; however, with reasonable parameter values, the uplift along the buoyed section prevents seafloor contact. All of these factors can be incorporated in the analysis if necessary, and in general this approach is somewhat more efficient than a finite element analysis.

4.1.1 Analytical Formulation

The riser is depicted in Fig. 4.1. Points on the riser have coordinates $X(S,T)$ and $Y(S,T)$, and rotation $\theta(S,T)$ with respect to the X axis, where S is the arc length and T is time. The total length of the riser is $L = L_1 + L_2 + L_3$, and the sea depth is H. The length of the unbuoyed segment of the riser at the seafloor connection is L_1 and the buoyed length is L_2. The horizontal distance between the riser ends is D. The internal forces in the strip are denoted $P(S,T)$ and $Q(S,T)$ parallel to the

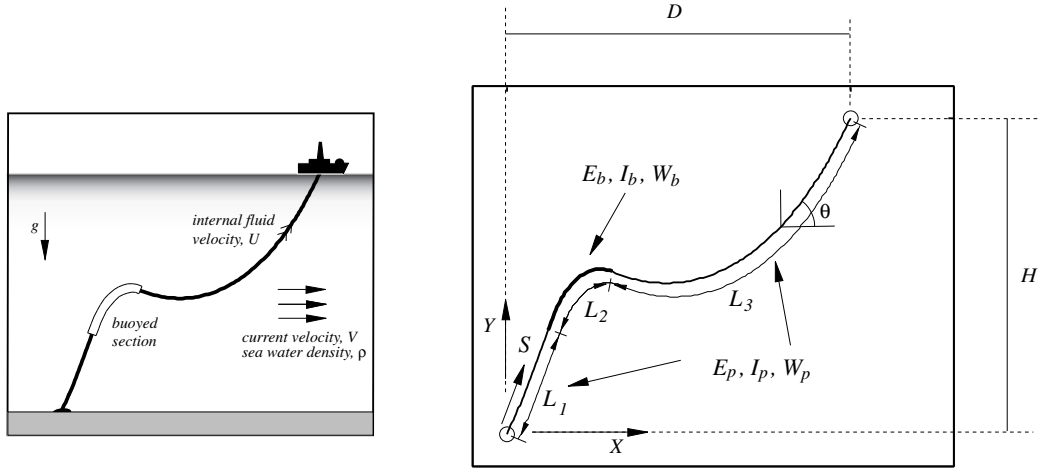

Figure 4.1: Steep wave riser schematic.

X and Y axes, respectively, and the bending moment is $M(S,T)$. The ends of the riser are pinned ($M(0,T) = M(L,T) = 0$).

The governing elastica equations are similar to those in equation 1.32, except that here, the effects of varying self-weight, buoyance, current, and fluid velocity are included, giving

$$\begin{gathered} X_S = \cos\theta, \\ Y_S = \sin\theta, \\ \theta_S = M/E_jI_j, \\ M_S = Q\cos\theta - P\sin\theta, \\ P_S = -(2-B_j)(W_j/g)X_{TT} - 2\mu_f U X_{ST} - \mu_f U^2 X_{SS} + F_j\sin\theta, \\ Q_S = -(2-B_j)(W_j/g)Y_{TT} - 2\mu_f U Y_{ST} - \mu_f U^2 Y_{SS} - W_jB_j, \end{gathered} \tag{4.1}$$

where the subscripts S and T denote partial derivatives. The subscript j denotes values that vary according to the location along the riser length. For example, $E_jI_j = E_pI_p$, the bending stiffness of the unbuoyed riser, along $0 \le S < L_1$ and $L_1 + L_2 < S \le L$, and $E_jI_j = E_bI_b$, the bending stiffness of the buoyed riser, along $L_1 \le S \le L_1 + L_2$. The buoyancy coefficient is $B_j = 1 - (\rho g A_j/W_j)$, and $F_j = \rho r_j C_d V^2$. The weight per unit length in air is given by W_j. The steady current velocity is V, ρ denotes the sea water density, and r and A are the radius and the cross-sectional area, respectively. The drag coefficient is C_d. The inner fluid velocity and mass per unit length are given by U and μ_f, respectively.

The following nondimensional quantities are defined:

$$\begin{gathered}
x = X/H, \quad y = Y/H, \quad s = S/H, \quad d = D/H, \\
l = L/H, \quad l_1 = L_1/H, \quad l_2 = L_2/H, \quad l_3 = L_3/H, \\
m = MH/E_pI_p, \quad p = PH^2/E_pI_p, \quad q = QH^2/E_pI_p, \quad t = (T/H^2)\sqrt{E_pI_pg/W_p}, \\
u = UH\sqrt{\mu_f/E_pI_p}, \quad f_j = F_jH^3/E_pI_p, \quad \beta = \mu_f g/W_p, \\
w_j = W_jH^3/E_pI_p, \quad \Omega = \omega H^2\sqrt{W_p/E_pI_pg}, \quad \gamma_j = E_pI_p/E_jI_j.
\end{gathered} \tag{4.2}$$

where ω is a dimensional vibration frequency.

In nondimensional terms, equations (4.1) become

$$\begin{gathered}
x_s = \cos\theta, \\
y_s = \sin\theta, \\
\theta_s = m\gamma_j, \\
m_s = q\cos\theta - p\sin\theta, \\
p_s = -(2 - B_j)(w_j/w_p)x_{tt} - 2\sqrt{\beta}ux_{st} - u^2x_{ss} + f_j\sin\theta, \\
q_s = -(2 - B_j)(w_j/w_p)y_{tt} - 2\sqrt{\beta}uy_{st} - u^2y_{ss} - B_jw_j.
\end{gathered} \tag{4.3}$$

The variables are written in the form

$$\begin{aligned}
x(s,t) &= x_e(s) + x_d(s)e^{i\Omega t}, & y(s,t) &= y_e(s) + y_d(s)e^{i\Omega t}, \\
\theta(s,t) &= \theta_e(s) + \theta_d(s)e^{i\Omega t}, & m(s,t) &= m_e(s) + m_d(s)e^{i\Omega t}, \\
p(s,t) &= p_e(s) + p_d(s)e^{i\Omega t}, & q(s,t) &= q_e(s) + q_d(s)e^{i\Omega t}.
\end{aligned} \tag{4.4}$$

At equilibrium, the equations are given by

$$\begin{aligned}
x_e' &= \cos\theta_e, & y_e' &= \sin\theta_e, \\
\theta_e' &= m_e\gamma_j, & m_e' &= q_e\cos\theta_e - p_e\sin\theta_e, \\
p_e' &= -u^2x_e'' + f_j\sin\theta_e, & q_e' &= -u^2y_e'' - B_jw_j.
\end{aligned} \tag{4.5}$$

The resulting linear equations in the dynamic variables are given by

$$\begin{gathered}
x_d' = -\theta_d\sin\theta_e, \\
y_d' = \theta_d\cos\theta_e, \\
\theta_d' = m_d\gamma_j, \\
m_d' = (q_d - p_e\theta_d)\cos\theta_e - (p_d + q_e\theta_d)\sin\theta_e, \\
p_d' = \Omega^2(2 - B_j)(w_j/w_p)x_d - 2i\sqrt{\beta}u\Omega x_d' - u^2x_d'' + f_j\theta_d\cos\theta_e, \\
q_d' = \Omega^2(2 - B_j)(w_j/w_p)y_d - 2i\sqrt{\beta}u\Omega y_d' - u^2y_d''.
\end{gathered} \tag{4.6}$$

The dynamic force equations can also be written as

$$\begin{gathered}
p_d' = \Omega^2(2 - B_j)(w_j/w_p)x_d + (2i\sqrt{\beta}u\Omega\theta_d + u^2m_d)\sin\theta_e + (u^2m_e\theta_d + f_j\theta_d)\cos\theta_e, \\
q_d' = \Omega^2(2 - B_j)(w_j/w_p)y_d - (2i\sqrt{\beta}u\Omega\theta_d + u^2m_d)\cos\theta_e + u^2m_e\theta_d\sin\theta_e.
\end{gathered} \tag{4.7}$$

Table 4.1: Dimensional and nondimensional values used in the present study [68].

Baseline Values	
Dimensional	Nondimensional
$E_pI_p = 6.57$ kN-m^2, $E_bI_b = 100$ kN-m^2	$\gamma_p = 1$, $\gamma_b = 0.0657$
$H = 350$ m, $D = 350$ m	$d = 1$
$W_p = 873.09$ N/m, $W_b = 3453.12$ N/m	$w_p = 5.698$ x 10^6, $w_b = 2.253$ x 10^7
$r_p = 0.1077$ m, $r_b = 0.4275$ m, $\rho = 1025$ kg/m^3	$B_p = 0.580$, $B_b = -0.672$
$L = 560$ m, $L_1 = 122.5$ m, $L_2 = 105$ m	$l = 1.6$, $l_1 = 0.35$, $l_2 = 0.3$
$\mu_f = 18.37$ kg/m	$\beta = 0.206$
$C_d = 1$, $V = 0$ m/s	$f_j = 0$
$U = 0$ m/s	$u = 0$

4.1.2 Equilibrium Results

To obtain numerical results for the equilibrium shapes of the riser, a second-order finite difference method is used. Equations (4.5) are used to create difference equations for internal nodes of the riser. The boundary conditions at $s = 0$ ($x_e = y_e = m_e = 0$) and at $s = l$ ($x_e = d$, $y_e = 1$, $m_e = 0$) are applied at the end nodes.

Throughout the present study, baseline parameter values are as given in Table 4.1. These values were computed using the included dimensional values (similar to those used by Hong [68]).

First, the method is used to generate equilibrium results for a catenary. In this case, $w_b = w_p$, $B_b = B_p = 1$, and $d = 1$. The resulting equilbrium shape is shown in Figure 4.2. The numerical results (plotted as data points) agree well with the analytical catenary solution, $y = a\cosh((x-c)/a) - b$ (where $a = 0.424$, $b = 0.467$, and $c = 0.189$), shown by the continuous curve [78].

Parameters are then varied and resulting equilibrium shapes are found. The effect of the length of the buoyed section is illustrated in Figure 4.3. The baseline case is the second shape from the bottom. The center of the buoyed segment is located at $s = 0.5$ for this case and for the other three cases shown. The length l_2 of the buoyed segment is reduced from 0.3 to 0.2 for the lowest shape, and to 0.4 and 0.6 for the higher shapes. As l_2 is increased, all internal points of the riser move to higher positions.

In Figure 4.4, the effect of the length l_3 of the upper section is shown. The baseline length $l_3 = 0.95$ (middle shape) is raised to 1.15, and is lowered to 0.85 (i.e., the total riser length is raised from 1.6 to 1.8, and lowered to 1.5). As l_3 is increased, the upper part of the riser moves downward and the lower part moves leftward. If l_3 were increased further, the internal local minimum of the shape would reach the seafloor when $l_3 = 1.71$ and $l = 2.36$.

In Figure 4.5, the buoyancy coefficient along the buoyed segment, B_b, is varied, and resulting

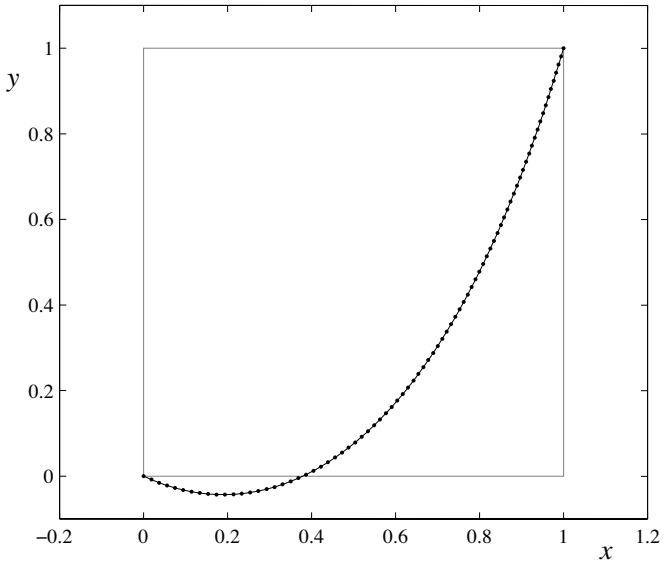

Figure 4.2: Catenary configuration with $d = 1$. Data points: numerical results using a finite difference method; continuous line - analytical solution.

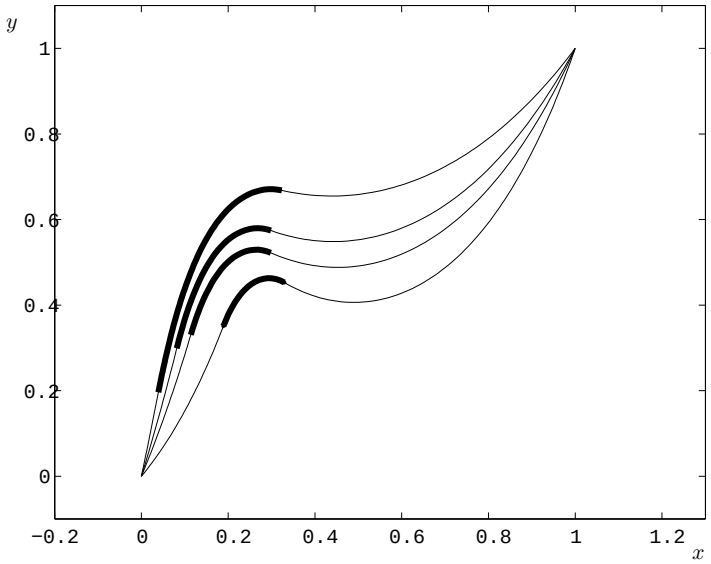

Figure 4.3: Static configurations with various buoyant segment lengths, l_2. The length l_1 is chosen such that $l_1 + 0.5l_2 = 0.5$. The lengths for each case are (beginnging with the uppermost curve): $l_1 = 0.2$, $l_2 = 0.6$; $l_1 = 0.3$, $l_2 = 0.4$; $l_1 = 0.35$, $l_2 = 0.3$; $l_1 = 0.4$, $l_2 = 0.2$;

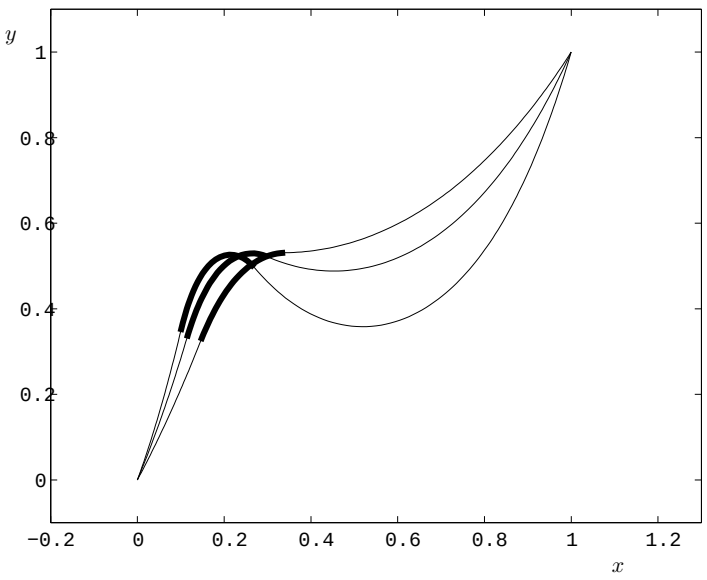

Figure 4.4: Equilibrium riser configurations where the upper-section length, l_3, is varied such that $l_3 = 1.5, 1.6, 1.8$.

equilibrium configurations are depicted. A change in the value of B_b may be caused by a change in the radius, stiffness, and/or weight of the buoyed section, each of which affects the buoyed segment weight parameter, w_b. In this case, the value of w_b is assumed to be constant. Under this assumption, $B_b < -0.215$ to avoid riser contact with the seafloor. As expected, an increase in the upward buoyancy force (i.e., in the magnitude of the buoyancy coefficient) results in a higher configuration at all internal points of the riser.

Next, the constant current velocity of the surrounding fluid is varied, and the results are shown in Figure 4.6. The current is assumed to move in the positive x-direction, and the three configurations correspond to velocities of 0, 1, and 2 m/s. As shown in Eqs. (4.3), the effect of the current force is largest where the pipe is close to vertical, and assumed to be negligible where the riser is horizontal. Because the force is also dependent upon the radius of the riser, for a given velocity, the force coefficient, f_j, is larger along the buoyed segment. Of course this effect is counteracted by the larger buoyancy effect along this segment. As the current velocity increases, the internal points on the riser naturally tend to move downstream, i.e., to the right.

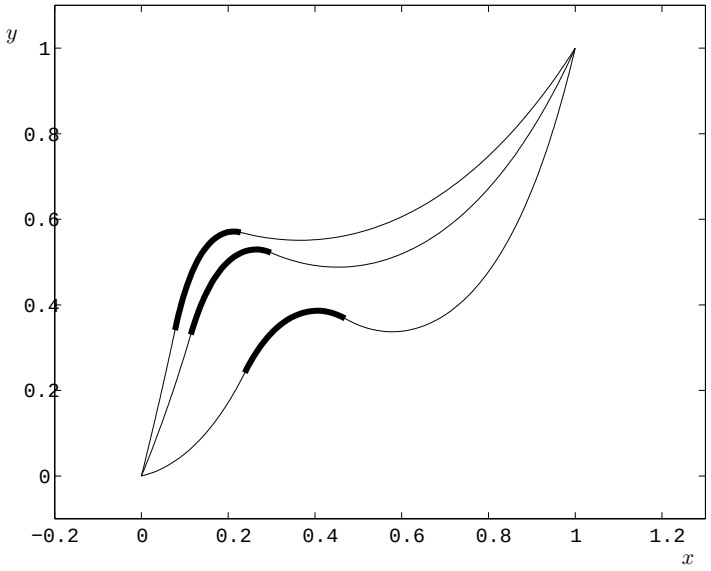

Figure 4.5: Static configurations for varying buoyancy coefficient values, $B_b = -1.25$ (uppermost configuration), -0.672, -0.25.

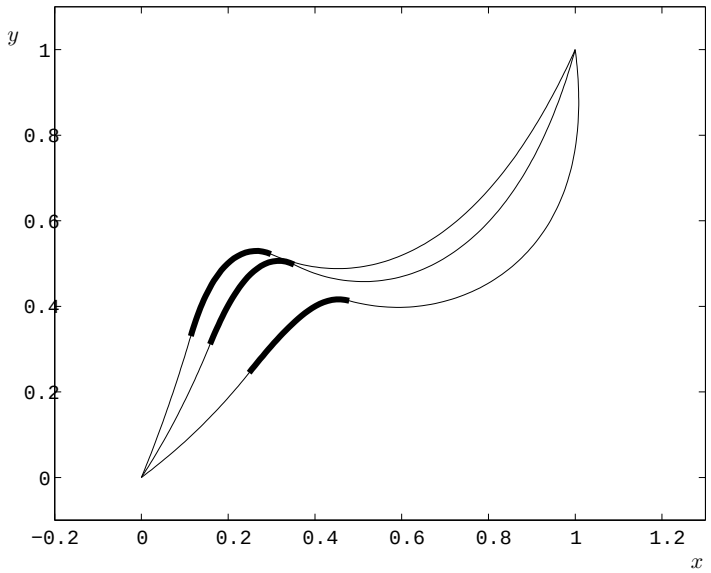

Figure 4.6: The effect of a steady current with velocity, V, on the static configuration. f_p values ($f_p = 0$ (uppermost configuration), 7.204×10^5, 2.882×10^6) correspond to dimensional velocities of $V = 0$, 1, and 2 m/s (giving $f_b = 0$, 2.860×10^6, 1.144×10^7).

4.1.3 Vibration Results

Small vibrations about equilibrium are considered. A finite difference method is again applied to obtain numerical solutions to Eqs. (4.6) and (4.7), using Eqs. (4.5) . The boundary conditions at $s = 0$ and $s = l$ are $x_d = y_d = m_d = 0$.

The first in-plane vibration frequency of the catenary is found (again where $B_b = B_p = 1$ and $w_b = w_p$) for varying d values, and are in agreement with [74]. For the baseline value, $d = 1$, the corresponding natural frequency is $\Omega = 3{,}986$ (or 0.0444 Hz).

The frequency for the first in-plane vibration mode of the riser (using the baseline parameter values) is $\Omega = 1{,}733$ (or 0.0193 Hz) and the corresponding mode shape is shown in Figure 4.7. The primary motion is horizontal.

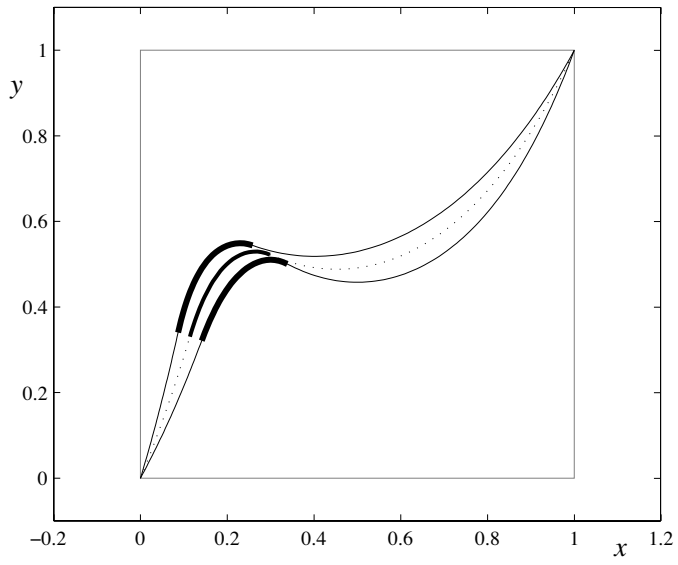

Figure 4.7: Mode shape corresponding to the first frequency of the riser (with baseline parameter values). The equilibrium configuration is given by the dotted line.

Figure 4.8 gives the fundamental frequency as a function of B_b, assuming again that this buoyancy coefficient can by varied independently from the weight parameter, w_b, and results are plotted only over the range of B_b values that prevent seafloor contact. The frequency is seen to increase by approximately 50 percent as the upward buoyancy force is increased (and B_b is decreased) over the range of B_b values shown.

The first (fundamental) frequency as a function of buoyed segment length, l_2, is plotted in

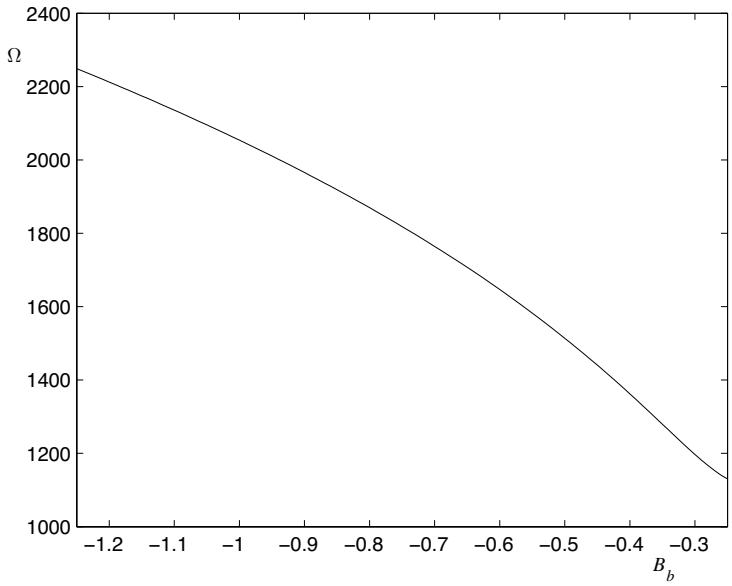

Figure 4.8: Frequency, Ω, as a function of the buoyancy coefficient, B_b.

Figure 4.9 where, again, the length $l_1+0.5l_2$ and the total length l are fixed. The frequency decreases with length for small l_2 values, then increases as the buoyant segment length is increased. Because the lengths l_1 and l_2 must be a multiple of the node spacing (in the finite difference algorithm), the number of data points in the plot is limited. The continuous line is a polynomial curve-fit of the numerical data points.

The current velocity is then varied and the corresponding fundamental frequency is computed. In Figure 4.10, dimensional values of V versus frequency in Hz are plotted as the solid curve, and nondimensional values Ω are plotted versus f_p as the dashed curve. The frequency reaches a minimum when $V = 0.87$ m/s.

4.1.4 Concluding Remarks

Planar equilibrium shapes of the steep-wave riser and small vibrations about equilibrium have been analyzed. The riser is modeled as an inextensible elastica, in which the bending stiffness is included and the bending moment is assumed to be proportional to the curvature. The ends are pinned at fixed locations, and an internal section is buoyed so that the net force in that section acts upward. A baseline case is defined, and numerical results are obtained using the finite difference method. Internal fluid flow in the riser is included in the governing equations, but not in the

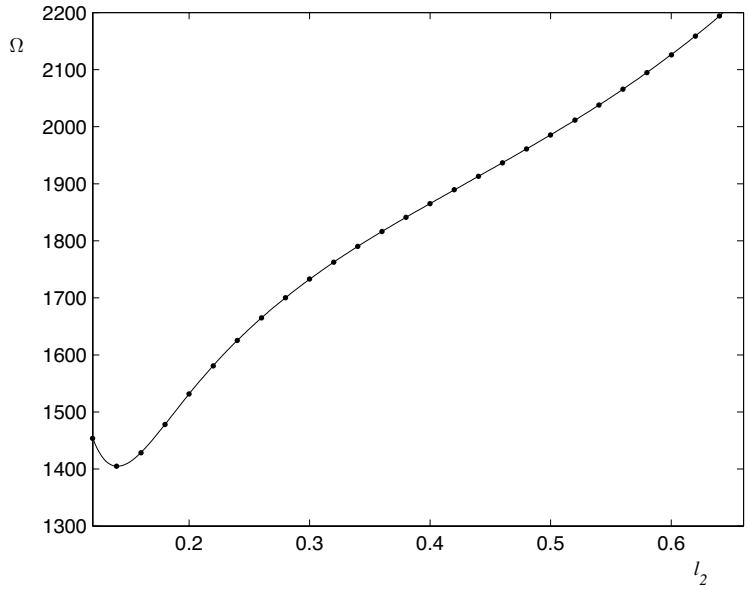

Figure 4.9: Frequency as a function of buoyed segment length.

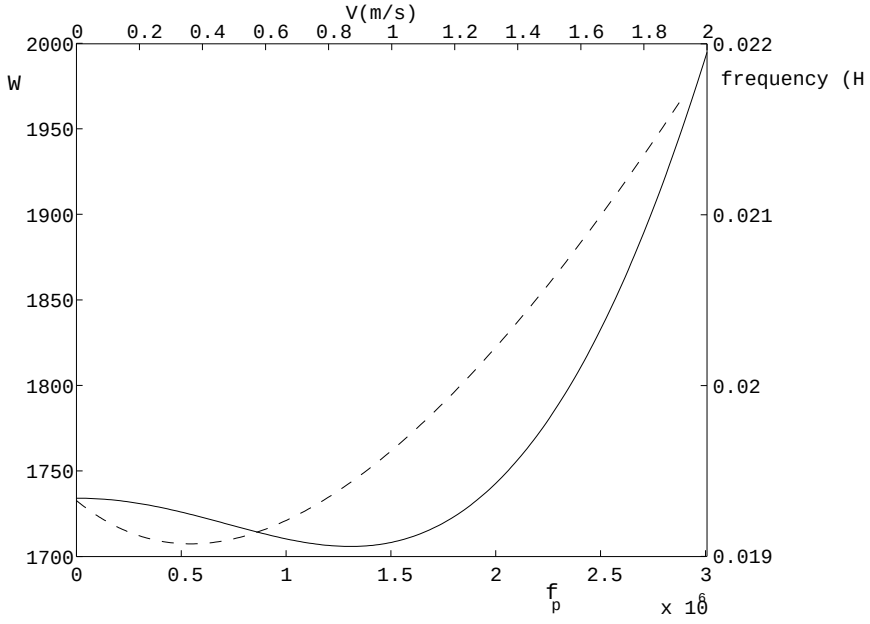

Figure 4.10: Frequency as a function of steady current velocity, dashed curve: Ω vs f_p; solid curve: V vs dimensional frequency.

presented results (since its effect is small for practical conditions). The effects of the following parameters on the equilibrium shape have been investigated: length of the buoyed section, length of the upper unbuoyed section, magnitude of the buoyancy force, and velocity of the steady horizontal current. The fundamental mode of vibration consists primarily of back and forth horizontal motion of the riser. The fundamental frequency tends to increase with an increase of the buoyancy force and with an increase in the length of the buoyed segment. As the current velocity is increased from zero, the fundamental frequency initially decreases and then increases.

Chapter 5

Concluding Remarks

In this study, the elastica equations were used to investigate a number of boundary condition cases of the two-dimensional study of beam dynamics, with applications to vibration isolation and nonlinear beam vibrations.

First, linear theory was introduced, along with its limitations in static and dynamic beam analyses. The elastica equations were then given, and were shown to be useful and accurate in determining large-deflection behavior where self-weight may be included. It was assumed in the equation derivation, however, that the beam is inextensible and that shear deformation is negligible (for a slender beam, it is reasonable to neglect these effects). The solutions for static deflection of the cantilever under self-weight were compared with some in the literature. Next, linear beam vibrations were introduced, along with traditional solution methods for small-amplitude beam vibrations. Some numerical techniques that are useful for the solution of boundary value problems were introduced. For nonlinear equilibrium and linear vibration solutions, the shooting method is useful and efficient, and the finite difference method may be used to characterize large-amplitude vibrations about both trivial and nontrivial equilibria. Two analytical methods - the Galerkin method and a perturbation method - were also introduced. While the Galerkin method (when applied to the elastica equations) is not useful for large dynamic deflections (if the condition of inextensibility is to be satisfied), the perturbation method gives accurate vibration solutions for a moderate range of dynamic deflection amplitudes. Experimental methods were then described, and some numerical and experimental studies of the equilibria and linear vibrations of the cantilever, heavy clamped-clamped beam, and pinched loop were shown.

Next, the elastica equations, as applied to vibration isolation, were studied. Three different systems were modeled and analyzed. The vertical and horizontal buckled beam isolator systems were introduced and shown to be effective isolators. For the vertical isolator, the transmissibility peaks occur near the natural frequencies of the system, where each of the n struts were assumed to behave identically. The horizontal system, however, was analyzed by considering the motion of each strut, because the two may not deflect in phase (at resonance, for example) or with equal amplitudes. This system exhibits some mode localization at transmissibility peaks beyond the first, producing

effective vibration isolation of the central mass. Finally, the pinched loop isolator was introduced. Only half of the beam length was analyzed, as the mass motion and excitation were assumed to be exclusively in the vertical direction. The static loop deflection due to a point load by the mass was found and agreed closely with experimental data. Next, natural frequencies and corresponding mode shapes of the system were found as a function of the mass load (where there is no minimum mass load required, as for the vertical, buckled beam isolator). Experimental transmissibility results were obtained for varying mass loads and lengths, and were found to agree well with the numerical transmissibility. Some additional transmissibility peaks were seen in the experimental data, and these may correspond to out-of-plane motion or some in-plane motion resulting from asymmetry in the experimental system.

Nonlinear beam vibrations were then investigated, where motion about trivial equilibria were studied first. The perturbation method was used to derive analytical backbone curves for the beam with various boundary conditions, where, in each case, self-weight was neglected. The results compare well with those from a similar study in the literature (where the equations were derived using an energy approach). The Perturbation Method was then applied to the elastica equations to determine analytical backbone curves for the heavy, upright, prebuckled cantilever, and the system was found to be increasingly hardening with weight in the first mode. The finite difference method was also used to find numerical backbone curve results, where steady-state vibration and lightly damped free vibration results were seen to agree closely. This method was also used to characterize the large-amplitude motion of beams about nontrivial equilibria (with and without self-weight). Finally, some extensions of the research were presented and some preliminary studies of subsea risers using this type of elastica analysis were described. The equations were derived such that the effects of gravity, buoyancy, buoyant segment length, and velocities (of the surrounding fluid current and conveying fluid) could be considered.

The elastica equations certainly may be used to generate accurate results well beyond those from the linear theory, where relevant forces (for a given application) may be included in the analysis. Numerical and analytical methods are useful in obtaining solutions to these equations, and there are many applications and extensions of the research herein.

Bibliography

[1] S.P. Timoshenko and J.M. Gere. *Theory of Elastic Stability*. McGraw-Hill, Tokyo, second edition, 1961.

[2] F.P. Beer and E.R. Johnston Jr. *Statics and Mechanics of Materials*. McGraw-Hill, New York, second edition, 1992.

[3] A.G. Greenhill. Determination of the greatest height consistent with stability that a vertical pole or mast can be made, and of the greatest height to which a tree of given proportions can grow. In *Proceedings of the Cambridge Philosophical Society*, volume 4, pages 65 – 73, 1881.

[4] R. Frisch-Fay. The analysis of a vertical and a horizontal cantilever under a uniformly distributed load. *Journal of the Franklin Institute*, 271(3):192 – 199, 1961.

[5] L.N. Virgin. Free vibrations of imperfect cantilever bars under self-weight loading. *Journal of Mechanical Engineering Science*, 201:345 – 347, 1987.

[6] G.B. Sinclair. The nonlinear bending of a cantilever beam with shear and longitudinal deformations. *International Journal of Non-linear Mechanics*, 14:111 – 122, 1979.

[7] H. Lurie. Lateral vibrations as related to structural stability. *Journal of Applied Mechanics*, 19:195 – 204, 1952.

[8] R.H. Plaut and L.N. Virgin. Use of frequency data to predict buckling. *Journal of Engineering Mechanics*, 116:2330 – 2335, 1990.

[9] L. Meirovitch. *Fundamentals of Vibrations*. McGraw-Hill, Boston, 2001.

[10] B.H. Tongue. *Principles of Vibration*. Oxford University Press, New York, 1996.

[11] D.J. Inman. *Engineering Vibration*. Prentice-Hall, Upper Saddle River, 2001.

[12] R.D. Blevins. *Formulas for Natural Frequency and Mode Shape*. Krieger, Malabar, 1979.

[13] S.H. Strogatz. *Nonlinear Dynamics and Chaos*. Perseus, Reading, 1994.

[14] S.T. Santillan, L.N. Virgin, and R.H. Plaut. Post-buckling and vibration of heavy beam on horizontal or inclined rigid foundation. *Journal of Applied Mechanics*, 73:664 – 671, 2006.

[15] C.Y. Wang. On symmetric buckling of a finite flat-lying heavy sheet. *Journal of Applied Mechanics*, 51(2):278 – 282, 1984.

[16] R. Frisch-Fay. *Flexible Bars*. Butterworth, London, 1962.

[17] J. Stolte and R.C. Benson. Dynamic deflection of paper emerging from a channel. *Journal of Vibration and Acoustics*, 114:187 – 193, 1992.

[18] M. Hermann and D. Kaiser. Numerical methods for parametrized two-point boundary value problems - a survey. *Reports of the Interdisciplinary Center for Scientific Computing*, 1:23 – 38, 2003.

[19] R.L. Burden and J.D. Faires. *Numerical Analysis*. Prindle, Weber and Schmidt, Belmont, third edition, 1985.

[20] A. Quarteroni, R. Sacco, and F. Saleri. *Numerical Mathematics*. Springer, New York, 2000.

[21] W.H. Press. *Numerical Recipes in C*. Cambridge, cambridge, second edition, 2002.

[22] E.L. Allgower and K. Georg. *Introduction to Numerical Continuation Methods*. SIAM, Philadelphia, 2003.

[23] J.C. Slater. A numerical method for determining nonlinear normal modes. *Nonlinear Dynamics*, 10:19 – 30, 1996.

[24] W.J. Duncan. *Galerkin's Method in Mechanics and Differential Equations*. HMSO, London, 1928.

[25] M.H. Holmes. *Introduction to Perturbation Methods*. Springer, New York, 1995.

[26] H.R. Öz, M. Pakdemirli, E. Özkaya, and M. Yilmaz. Nonlinear vibrations of a slightly curved beam resting on a non-linear elastic foundation. *Journal of Sound and Vibration*, 212(2):295 – 309, 1998.

[27] L.N. Virgin, S.T. Santillan, and D.B. Holland. Effect of gravity on the vibration of vertical cantilevers. *Mechanics Research Communications*, 34:312 – 317, 2007.

[28] G. Domokos, W.B. Fraswer, and I Szeberényi. Summetry-breaking bifurcations of the uplifted elastic strip. *Physica D*, 185(1):67 – 77, 2003.

[29] S. Santillan, L.N. Virgin, and R.H. Plaut. Equilibria and vibration of a heavy pinched loop. *Journal of Sound and Vibration*, 288:81 – 90, 2005.

[30] J. Ellison, G. Ahmadi, and M. Kehoe. Passive vibration control of airborne equipment using a circular steel ring. *Journal of Sound and Vibration*, 246(1):1 – 28, 2001.

[31] R.H. Plaut, J.E. Sidbury, and L.N. Virgin. Analysis of buckled and pre-bent fixed-end columns used as vibration isolators. *Journal of Sound and Vibration*, 283:1216 – 1228, 2005.

[32] C.E. Crede. *Vibration and Shock Isolation*. Wiley, New York, 1951.

[33] R.H. Plaut, L.A. Alloway, and L.N. Virgin. Nonlinear oscillations of a buckled mechanism used as a vibration isolator. In *Proceedings of the IUTAM Symposium on Chaotic Dynamics and Control of Systems and Processes in Mechanics*, volume III, pages 241 – 250, 2005.

[34] L.N. Virgin and R.B. Davis. Vibration isolation using buckled struts. *Journal of Sound and Vibration*, 260:965 – 973, 2003.

[35] P. Bonello, M.J. Brennan, and S.J. Elliott. Vibration control using an adaptive tuned vibration absorber with a variable curvature stiffness element. *Smart Materials and Structures*, 14:1055 – 1065, 2005.

[36] J. Winterflood, T. Barber, and D.G. Blair. Using Euler buckling springs for vibration isolation. *Classical and Quantum Gravity*, 19:1639 – 1645, 2002.

[37] J. Winterflood, T.A. Barber, and D.G. Blair. Mathematical analysis of an Euler spring vibration isolator. *Physics Letters A*, 300:131 – 139, 2002.

[38] J. Winterflood, D.G. Blair, and B. Slagmolen. High performance vibration isolation using springs in Euler column buckling mode. *Physics Letters A*, 300:122 – 130, 2002.

[39] R.H. Plaut, H.M. Favor, A.E. Jeffers, and L.N. Virgin. Vibration isolation using buckled or pre-bent columns. part 1: two-dimensional motions of horizontal rigid bar. *Journal of Sound and Vibration*, submitted for publication.

[40] A.E. Jeffers, R.H. Plaut, and L.N. Virgin. Vibration isolation using buckled or pre-bent columns. part 2: three-dimensional motions of horizontal rigid bar. *Journal of Sound and Vibration*, submitted for publication.

[41] D.J. Ewins. *Modal Testing: Theory and Practice*. Wiley, London, 1984.

[42] T.A. Nayfeh, E. Emaci, and A.F. Vekakis. Application of nonlinear localization to the optimization of a vibration isolation system. *AIAA Journal*, 35(8):1378 – 1386, 1997.

[43] A.F. Vakakis, L.I. Manevitch, Y.V. Mikhlin, V.N. Pilipchuk, and A.A. Zevin. *Normal Modes and Localization in Nonlinear Systems*. Wiley, New York, 1996.

[44] S.R. Marur. Advances in nonlinear vibration analysis of structures. *Sādhanā*, 26:243 – 249, 2001.

[45] M.K. Verma and A.V. Krishna Murthy. Nonlinear vibrations of non-uniform beams with concentrated masses. *Journal of Sound and Vibration*, 33(1):1 – 12, 1974.

[46] A. Luongo, G. Rega, and F. Vestroni. On nonlinear dynamics of planar shear indeformable beams. *Journal of Applied Mechanics*, 53:619 – 624, 1986.

[47] M. Pakdemirli and H. Boyaci. Comparison of direct-perturbation methods with discretization-perturbation methods for nonlinear vibrations. *Journal of Sound and Vibration*, 186(5):837 – 845, 1995.

[48] J.G. Eisley. Large amplitude vibration of buckled beams and rectangular plates. *AIAA Journal*, 2(12):2207 – 2209, 1964.

[49] E. Özkaya, M. Pakdemirli, and H.R. Öz. Nonlinear vibrations of a beam-mass sytem under different boundary conditions. *Journal of Sound and Vibration*, 199(4):679 – 691, 1997.

[50] N.Yamaki and A. Mori. Nonlinear vibrations of a clamped beam with initial deflection and initial axial displacement, part I: theory. *Journal of Sound and Vibration*, 71(3):333 – 346, 1980.

[51] W. Lestari and S. Hanagud. Nonlinear vibration of buckled beams: some exact solutions. *International Journal of Solids and Structures*, 38:4741 – 4747, 2001.

[52] G. Prathap and T.K. Varadan. Nonlinear vibrations of tapered cantilevers. *Journal of Sound and Vibration*, 55(1):1 – 8, 1977.

[53] W. Lacarbonara and A.H. Nayfeh. Experimental validation of reduction methods for nonlinear vibrations of distributed-parameter systems: analysis of a buckled beam. *Nonlinear Dynamics*, 17:95 – 117, 1998.

[54] R.W. Krauss and A.H. Nayfeh. Experimental nonlinear identification of a single mode of a transversely excited beam. *Nonlinear Dynamics*, 18:69 – 87, 1999.

[55] Z. Rahman and T.D. Burton. On higher order methods of multiple scales in nonlinear oscillations - periodic steady state response. *Journal of Sound and Vibration*, 133(3):369 – 379, 1989.

[56] M.N. Hamdan, A.A. Al-Quaisia, and B.O. Al-Bedoor. Comparison of analytical techniques for nonlinear vibrations of a parametrically excited cantilever. *International Journal of Mechanical Sciences*, 43:1521 – 1542, 2001.

[57] W.Y. Poon, C.F. Ng, and Y.Y. Lee. Dynamic stability of a curved beam under sinusoidal loading. *Proceedings of the Institution of Mechanical Engineers, Part G: Journal of Aerospace Engineering*, 216:209 – 217, 2002.

[58] S.A. Emam and A.H. Nayfeh. On the nonlinear dynamics of a buckled beam subjected to a primary-resonance excitation. *Nonlinear Dynamics*, 35(2):1 – 17, 2004.

[59] J.C. Ji and C.H. Hansen. Nonlinear response of a post-buckled beam subjected to a harmonic axial excitation. *Journal of Sound and Vibration*, 237(2):303 – 318, 2000.

[60] J.P. Cusumano and F.C. Moon. Chaotic non-planar vibrations of the thin elastica, part II: derivation and analysis of a low-dimensional model. *Journal of Sound and Vibration*, 179(2):209 – 226, 1995.

[61] N.Yamaki, K. Otomo, and A. Mori. Nonlinear vibrations of a clamped beam with initial deflection and initial axial displacement, part II: experiment. *Journal of Sound and Vibration*, 71(3):347 – 360, 1980.

[62] H.E. Hinnant and D.H. Hodges. Nonlinear analysis of a cantilever beam. *AIAA Journal*, 26(12):1521 – 1527, 1988.

[63] K. Nandakumar and A. Chatterjee. Resonance, parameter estimation, and modal interactions in a strongly nonlinear benchtop oscillator. *Nonlinear Dynamics*, 40:149 – 167, 2005.

[64] G.R. Scholz and C.D. Rahn. Profile sensing with an actuated whisker. *IEEE Transactions on Robotics and Automation*, 20(1):124 –127, 2004.

[65] K.F. Voss and K.H. Wanser. Fiber-optic strain-displacement sensor employing nonlinear buckling. *Applied Optics*, 36(13):2944 –2946, 1997.

[66] S. Goyal, N.C. Perkins, and C.L Lee. Nonlinear dynamics and loop formation in kirchhoff rods with implications to the mechanics of dna and cables. *Journal of Computational Physics*, 209:371 – 389, 2005.

[67] Y. Bai and Q. Bai. *Subsea Pipelines and Risers*. Elsevier, Amsterdam, 2005.

[68] S. Hong. Three-dimensional static analysis of flexible risers by a lumped-mass method. In *Proceedings of the Fourth International Offshore and Polar Engineering Conference*, volume II, pages 251 – 257, 1994.

[69] T. Huang and S. Chucheepsakul. Large displacement analysis of a marine riser. *Journal of Energy Resources Technology*, 107:54 – 59, 1985.

[70] F.B. Seyed and M.H. Patel. Parametric studies of flexible risers. In *Proceedings of the First International Offshore and Polar Engineering Conference*, volume II, pages 147 – 156, 1991.

[71] Y. Liu and L. Bergdahl. Frequency-domain dynamic analysis of cables. *Engineering Structures*, 19:499 – 506, 1997.

[72] K. Ahmadi-Kashani. Vibration of hanging cables. *Computers and Structures*, 31:699 – 715, 1989.

[73] C.E. Smith and R.S. Thompson. The small oscillations of a suspended flexible line. *Journal of Applied Mechanics*, 40:624 – 626, 1973.

[74] R. Bylsma, A. Nguyen, and D.A. Van Baak. Oscillations of a suspended chain. *American Journal of Physics*, 56:1024 – 1032, 1988.

[75] K. Vikestad, J.K. Vandiver, and C.M. Larsen. Added mass and oscillation frequency for a circular cylinder subjected to vortex-induced vibrations and external disturbance. *Journal of Fluids and Structures*, 14:1071 – 1088, 2000.

[76] R.D. Gabbai and H. Benaroya. An overview of modeling and experiments of vortex-induced vibration of circular cylinders. *Journal of Sound and Vibration*, 282:575 – 616, 2005.

[77] Y.T. Chai and K.S. Varyani. An absolute coordinate formulation for three dimensional flexible pipe analysis. *Ocean Engineering*, 33:23 – 58, 2006.

[78] P. Cella. Methodology for exact solution of catenary. *Journal of Structural Engineering*, 125:1451 – 1453, 1999.

Biography

Sophia Teresa Santillan was born on August 12, 1979 in Amarillo, Texas. She graduated from Amarillo High School in 1997 and received her Bachelor of Science in Engineering degree in Mechanical Engineering from Duke University, along with a Bachelor of Science degree in Mathematics, in May 2001. She earned her Master of Science degree in Mechanical Engineering from Duke University in May 2005. She has coauthored three journal papers: "Effect of Gravity on the Vibration of Vertical Cantilevers" (Mechanics Research Communications), "Post-buckling and Vibration of Heavy Beam on Horizontal or Inclined Rigid Foundation" (Journal of Applied Mechanics), and "Equilibria and Vibration of a Heavy Pinched Loop" (Journal of Sound and Vibration). She has also coauthored two conference proceedings papers: "Vibration Isolation Using Extreme Geometric Nonlinearity" (EUROMECH Colloquium 483: Geometrically Nonlinear Vibrations of Structures) and "Dynamic Behavior of Highly-Deformed Risers and Pipelines" (Twenty-Sixth International Conference on Offshore Mechanics and Arctic Engineering).

She was a recipient of the North Carolina Space Grant Consortium Graduate Fellowship and is a member of Pi Tau Sigma, the American Society of Mechanical Engineers, and the Society of Hispanic Professional Engineers.